Bandgap Engineering and Molecular Selectivity of 2D Nanostructures by First-Principles Simulations

Xiaoyu Han

A dissertation submitted in partial fulfillment
of the requirements of the degree of
Doctor of Philosophy
of
University College London

Department of Chemistry
University College London
September 2015

Declaration

I, Xiaoyu Han confirm that the work presented in this thesis is my own. Where information has been derived from other sources, I confirm that this has been indicated in the thesis

Acknowledgements

First of all, I'd like to thank Prof. Zheng Xiao Guo for letting me work on this project and his support throughout my research time in London and in Zhengzhou. Without him, I couldn't start my Ph.D. from the beginning. Furthermore, thanks are also due to Prof. Julian Evans who is a true academic idol to me. His suggestions and generous help truly have inspired me.

I'd also like to thank all the members of Xiao's group, past and present. Dr. Stephen Shevlin has helped me throughout my Ph.D. I am appreciated his willingness and patient. I am grateful for Dr. William Travis, Dr. Srinivas Gadipelli for the kindness advice. Additionally, I would like also to thank my collaborators who are the true young talents. I am grateful for the inspirational discussion we had and the friendship shared with me. In regards to the graphene/ diamond heterostructure work, I thank the experimental data supports from Dr. Fang Zhao in EEE Department and Dr. Ling Hao's group from National Physical Laboratory. Deeply thankful to Henry Morgan Stewart who shared the workloads with me on the phosphorene nanoribbons. I am also appreciated Haitang Luo for her MD simulation work on the gas selectivity enhancement with porous graphene.

Special thanks to Prof. Angelos Michaelides and Prof. Feliciano Giustino for reviewing my thesis and exam my Ph.D. viva. Their insightful questions challenged and broadened my knowledge in the area, some of which I would never think of. The suggestions and comments improved my thesis from single word error to better coherent constructed.

To those close friends met in London, Xiaoxue Zhao and Yiqi Deng, they felt like my families to me. I am so grateful for their countless help, constantly support and invaluable friendship.

Xiaoyu Han

UCL

September 2015

To mum

"We are what we pretend to be,

so we must be careful about what we pretend to be"

Kurt Vonnegut, *Mother Night*

Abstract

Two-Dimensional (2D) materials often exhibit far more distinguished properties than their 3D counterparts and offer great potential to advance technologies. However, even graphene, the star of 2D materials, still face several challenges, despite its high mobility and high thermal conductivity. One of such challenges is the lack of a bandgap for use in electronics, photonics or photocatalysis. Here, we propose two approaches to tuning the bandgap: One is by vacancy and nitrogen substitution, and another by substrate interaction. Several vacancy/nitrogen configurations were considered in the study. One of the defective complexes, with 2 vacancies and 4 N atoms, can open up the bandgap to 0.27 eV. Diamond substrate of different orientations with or without hydrogen termination was employed to create a heterostructure with graphene. Our calculations indicate that the hydrogen treatment of the diamond surface plays an important role, and so is the surface orientation, in determining the size of the bandgap. A hydrogen-terminated diamond with (100) surface can tune the bandgap of graphene to 61 meV. This agrees well with collaborative experimental measurement of a similar system.

Another newly discovered 2D material, phosphorene, was also investigated with a particular focus on the effects of nanostructuring, straining, and hybridization with graphene. Phosphorene nanoribbons (PNR) with different widths and orientations were considered. Significant quantum confinement causes the bandgap to vary substantially with ribbon width and orientation. Furthermore, the straining effect is also shown to alter the electronic properties dramatically. For a diagonally-cut nanoribbon (d-PNR), the direct to indirect bandgap switch-over occurred below -7% compression or beyond +3% extension. As phosphorene may degrade in the air, a graphene/phosphorene/graphene (G/P/G) sandwich heterostructure is designed and studied. The bandgap of this sandwich heterostructure is 19 meV, due to charge redistribution within the interlayers. The calculated dielectric constant show large

directional variation, due to phosphorene's puckered structure. This suggests G/P/G may be considered for birefringence optical applications.

The defective graphene is also a strong contender for gas separation and H_2 purification, which is also studied here. The results show that graphene with a vacancy cluster (pore-10) show exceptional selectivity for H_2 at room temperature, while inhibiting many other gaseous molecules. Nitrogen-doping can attract more gas molecules to the pore area, increasing the propensity of "trapping" molecular impurities. In particular, a strong energy trap is generated when a CO_2 molecule approaches the proposed nanopore, due to its relative strong quadruple moment interacting with N-doped carbon edge sites. A CH_4 molecule needs to overcome a sequence of energy barriers in order to pass through the pore. Such interactions inhibit the impurity molecules and enhance the selectivity for H_2 purification.

Table of Contents

Chapter I
Introduction

The successful exfoliation and then characterizations of graphene in 2004, by Novoselov and Geim *et al.*, have generated a huge wave of interest in two-dimensional (2D) materials for solid-state science and technologies.[1] Graphene, a monolayer of sp^2 carbon, exhibits distinctive properties that no other material can reach, such as extremely high electron mobility (15,000 $cm^2V^{-2}s^{-1}$),[2] exceptionally large thermal conductivity (5,300 $Wm^{-1}K^{-1}$),[3] high optical conductance,[4] high stiffness (1 TPa)[5] and anomalous quantum Hall effect.[6] This effort is followed by further explorations of other 2D materials, such as transition metal dichalcogenides (TMDCs),[7] puckered silicene,[8] germanene[9] and phosphorene.[10]

However, massive production of graphene for practical applications encounters two major obstacles: one is the synthesis of high-quality graphene in industrial scale, and the other is to engineer structures with a suitable bandgap for electronic and photonic devices. For the former, many approaches have been investigated, one of which is to use patterned epitaxial growth on a single crystal silicon carbide substrate.[11] A relatively low-cost approach is liquid-phase exfoliation of graphite.[12,13] The most common method of generating a large area of graphenes with no or low defect densities is to use chemical vapour deposition (CVD) on a metal substrate, mostly copper.[14,15] Up to date, graphene films up to 30-inch have been produced onto flexible copper substrates by CVD.[16]

For the second issue, the absence of a bandgap makes graphene difficult to integrate into high-performance logic circuits.[17] In order to "engineer" the bandgap, many attempts are devoted to nanostructuring of graphene into nanoribbons,[18,19] and bilayers,[20,21] chemical modifications,[22,23] and tuning by a substrate.[24] So far, no desirable achievement has been reached for graphene. Moreover, once graphene is supported on a substrate, substrate-induced

structural distortion,[25] local charge disorder,[26] edge effects,[27] defects and impurities[28] would strongly affect its properties.

Surpassing the bandgap issue of graphene, other 2D materials with a natural bandgap also attract considerable attention. Taking TMDCs (Transitional Metal Di-Chalcogenides) as an example, monolayer TMDCs show a direct bandgap, but turn into an indirect one with the multilayer counterparts.[29] Others, such as silicene and germanene, also elements in Group 14, have a direct bandgap,[8,9] but are unstable in air.[30] Newly exfoliated few-layer phosphorenes follow the same path of synthesis as graphene.[10,31] Unlike graphite or TMDCs, layered bulk black phosphorous possesses a direct bandgap around 0.3 eV.[32] This 2D material opens a new scope for exploration of 2D functional nanostructures.

Hence, the objectives of the project are:
1) to investigate different approaches to tuning the graphene bandgap;
2) to explore other 2D materials, complementary to graphene;
3) to understand the fundamental mechanisms of the effects of defects, doping, substrate hybridization and nanostructuring.

The thesis is organized as follows. Chapter 2 illustrates the background of the theory of carbon, diamond, and graphene and experimental efforts on bandgap opening of graphene. The theoretical methodology is presented in Chapter 3. In Chapter 4, a systematical study of nitrogen doped mono-/bi vacancy graphenes is reported, with particular attention paid to nitrogen doping on bandgap opening of graphene. Another approach to bandgap tuning by diamond substrates was investigated theoretically and compared with the experimental results from collaborative partners in Chapter 5. In Chapters 6 and 7, newly developed 2D materials, phosphorenes, were

investigated by nanostructuring, strain engineering and combined with graphene as a heterostructure, respectively. Chapter 8 contributes to H_2 purification by means of defective graphene, as part of the project effort. This is followed by General Discussion and Conclusions in Chapter 9 and Future Work in Chapter 10, respectively.

References

[1] K. S. Novoselov, A, K. Geim, S. V. Morozov, D. Jiang, Y. Zhang, S. V. Dubonos, I. V. Grigorieva, A. A. Firsov, *Science*, **2004**, 306, 666;

[2] A. K. Geim, K. S. Novoselov, *Nature Materials*, **2007**, 6(3), 183;

[3] A. A. Balandin, S. Ghosh, W. Bao, I. Calizo, D. Teweldebrhan, F. Miao, and C. N. Lau, *Nano Lett.* **2008**, 8(3), 902;

[4] A. B. Kuzmenko, E. van Heumen, F. Carbone, and D. van der Marel, *Phys. Rev. Lett.* **2008**, 100, 117401;

[5] C. Lee, X. Wei, J. W. Kysar, J. Hone, *Science* **2008**, 321, 385;

[6] K. S. Novoselov, A. K. Geim, S. V. Morozov, D. Jiang, M. I. Katsnelson, I. V. Grigorieva, S. V. Dubonos, and A. A. Firsov, *Nature,* **2005**, 438, 197;

[7] B. Radisavljevic, A. Radenovic, J. Brivio, V. Giacometti and A. Kis, *Nature Nanotech.* **2011**, 6, 147;

[8] B. Aufray, A. Kara, S. Vizzini, H. Oughaddou, C. Léandri, B. Ealet and G. Le Lay, *Appl. Phys. Lett.* **2010**, 96, 183102;

[9] M. E. Dávila, L. Xian, S. Cahangirov, A. Rubio, and G. Le Lay, *New J. Phys.* **2014**, 16, 095002;

[10] L. Li, Y. Yu, G. J. Ye, Q. Ge, X. Ou, H, Wu, D. Feng, X. H. Chen, and Y. Zhang, *Nature Nanotech.* **2014**, 9(5), 372;

[11] C. Berger, Z. Song, X. Li, X. Wu, N. Brown, C. Naud, D. Mayou, T. Li, J. Hass, A. N. Marchenkov, E. H. Corad, P. N. First, and W. A. de Heer, *Science* **2006**, 312, 1191;

[12] P. Blake, P. D. Brimicombe, R. R. Nair, T. J. Booth, D. Jiang, F. Schedin, L. A. Ponomarenko, S. V. Morozov, H. F. Gleeson, E. W. Hill, A. K. Geim and K. S. Novoselov, *Nano Lett.* **2008**, 8(6), 1704;

[13] Y. Hernandez, V. Nicolosi, M. Lotya, F. M. Blighe, Z. Sun, S. De, I. T. McGovern, B. Holland, M. Byrne, Y. K. Gun'Ko, J. J. Boland, P. Niraj, G. Duesberg, S. Krishnamurthy, R. Goodhue, J. Hutchison, V. Scardaci, A. C. Ferrari and J. N. Coleman, *Nature Nanotech.* **2008**, 3, 563;

[14] X. Li, W. Cai, J. An, S. Kim, J. Nah, D. Yang, R. Piner, A. Vallemakanni, I. Jung, E. Tutuc, S. K. Banerjee, L. Colombo and R. S. Ruoff. *Science*, **2009**, 324, 1312;

[15] M. Losurdo, M. M. Giangregorio, P. Capezzuto and G. Bruno, *Phys. Chem. Chem. Phys.* **2011**, 13, 20836;

[16] S. Bae, H. Kim, Y. Lee, X. Xu, J. –S. Park, Y. Zheng, J. Balakrishnam, T. Lei, H. R. Kim, Y. I. Song, Y. –J. Kim, K. S. Kim, B. Özyilmaz, J. –H. Ahn, B. H. Hong, and S. Lijima, *Nature Nanotech.* **2010**, 5, 574;

[17] K. S. Novoselov, V. I. Fal'ko, L. Colombo, P. R. Gellert, M. G. Schwab and K. Kim, *Nature,* **2012**, 490,192;

[18] J. Cai, P. Ruffieux, R. Jaafar, M. Bieri, T. Braun, S. Blankenburg, M. Muoth, A. P. Seitsonen, M. Saleh, X. Feng, K. Müllen, and R. Fasel, *Nature*, **2010**, 466, 470;

[19] M. Y. Han, B. Özyilmaz, Y. Zhang, and P. Kim, *Phys. Rev. Lett.* **2007**, 98, 206805;

[20] T. Ohta, A. Bostwick, T. Seyller, K. Horn, and E. Rotenberg, *Science* **2006**, 313, 951;

[21] J. B. Oostinga, H. B. Heersche, X. Liu, A. F. Morpurgo and L. M. K. Vandersypen, *Nature Materials* **2007**, 7, 151;

[22] D. C. Elias, R. R. Nair, T. M. G. Mohiuddin, S. V. Morozov, P. Blake, M. P. Halsall, A. C. Ferrari, D. W. Boukhvalov, M. I. Katsnelson, A. K. Geim, and K. S. Novoselov, *Science* **2009**, 323, 610;

[23] R. R. Niar, W. Ren, R. Jalil, I. Riaz, V. G. Kravets, L. Britnell, P. Blake, F. Shedin, A. S. Mayorov, S. Yuan, M. I. Katsnelson, H. –M. Cheng, W. Strupinski, L. G. Bulusheva, A. V. Okotrub, I. V. Grigorieva, A. N. Grigorenko, K. S. Novoselov, and A. K. Geim, *Small*, **2010**, 6, 2877;

[24] F. Zhao, T. T. Nguyen, M. Golsharifi, S. Amakubo, K. P. Loh, and R. B. Jackman, *J. Appl. Phys.* **2013**, 114, 053709

[25] S. V. Morozov, K. S. Novoselov, M. I. Katsnelson, F. Shedin, L. A. Ponomarenko, D. Jiang, and A. K. Geim, *Phys. Rev. Lett.* **2006**, 97, 016801;

[26] Y. Zhang, V. W. Brar, C. Girit, A. Zettl and M. F. Crommie, *Nature Phys.* **2009**, 5, 722;

[27] Y. Niimi, T. Matsui, H. Kambara, K. Tagami, M. Tsukada and H. Fukuyama, *Phys. Rev. B* **2006**, 73; 085421;

[28] T. O. Wehling, A. V. Balatsky, M. I. Katsnelson, A. I. Lichtenstein, K. Scharnberg, and R. Wiesendanger, *Phys. Rev. B* **2007**, 75, 125425;

[29] K. F. Mak, C. Lee, J. Hone, J. Shan, and T. F. Heinz, *Phys. Rev. Lett.* **2010**, 105, 136805;

[30] G. Liu, X. L. Lei, M. S. Wu, B. Xu and C. Y. Ouyang, *EPL*, **2014**, 106, 47001;

[31] H. Liu, A. T. Neal, Z. Zhu, Z. Luo, X. Xu, D. Tománek, and P. D. Ye, *ACS Nano*, **2014**, 8(4), 4033;

[32] Y. Takao, *Physica B+C* **1981**, 105, 93;

Chapter II
Background

2.1 Carbon

Elements of Group 14, led by carbon, have been the essential “backbones” of human modernization. Firstly, carbon has many allotropes: graphite, diamond, fullerene, and amorphous carbon, which offer a plethora opportunities for technology advancement, e.g. electrodes for metallurgical refining processes and energy storage, coatings for cutting tools, lubricants for high temperature processes, supports for catalysts and surfaces for sensing and electronic devices. It is also the essential element in organic compounds, from DNAs, steroids, to proteins. The discoveries of graphene and fullerene lead to two Nobel prizes.[1,2] Secondly, silicon is the key enabler that pushes forward the whole semiconductor industry since the 1950s.[3] Even, the home of many of the world’s largest high-tech corporations is located in the so-called “Silicon” Valley.

The electronic orbitals of carbon are 2*s*, 2p_x, 2p_y and 2p_z. The hybridization of the *s* and the *p* orbitals can lead to 4 tetrahedral sp^3 orbitals or 3 trigonal planar sp^2 orbitals, shown in Figure 2.1. Different structural configurations depend on the degree of *sp* hybridization. sp^2 gives rise to a planar structure, while sp^3 leads to a 3D tetrahedral network.

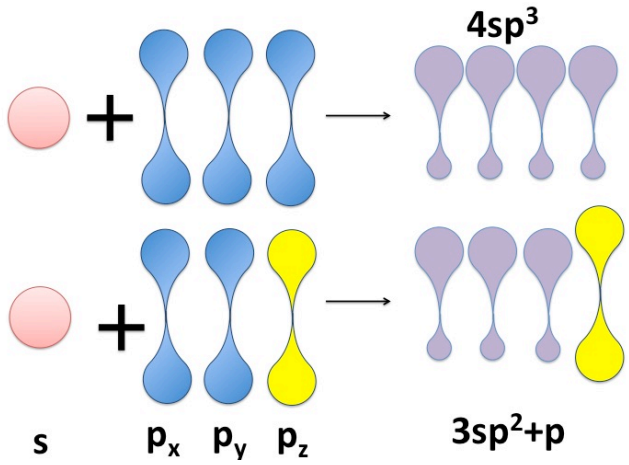

Figure 2.1 Scheme of hybridization of carbon orbitals.

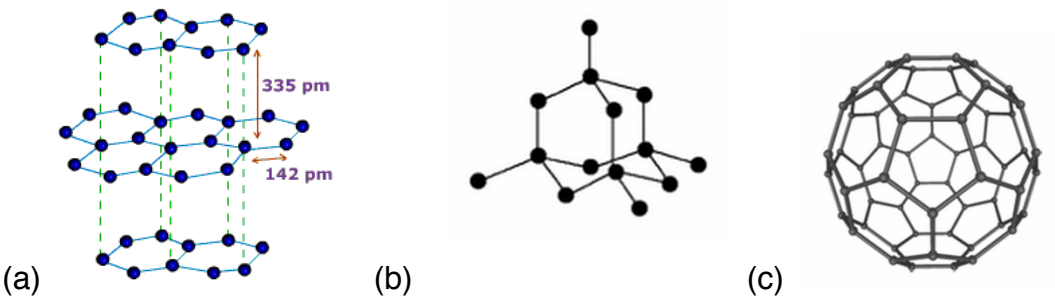

Figure 2.2 Atomic structure of (a) graphite with sp^2 hybridisation; (b) diamond with sp^3 hybridisation; and (c) fullerene with mixed (sp^2+sp^3) hybridisation.

Figure 2.2 gives three common allotropes of carbon, which are graphite, diamond and fullerene. Graphite is characterized by layered structures with weak van der Waals stacking. In-plane carbon atoms form hexagonal structures and bond in sp^2 character. In diamond, all carbon atoms are sp^3 hybridized and each atom occupies four corners of a tetrahedron. The classical buckminsterfullerene (C_{60}) contains pentagonal and hexagonal rings in which no two pentagons share an edge. It has two types of bond, 6:6 double bond and 6:5 single bond with the sp^2 and sp^3 mixed hybridization.

2.2 Graphene

2.2.1 Graphene Structure

Graphene is the first 2D atomic crystal available to mankind.[4] The monolayer carbon atoms form a honeycomb structure through σ bonds (Figure 2.3 (a)). The stability of graphene is due to these covalent bonds. Meanwhile, the p_z orbitals make up the π bond. These weak p_z orbitals overlapped and hybridized together to form the π-bond and π* bond (Figure 2.3(b)). The lattice constant of graphene is 2.461 Å, measured experimentally[5] and 2.465Å in theory.[6]

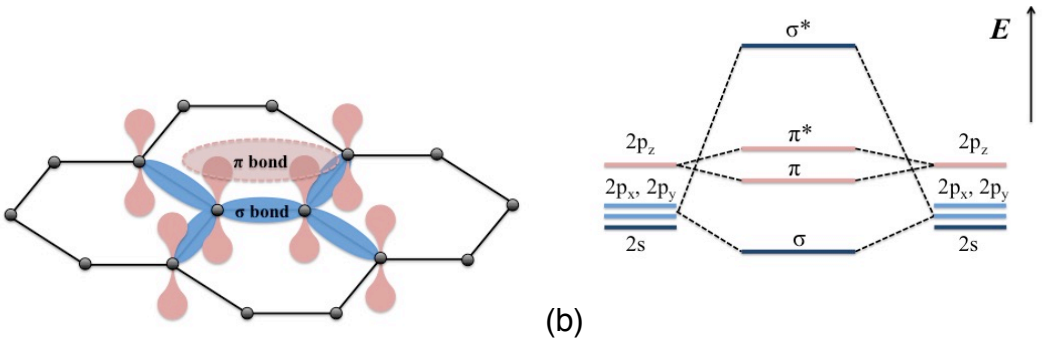

Figure 2.3 (a) Graphene structure and scheme of two types of carbon bonds (b) orbital energy diagram displays the σ and π bonds due to the *sp* hybridization.

2.2.2 Properties of Graphene

2.2.2.1 Electronic Properties

Owing to its unique structure, graphene ~~also~~ exhibits distinguish electronic properties. Figure 2.4 shows the band structure of graphene in 3D and 2D. At special points K and K', conduction band edge meets the valence band edge. Hence, graphene is a zero bandgap material. Meanwhile, energy dispersion at the point shows that both electron and hole are massless.

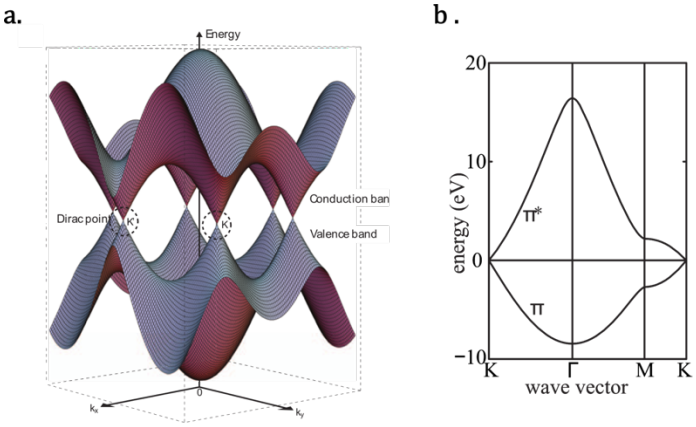

Figure 2.4 (a) Energy dispersion for graphene band structure;[7] (b) Band structure along the points of interest in the First Brillouin zone.[8]

2.2.2.2 Mechanical Properties

Even before graphene was peeled off from graphite, theoreticians had already predicted that graphene would show an ultimate high strength.[9] Lee, *et al.* have measured the elastic properties of free-standing graphene in an atomic force microscope.[10] The results confirm the prediction that graphene is the strongest material ever measured, with Young's modulus E = 1.0 tera-Pascal (TPa), compared with the 32.47 GPa for graphite.[11]

2.2.2.3 Thermal Properties

In solid-state materials, heat is contributed by both electron and core vibrations. For a metal, thermal conduction is mainly contributed by electron vibrations. While carbon materials are dominated by phonons, even for metallic graphite,[12] the intrinsic thermal conductivity K of graphene shows a logarithmic divergence.[13] Theoretically, the lattice thermal conductivity is dominated by contributions from the out-of-plane phonon modes and thermal conductivity can reach 3,400 $Wm^{-1}K^{-1}$.[14] This is much higher than that of graphite, which is 2000 $Wm^{-1}K^{-1}$.[15,16]

2.2.2.4 Optical Properties

An ideal graphene should be transparent due to its zero bandgap. Many scientists attempt to tune its optical properties by means of quantum dots,[17] functionalization, [18] nanostructuring, [19] and hybrid 2D structures. [20, 21, 22] Especially for graphene with other 2D materials, Bernardi, et al., predicts that the graphene/MoS_2 heterostructures can yield efficient properties for solar cells and can boost the power density up to 1,000-10,000 kW/L.[23] There are many other possible combinations to be further explored.

2.2.3 Syntheses of Graphene

2.2.3.1 Mechanical Exfoliation

The first piece of graphene was produced by mechanical exfoliation using a scotch tape.[32] So far, this approach is still employed to produce high-quality samples, but the method is neither of high throughput nor high yield.[24] It only needs to overcome the van der Waals interaction between layers without disturbing others. The calculated exfoliation energy is 57.16 eV/atom. [25] However, this method is unsuitable for massive production in industrial applications.

2.2.3.2 Chemical Vapour Deposition (CVD)

Chemical vapour deposition (CVD) can be applied to grow large-area graphenes using a mixture of methane and hydrogen precursors.[26] It can grow graphene films up to 30 inches so far.[27] Metal foils, copper or nickel films, are normally chosen as the substrate.[26,28] After cooling, these metal foils need to be removed, which make this method expensive. Furthermore, the films also need to be transferred to a Si wafer to build devices. This will further induce defects and cripples.

2.2.3.3 Liquid Exfoliation

Liquid-phase exfoliation of graphite can provide another productive and cost-effective method of producing graphenes.[29] N-methylpyrrolidon (NMP), as a solvent, adds strong interactions between graphite layers. Then using poly vinylidene fluoride (PVDF) to concentrate flakes after centrifugation. Both graphite oxide and pristine graphite can be used as precursors.[29,30] However, researchers have found that approximately only 25% are monolayer graphene.[31] Few-layer graphenes still dominate the exfoliated products.[29]

2.2.4 Applications of Graphene

Graphene has been extensively studied for Field-Effect Transistors (FETs) since 2004.[32] The lack of a bandgap limits its direct consideration for efficient FETs. Many attempts have been made to resolve the problem, but with limited success.[33,34,35,36] In fact, some of those worsen the problem by restricting the on/off ratio and/or carrier mobilities. Only recently, Wu. *et al.* and Yu. *et al.* show high RF frequency and high carrier mobilities of graphene on diamond related substrates.[37,38]

As graphene is transparent, and can also be used to develop a compact, efferent and scalable light source along with a graphene-based optical modulator/detector. By applying strong plasmatic enhancement to improve by up to 20 times of the sensitivity of graphene,[39] a ridge-guided graphene photodetector is able to respond to a broad range of wavelengths covering both O-band (1260-1360 nm) and U-band (1625-1675 nm), which simplifies the integration progress.

Furthermore, owing to its low noise, high sensitivity, chemical stability and biocompatibility, graphene also can be considered for chemical and biological

sensors.[40] The mechanism is principally due to the change of conductivity after the molecules have been absorbed, similar to carbon nanotubes.[41] Both NO_2 and NH_3 lead to an increase of conductivity in graphene.[40,42]

2.2.5 Tailoring Graphene Properties

2.2.5.1 Nanostructuring

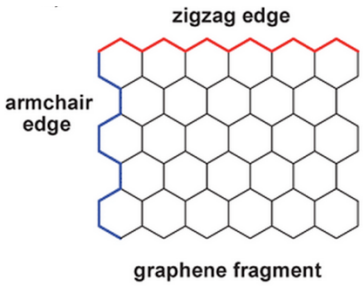

Figure 2.5 Illustration of zigzag and armchair GNR.

Nanostructuring graphene into 1D graphene nanoribbons (GNR) can greatly alter its properties due to the effect of quantum confinement. It can be made using chemical,[43,44,45] sonochemical,[46] lithographic,[47] unzipping of a carbon nanotube,[48,49] and directly synthesis using surface-assisted coupling of molecular precursors,[33] etc. Two typical GNRs have been studies, zigzag-GNR and armchair-GNR (Figure 2.5).[50] Zigzag-GNR is predicted to be half-metallic,[51] and both GNRs exhibit ballistic thermal conductivity.[52] Experimentally etching GNRs also induce energy gaps.[53] Meanwhile, functionalization of the edge of GNRs can further tune their electronic and spin properties.[54]

2.2.5.2 Bilayer Control

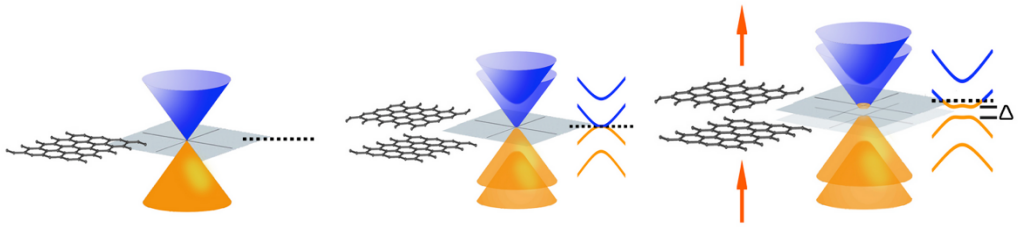

Figure 2.6 Scheme of controlling bilayer graphene to tune bandgap by electrical fields.[55]

Both single layer and bilayer graphenes exhibit a zero bandgap. However, the electronic structure will show asymmetry when an external electrical field is applied perpendicular to its surface, Figure 2.6[56,57,58] Another way of tuning the bandgap is by chemical doping to adjust the carrier concentration in each layer to induce asymmetry.[59,60,61] However, both methods either need a low-temperature environment or dual gate control, which makes it hard to integrate graphene in a circuit.

2.2.5.3 Doping and Defects

Creating size-controlled nanopores and nanopore functionalization can fundamentally tailor the properties of graphene.[62,63] There are two fundamental methods behind the synthesis methodology. One is to punch nanopores on graphene sheet using focused ion bombardment,[64] ultraviolet-induced oxidative etching,[65] or plasma etching.[66] The other is to create defects and nanopores from the beginning of synthesis by surface-assisted coupling.[67,68] Point defects, such as single vacancy, double vacancy and Stone-Wales defect, have been intensively studied.[69,70] Nitrogen and boron, which are the neighbouring elements, are commonly selected as dopants to tune the properties of graphene. Doping of N- or B- into graphene can be realized through direct syntheses, such as CVD,[71] segregation,[72] solvothermal,[73] and arc-discharge[74] methods. It is also possible to introduce

such dopants in post-synthesis approaches.[75,76] However, for large-scale synthesis, controlling dopant distribution and distortion are major issues.

2.3 Phosphorene

2.3.1 Phosphorous

The element phosphorus has the electron configuration, [Ne] $3s^2$ $3p^3$. It exists in several allotropes. White phosphorus is the most reactive and unstable form, which consists of P_4 molecules (Figure 2.7(a)) and can be easily degenerated into P_2 molecules. Red phosphorus is a polymeric material with an amorphous network (Figure 2.7(b)). It can also be considered as the intermediate between the white and violet phosphorous. The violet phosphorus (Figure. 2.7(c)) is of a monoclinic or rhombohedral crystal structure. Finally, but not the least, black phosphorus consists of a weakly stacked layered quasi-planar corrugated half-honeycomb (or puckered) structure (Figure 2.7 (d)). Black phosphorus was first synthesized in 1914 by means of a high hydrostatic pressure (12 Kbar) at 200 °C.[77] Unlike white or red phosphorus, it shows chemical stability and can sustain up to 400 °C in the air without spontaneous degradation.[77] More importantly, this p-type semiconductor has a direct bandgap of 0.35 eV and resistivity around 1 Ωcm.[78] At room temperature, the electron and hole mobility is ≈ 1000 $cm^2V^{-1}s^{-1}$ and could exceed 15,000 $cm^2V^{-1}s^{-1}$ for electrons and 50,000 $cm^2V^{-1}s^{-1}$ for holes at low temperature.[79]

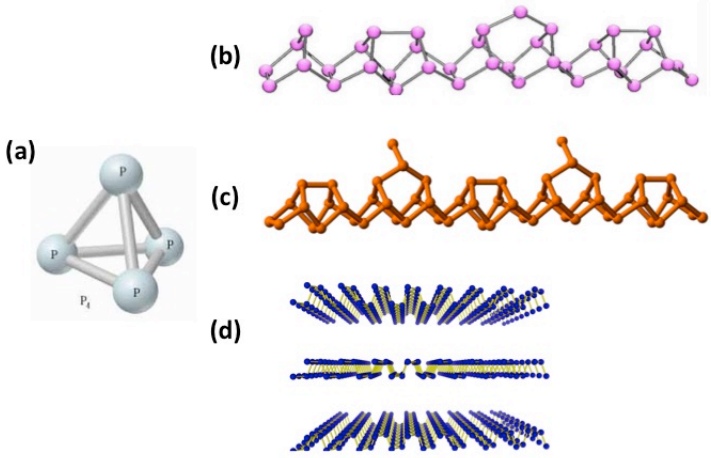

Figure 2.7 Atomic structures of four different allotropes of phosphorus (a) white phosphorus (b) red phosphorus (c) violet phosphorus (d) black phosphorus

2.3.2 Phosphorene

Recently, phosphorene, a monolayer of the black phosphorus, has been exfoliated using the scotch tape peeling method, similar to peeling of graphene from graphite.[80,81] However, unlike graphene, phosphorene has an inherent, direct and appreciable bandgap of 1.55 eV, potentially interesting for a wide range of electronic and optoelectronic devices.[82] Moreover, its bandgap is also layer depended [83, 84] and can be further tuned by nanostructuring into nanoribbons.[82, 85] Experimentally, a high field-effect mobility μ_{FE} =286 $cm^2V^{-1}s^{-1}$, and can reach 1,430 $cm^2V^{-1}s^{-1}$ at low temperature, improved by a factor of 5.[80] Due to its unique structure, phosphorene exhibits anisotropic transportation and mechanical stability.[82,86] The previous study shows that the Raman intensities of B_{2g} and A_g^2 modes are significantly dependent on the polarization angle.[87] The theoretical study also reveals that the effective mass is angle-dependent.[88] Meanwhile, these transportation properties are also sensitive to the strain. The report shows that +2% compression along zigzag direction will trigger a direct-to-indirect bandgap transition. [89]

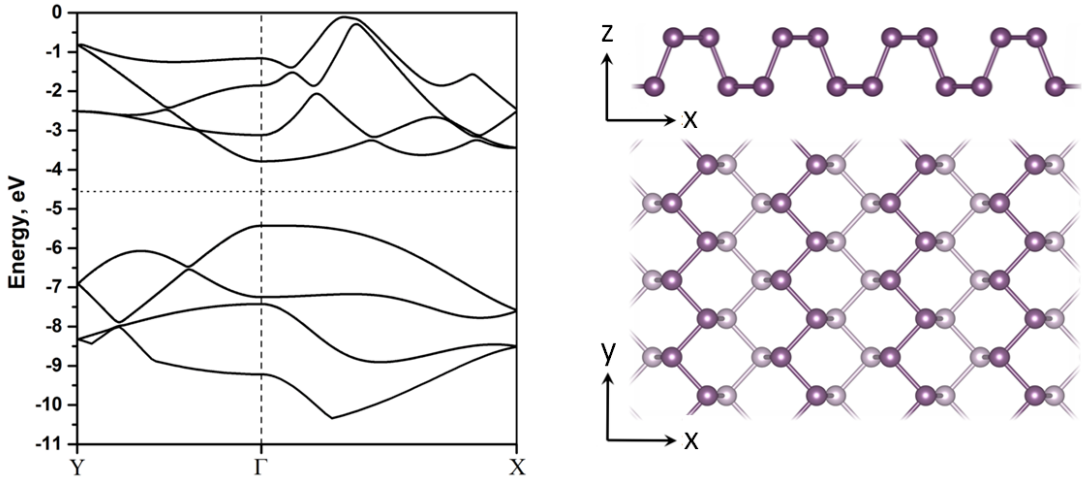

Figure 2.8 The band structure of single layer phosphorene (left) and its structure side view (top) and top view(bottom).

Those interesting and unique properties have led to a surge of interest from many scientists and many potential applications have been explored, especially for electronic devices. Back-gated black phosphorus Field Effect Transistors (FETs) have been made on heavily doped silicon.[80] Both field effect mobility and Hall mobility show temperature dependence.[81] Researchers also construct a p-n diode with phosphorene/h-BN heterojunction.[90] The heterojunction attracts wavelengths up to 940 nm. As 90% of solar energy within the wavelength range of 380-980 nm, it is potentially ideal for solar energy harvesting.

However, there exist some remaining challenges: 1) Is it possible to synthesize this material at industrial scale? What is the nature of the strongly anisotropic conducting behaviour, *e.g.* the drain current is strongly angular dependent.[71] And what are the effects of nanostructuring on the electronic and optical properties of this material? To answer the last two questions, theoretical simulations were carried out here, and the results are illustrated in Chapter 6.

References

[1] H. Kroto, *Nobel Lecture*, December 7, 1996, p.45;

[2] Editorial, *Nature Material,* **2011**, 10, 1;

[3] http://mastse1.mastse.illinois.edu/sc/prin.html

[4] K.S. Novoselov, V. I. Fal'ko, L. Colombo, P. R Gellert, M. G. Schwab and K. Kim, *Nature*, **2012**, 490, 192;

[5] H. Hattab, A. T. N'Diaye, D. Wall, C. Klein, G. Jnawali, J. Coraux, C. Busse, R. van Gastel, B. Poelsema, T. Michely, F-J. M. zu Heringdorf and M. Horn-von Hoegen, *Nano Lett.* **2012**, 12, 678;

[6] D. –E. Jiang, M. –H. Du, and S. Dai, *J. Chem. Phys.* **2009**, 130, 074705;

[7] T. Ando, *NPG Asia Materials*, **2009**, 1, 17;

[8] I. Thomas, *Semiconductor Nanostructures: The Quantum States and Electronic Transport,* Oxford University Press (**2010**);

[9] Q. Zhao, M. B. Nardelli, and J. Bernholc, *Phys. Rev. B* **2002**, 65, 144105;

[10] C. Lee, X. Wei, J. W. Kysar, J. Hone, *Science,* **2008**, 321, 385;

[11] Y. Qi, H. Guo, Jr. L. G. Hector, and A. Timmons, *J. Electrochem. Soc.* **2010**, 157(5), A558;

[12] P. G. Klemens, *J. Wide Bandgap Mater.* **2000**, 7, 332;

[13] A. A. Balandin, *Nature. Materials*, **2011**, 10, 569;

[14] L. Lindsay, D. A. Broido, and N. Mingo, *Phys. Rev. B.* **2010**, 82, 115427;

[15] C. Y. Ho, R. W. Powell, P. E. Liley, *J. Phys. Chem. Ref. Data,* **1972**, 1(2), 279;

[16] G. Fugallo, A. Cepellotti, L. Paulatto, M. Lazzeri, N. Marzari, and F. Mauri, *Nano Lett.* **2014**, 14(11), 6109;

[17] Z. Z. Zhang, Kai Chang, and F. M. Peeters, *Phys. Rev. B,* **2008**, 77, 235411;

[18] Z. –B. Liu, Y. –F. Xu, X. –Y. Zhang, X. –L. Zhang, Y. –S. Chen, and J. –G. Tian, *J. Phys. Chem. B* **2009**, 113(29), 9681;

[19] Y. C. Huang, C. P. Chang, and M. F. Lin, *Nanotechnology*, **2007**, 18, 495401;

[20] K. Roy, M. Padmanabhan, S. Goswami, T. P.Sai, G. Ramalingam, S. Raghavan and A. Ghosh, *Nature Nanotechnology*, **2013**, 8, 826;

[21] Y. Shi, W. Zhou, A. –Y. Lu, W. Fang, Y. –H. Lee, A. L. Hsu, S. M. Kim, K. K. Kim, H. Y. Yang, L. –J. Li, J. –C. Idrobo, and J. Kong, *Nano Letts,* **2012**, 12(6), 2784;

[22] L. Ci, L. Song, C. Jin, D. Jariwala, D. Wu, Y. Li, A. Srivastava, Z. F. Wang, K. Storr, L. Balicas, F. Liu, and P. M. Ajayan, *Nature Materials*, **2010**, 9, 430;

[23] M. Bernardi, M. Palummo, and J. C. Grossman*, Nano Letts.* **2013**, 13, 3664;

[24] M. J. Allen, V. C. Tung, and R. B. Kaner, *Chem. Rev.* **2010**, 110, 132;

[25] X. Chen, F. Tian, C. Persson, W. Duan, and N. –X. Chen, *Sci. Rep.* **2013**, 3, 3046;

[26] X. Li, W. Cai, J. An, S. Kim, J. Nah, D. Yang, R. Piner, A. Velamakanni, I. Jung, E. Tutuc, S. K. Banerjee, L. Colombo, and R. S. Ruoff, *Science*, **2009**, 324, 1312;

[27] S. Bae, H. Kim, Y. Lee, X. Xu, J. –S. Park, Y. Zheng, J. Balakrishnan, T. Lei, H. R. Kim, Y. I. Song, K. S. Kim, B. Özyilmaz, J. –H. Ahn, B. H. Hong and S. Lijima, *Nature Nanotechnology,* **2010**, 5, 574;

[28] S. J. Chae, F. Günes, K. K. Kim, E. S. Kim, G. H. Han, S. M. Kim, H. –J. Shin, S. –M. Yoon, J. –Y. Choi, M. H. Park, C. W. Yang, D. Pribat, and Y. H. Lee, *Adv. Mater.* **2009**, 21, 2328;

[29] Y. Hernandez, V. Nicolosi, M. Lotya, F. M. Blighe, Z. Sun, S. De, I. T> McGovern, B. Holland, M. Byrne, Y. K. Gun'Ko, J. J. Boland, P. Nirag, G. Duesberg, S. Krishnamurthy, R. Goodhue, J. Hutchison, V. Scardaci, A. C. Ferrari, and J. N. Coleman, *Nature,* **2008**, 3, 563;

[30] V. C. Tung, M. J. Allen, Y. Yang and R. B. Kaner, *Nature Nanotechnology*, **2008**, 4, 25;

[31] J. N. Coleman, *Accounts of Chemical Research,* **2013**, 46, 14;

[32] K. S. Novoselov, A. K. Geim, S. V. Morozov. D. Jiang, Y. Zhang, S. V. Dubonos, I. V. Grigorieva, and A. A. Firsov, *Science*, **2004**, 306, 666;

[33] J. Cai, P. Ruffieux, R. Jaafar, M. Bieri, T. Braun, S. Blankenburg, M. Muoth, A. P. Seitsonen, M. Saleh, X. Feng, K. Müllen and R. Fasel, *Nature*, **2010**, 466, 470;

[34] M. Y. Han, B. Özyilmaz, Y. Zhang, and P. Kim, *Phys. Rev. Lett.* **2007**, 98, 206805;

[35] C. Stampfer, E. Schurtenberger, F. Molitor, J. Güttinger, T. Lhn and K. Ensslin, *Nano Lett.* **2008**, 8(8), 2378;

[36] K. Kim, J. –Y. Choi, T. Kim, S.-H. Cho and H. –J. Chuang, *Nature*, **2011**, 479, 338;

[37] Y. Wu, Y. –M. Lin, A. A. Bol, K. A. Jenkins, F. Xia, D. B. Farmer, Y. Zhu, and P. Avouris, *Nature*, **2011**, 472, 74;

[38] J. Yu, G. Liu, A. V. Sumant, V. Goyal and A. Balandin, *Nano Lett.* **2012**, 12, 1603;

[39] T. J. Echtermeyer, L. Britnell, P. K. Jasnos, A. Lombardo, R. V. Gorbachev, A. N. Grigorenko, A. K. Geim, A. C. Ferrari, and K. S. Novoselov, *Nature Commun.* **2011**, 2, 458;

[40] J. D. Fowler, M. J. Allen, V. C. Tung, Y. Yang, R. B. Kaner, and B. H. Weiller, *ACS Nano*, **2009**, 3(2), 301;

[41] J. Kong, N. R. Franklin, C. Zhou, M. G. Chapline, S. Peng, K. Cho, and H. Dai, *Science*, **2000**, 287, 662;

[42] F. Schedin, A. K. Geim, S. V. Morozov, E. W. Hill, P. Blake, M. I. Katsnelson, and K. S. Novoselov, *Nature Materials* **2007**, 6, 652;

[43] S. S. Datta, D. R. Strachan, S. M Khamis, and A. T. C. Johnson, *Nano Lett.* **2008**, 8, 1912;

[44] J. Campos-Delgado, J. M. Romo-Herrera, X. Jia, D. A. Cullen, H. Muramatsu, Y. A. Kim, T. Hayashi, Z. Ren, D. J. Smith, Y. Okuno, T. Ohba, H. Kanoh, K. Kaneko, M. Endo, H. Terrones, M. S. Dresselhaus, and M. Terrones, *Nano Lett.* **2008**, 8(9), 2773;

[45] X. Yang, X. Dou, A. Rouhanipour, L. Zhi, H. J. Räder, and K. Müllen, *J. Am. Chem. Soc.* **2008**, 130(13), 4216;

[46] X. L. Li, X. R. Wang, L. Zhang, S. W. Lee and H. J. Dai, *Science*, **2008**, 319, 1229;

[47] M. Y. Han, B. Ozyilmaz, Y. B. Zhang, and P. Kim, *Phys. Rev. Lett.* **2007**, 98, 206805;

[48] L. Jiao, L. Zhang, X. Wang, G. Diankov, H. Dai, *Nature*, **2009**, 458, 877;

[49] L. Jiao, X. Wang, G. Diankov, H. Wang and H. Dai, *Nature nanotechnology*, **2010**, 5, 321;

[50] X. Jia, M. hofmann, V. Meunier, B. G. Sumpter, J. Campos-Delgaso, J. M. Romo-Herrera, H. Son, Y. –P. Hsieh, A. Reina, J. Kong, M. Terrones, M. S. Dresselhaus, *Science*, **2009**, 323, 1701;

[51] Y. –W. Son, M. L. Cohen, and S. G. Louie, *Nature*, **2006**, 444, 347;

[52] E. Muñoz, J. Lu, and B. I. Ykobson, *Nano Lett.* **2010**, 10, 1652;

[53] C. Stampfer, J. Güttinger, S. Hellmüller, F. Molitor, K. Ensslin, and T. Ihn, *Phys. Rev. Lett.* **2009**, 102, 056403;

[54] F. Cervantes-Sodi, G. Csanyi, S. Piscanec, A. C. Ferrari, *Phys. Rev. B*, **2008**, 77, 165427;

[55] http://newscenter.lbl.gov/2009/06/10/graphene-bandgap/

[56] E. McCann, *Phys. Rev. B*, **2006**, 74, 16143;

[57] H. K. Min, B. Sahu, S. K. Banerjee, A. H. MacDonald, *Phys. Rev. B*, **2007**, 75, 155115;

[58] Y. Zhang, T.-T. Tang, C. Girit, Z. Hao, M. C. Martin, A. Zettle, M. F. Crommie, Y. R. Shen and F. Wang, *Nature*, **2009**, 459, 820;

[59] T. Ohta, A. Bostwick, T. Seyller, K. Horn, and E. Rotenberg, *Science*, **2006**, 313, 951;

[60] S. Y. Zhou, G. –H. Gweon, A. V. Fedorov, P. N. First, W. A. de Heer, D. –H. Lee, F. Guinea, A. H. Castro Neto and A. Lanzara, *Nature Materials*, **2007**, 6, 770;

[61] E. V. Castro, K. S. Novoselov, S. V. Morozov, N. M. R. Peres, J. M. B. Lopes ods Santos, J. Nilsson, F. Guinea, A. K. Geim, and A. H. Castro Neto, *Phys. Rev. Lett.* **2007**, 99, 216802;

[62] A. K. Geim, *Science*, **2009**, 324, 1530;

[63] T. Kuila, S. Bose, A. K. Mishra, P. Khanra, N. H. Kim, and J. H. Lee, *Prog. Mater. Sci.* **2012**, 57, 1061;

[64] K. Celebi, J. Buchheim, R. M. Wyss, A. Droudian, P. Gasser, I. Shorubalko, J. –I. Kye, C. Lee, and H. G. Park, *Science*, **2014**, 344, 95;

[65] S. P. Koenig, L. Wang, J. Pellegrino, and J. S. Bunch, *Nature. Nanotechnol.* **2012**, 7, 728;

[66] H. M Jeong, J. W. Lee, W. H. Shin, Y. J. Choi, H. J. Shin, J. K. Kang, and J. W. Choi, *Nano Lett.* **2011**, 11, 2472;

[67] P. Kuhn, M. Antonietti, A. P. Thomas, *Angew. Chem. Int. Ed. Engl.* **2008**, 47, 3450;

[68] S. Blankenburg, M. Bieri, R. Fasel, K. Müllen, C. A. Pignedoli, and D. Passerone, *Small*, **2010**, 6, 2266;

[69] F. Banhart, J. Ktakoski, and A. V. Krasheninnikov, *ACS Nano*, **2011**, 5(1), 26;

[70] N. Jing, Q. Xue, C. Ling, M. Shan, T. Zhang, X. Zhou, and Z. Jiao, *RSC Adv.* **2012**, 2, 9124;

[71] A. L. M. Reddy, A. Srivastava, S. R. Gowda, H. Gullapalli, M. Dubey, and P. M. Ajayan, *ACS Nano*, **2010**, 4, 6337;

[72] C. Zhang, L. Fu, N. Liu, M. Liu, Y. Wang, Z. Liu, *Adv. Mater.* **2011**, 23,1020;

[73] D. Deng, X. Pan, L. Yu, Y. Cui, Y. Jiang, J. Qi, W. X. Li, Q. FU, X. Ma, Q. Xue, G. Sun, and X. Bao, *Chem. Mater.*, **2011**, 23, 1188;

[74] L. S. Panchakarla, K. S. Subrahmanyam, S. K. Saha, A. Govindaraj, H. R. Krishnamurthy, U. V. Waghmare, C. N. R. Rao, *Adv. Mater.* **2009**, 21, 4726;

[75] L. S. Zhang, X. Q. Liang, W. G. Song, Z. Y. Wu, *Phys. Chem. Chem. Phys.* **2010**, 12, 12055;

[76] X. Li, H. Wang, J. T. Robinson, H. Sanchez, G. Diankov, H. Dai, *J. Am. Chem. Soc.* **2009**, 131, 15939;

[77] P. W. Bridgeman, *J. Am. Chem. Soc* **1914**, 36, 1344;

[78] Y. Maruyama, S. Suzuki, K. Kobayashi, and S. Tanuma, *Physica B+C*, **1981**, 105, 99;

[79] A. Morita, *Appl. Phys. A: Mater. Sci. Phrocess*, **1986**, 39, 227;

[80] H. Liu, A. T. Neal, Z. Zhu, Z. Luo, X. Xu, D. Tománek and P. D. Ye, *ACS Nano*, **2014**, 8(4), 4033;

[81] L. Li, Y. Yu, G. J. Ye, Q. Ge, X. Ou, H. Wu, D. Feng, X. H. Chen, and Y. Zhang, *Nature Nanotech.* **2014**, 9, 372;

[82] X. Han, H. Morgan Stewart, S. A. Shevlin, C. R. A. Catlow, and Z. X. Guo, *Nano Lett.* **2014**, 14(8), 4607;

[83] Y. Cai, G. Zhang, and Y. –W. Zhang, *Sci. Rep.* **2014**, 4, 6677;

[84] V. Tran, R. Soklaski, Y. Liang, and L. Yang, *Phys. Rev. B*, **2014**, 89, 235319;

[85] V. Tran and L. Yang, *Phys. Rev. B*, **2014**, 89, 245407;

[86] F. Xia, H. Wang, and Y. Jia, *Nat. Commun.* **2014**, 5, 4458;

[87] S. Zhang, J. Yang, R. Xu, F. Wang, W. Li, M. Ghufran, Y. –W. Zhang, Z. Yu, G. Zhang, Q. Qin, and Y. Lu, *ACS Nano*, **2014**, 8(9), 9590

[88] R. Fei and L. Yang, *Nano Lett.* **2014**, 14, 2884;

[89] X. Peng, Q. Wei, A. Copple, *Phys. Rev. B*, **2014**, 90, 085402;

[90] M. Buscema, D. J. Groenendijk, G. A. Steele, H. S. J. van der Zant and A. Castellanos-Gomez, *Nature Commun.* **2014**, 5, 4651;

Chapter III
Simulation Principles and Methodology

In this chapter, a brief introduction to the theoretical methodology used in the simulations is provided. The coverage includes the fundamental theory based on the *ab-initio* method, the well developed and practiced density functional theory (DFT), and newly improved van der Waals corrected vdW-DF.

3.1 *Ab-initio* method

3.1.1 Schrödinger Equation

From a quantum physics point view, a quantum state of a physical system can be described by its Schrödinger Equation (Eq. 1), associated with its Hamiltonian (Eq. 2).

$$E\Psi(\mathbf{r}) = -\frac{\hbar^2}{2m}\nabla^2\Psi(\mathbf{r}) + V(r)\Psi(\mathbf{r}) \qquad \text{Eq. 1}$$

where Ψ is the time-independent wave function, ħ is reduced Planck's constant, V(r) is the potential, and the Hamiltonian operator is

$$\hat{H} = -\frac{\hbar^2}{2m}\nabla^2 + V(r) \qquad \text{Eq. 2}$$

Many properties of a physical system can, in theory, be derived from this fundamental relationship. However, only a single H atom can be analytically resolved to obtain its exact Hamiltonian solutions. Computational simulations have to be applied to material problems in both static and dynamic circumstances. There are different simulation approaches to approximate the solutions. Among those, the *ab-initio* quantum chemistry method is the one that does not include any empirical or semi-empirical parameters in its calculation, though some approximations are necessary to make such simulations viable while sufficiently accurate for prediction and design of materials with desirable properties.[1] Those concepts are briefly introduced below.

3.1.2 Born-Oppenheimer approximation

Most of the *ab-initio* methods rely on the Born-Oppenheimer approximation (Eq. 3), which allows the wavefunction of a molecule to be broken into two parts: electronic and nuclear components. Due to the large ratio between the nuclear and electronic masses, the Born-Oppenheimer approximation neglects the kinetic energy of nuclei. (Eq. 4) The Born-Oppenheimer approximation can be simplified into two steps. The first step is referred to as the "clamped nuclei" approximation, in which the nuclear kinetic energy is neglected. Therefore, all the electrons' Hamiltonian components can be represented in nuclear coordinates and under their Coulomb potentials (Eq. 4). The separation allows the calculation of a solution involving the electrons first.

$$\Psi_{total} = \Psi_{electronic} \times \Psi_{nuclear} \qquad \textbf{Eq. 3}$$

$$\hat{H} = \hat{H}_{ee} + \hat{H}_{eN} + \hat{H}_{NN} = -\sum_i \frac{\hbar^2}{2m_e}\nabla_i^2 + \frac{1}{2}\sum_{i,j\ (i\neq j)} \frac{e^2}{|r_i - r_j|} - \sum_{i,I} \frac{Z_I e^2}{|r_i - r_I|} + \frac{1}{2}\sum_{I,J\ (I\neq J)} \frac{Z_I Z_J e^2}{|R_I - R_J|} \qquad \textbf{Eq. 4}$$

where the $\hat{H}_{ee}$ is the Hamiltonian of the kinetics of electron and electron-electron interaction, $\hat{H}_{eN}$ is the Hamiltonian of the interaction of the electron with nuclei, and $\hat{H}_{NN}$ is the Hamiltonian of the nuclear-nuclear interaction.

The second step is to reintroduce the nuclear kinetic energy to the Schrödinger Equation of the whole system including the results from the first step (Eq. 5).

$$(T_{nuclear} + E_e)\Psi = E\Psi \qquad \textbf{Eq. 5}$$

where the $T_{nuclear}$ is the kinetic energy of nuclei, including vibration and rotation, E_e is the eigenvalue energy resulting from the first step, and E is the total energy of the whole system.

3.1.3 Slater Determinant

For an N-electron system, i.e. a multi-fermion system, the wave function can be described in a Slater determinant (Eq. 6) that satisfies anti-symmetry requirements, according to the Pauli exclusion principle. For a two-particle's case with coordinates X_1, X_2, the wavefunction satisfies $\Psi(\mathrm{X}_1, \mathrm{X}_2) = -\Psi(\mathrm{X}_2, \mathrm{X}_1)$. An N-electron system can also be generalized to any number of electrons under the Hartree-Fock method, where it applied the Fock operator on the matrix (Eq. 6) and made the approximation under the electron-electron repulsion condition and neglect nuclear-nuclear repulsion.

$$\Psi(x_1, x_2, \dots, x_N) = \frac{1}{\sqrt{N!}} \begin{bmatrix} \chi_1(x_1) & \chi_2(x_1) & \cdots & \chi_N(x_1) \\ \chi_1(x_2) & \chi_2(x_2) & \cdots & \chi_N(x_2) \\ \vdots & \vdots & \ddots & \vdots \\ \chi_1(x_N) & \chi_2(x_N) & \cdots & \chi_N(x_N) \end{bmatrix} \equiv |\chi_1 \chi_2 \cdots \chi_N| \qquad \textbf{Eq. 6}$$

The Hartree-Fock (HF) method needs to find the determinant by minimization of the total energy of the fully interacting Hamiltonian, in order to obtain the wavefunction. This method is given rise from deviations from mean field approximation, which are completely neglected for the electron of opposite spin. Hence, the correlation energy is not included, which can lead to large variations from the experimental results. To tackle this problem, post-HF

methods give more accurate results by including approximated electron correlation energy, although with a large computational penalty.

3.2 Density Functional Theory (DFT)

It is difficult to resolve the electronic structures of atoms, molecules, and solids because electrons must follow the quantum mechanism, not the classical one. As a number of electrons increases, the system becomes more complicated. Density Functional Theory (DFT) is to solve the Schrödinger Equation depending on electron density. It is a powerful tool to investigate the electronic structure of atoms, molecules, and condensed states. For many body systems, density functional theory, which employs an exchange-correlation functional (functional of the density of the electrons) and the Pauli principle, simplifies the problems into a single electron system.

The main advantage of this method is to balance the accuracy and computational cost by means of the approximation of the exchange-correlation functionals.

3.2.1 Thomas-Fermi method

The Thomas-Fermi method and Hartree-Fock-Slater method are both considered as the pioneers of the modern density functional theory. Though these methods solved the Schrödinger Equation approximately, they gave comparably accurate results according to the ground states. For Thomas-Fermi approximation, the basic idea is the total energy of the system E can be written as a formula in terms of the electronic density $\rho(r)$, and the ground state energy obtained by the minimization of E with respect to $\rho(r)$. The total energy is then:

$$E_{tot} = \frac{\alpha^2}{\hbar} m \int \rho(r)^{5/3} dr + \int V(r)\rho(r) dr + \frac{e^2}{8\pi\epsilon_0} \int dr dr' \frac{\rho(r)\rho(r')}{|r - r'|} - \frac{\beta e^2}{4\pi\epsilon_0} \int \rho(r)^{4/3} dr \quad \text{Eq. 7}$$

where $\alpha = \frac{3}{10}(3\pi^2)^{2/3}$ and $\beta = \frac{3}{4}\left(\frac{3}{\pi}\right)^{1/3}$. The first term of Eq. 7 is the electron kinetic energy, followed by the electron Columbus energy under the potential *V(r).* The third term is called Hartree energy, which is contributed by the different parts of the charge distribution interaction. The final one is the exchange energy. As a universal condition, the total electron density is constant, i.e.

$$\int \rho(r) dr = N \quad \text{Eq. 8}$$

And the solution can be solved by performing the first order variation, the minimization condition is

$$\delta E - \mu \delta N = 0 \quad \text{Eq. 9}$$

However, the Thomas-Fermi approximation still has its limitations, including the inaccuracy of the kinetic energy and omission of the correlation energy, which is the energy difference between the exact energy and Hartree-Fock energy. Furthermore, Thomas-Fermi theory assumes that specifying the electron density *ρ(r)* by itself is enough to uniquely determine the ground state.

Here, the Hohenberg-Kohn Theorem has justified as its Theorem as follows.[2]

Theorem 1 *It is impossible that two external potentials v(**r**) and v'(**r**) whose difference v'(**r**) -v(**r**) is not a constant given rise to the same ground state density distribution ρ(**r**).*

In another word, for any system of interacting particles in an external potential $V_{ext}(\mathbf{r})$, the density is uniquely determined, i.e. the external potential is a unique functional of the density.

Theorem 2 *The ground state energy that can be obtained varies. For any particular external potential $V_{ext}(\mathbf{r})$ and fixed N, the ground state energy of the system is the global minimum of this functional.*

3.2.2 Kohn-Sham equation

From previous Thomas-Fermi theory, and Hohenberg-Kohn theorems, the total energy can be written as:

$$E_{tot} = \int dr\rho(r)v(r) + T[\rho(r)] + E_{Har} + E_{ex} \qquad \text{Eq. 10}$$

Then,

$$\delta E = 0 = \int dr[v(r) + \frac{\delta T}{\delta\rho(r)} + \frac{\delta(E_{Har}+E_{xc})}{\delta\rho(r)}]\delta\rho(r) \qquad \text{Eq. 11}$$

The vibrational equation should be satisfied for any arbitrary $\delta\rho(\mathbf{r})$. Therefore,

$$\frac{\delta T}{\delta\rho(r)} + v_{eff}(r) = \mu \qquad \text{Eq. 12}$$

where, the so-called effective energy

$$v_{eff}(r) = v(r) + \frac{\delta(E_{Har}+E_{xc})}{\delta\rho(r)} \qquad \text{Eq. 13}$$

which is also known as the Kohn-Sham potential. At the same time, for non-interacting electron, $E_{Har} + E_{ex} = 0$. Therefore, the ground stat condition should be

$$\frac{\delta T}{\delta \rho(r)} + v(r) = \mu \qquad \textbf{Eq. 14}$$

So the interacting system with external potential *v(r)* is equal to the non-interacting system with the external potential $v_{eff}(r)$. The complex Schrödinger Equation can then be simplified into

$$\left[-\frac{\hbar^2}{2m}\nabla^2 + v_{eff}(r)\right]\psi_n(r) = \epsilon_n \psi_n(r) \qquad \textbf{Eq. 15}$$

The Kohn-Sham method simplifies a many body system into a single electron equation and is literally similar to the Schrödinger Equation. It has great advantages than Thomas-Fermi method because almost all the kinetic energy is treated exactly. Moreover, it can also include other properties of the system in the ground state, such as lattice parameter, binding energies, etc.

DFT can be widely used in surface science, nano-materials, bio-materials, and geo-physics. However, there are still some deficiencies in DFT. For example, it cannot solve the exited states; the calculated bandgaps of semiconductors are 50%-100% lower than the experimental data, because of the constructive failure of derivatives of the discontinuity of the exchange and correlation functionals; it also cannot deal with the van der Waals forces, etc.[3]

3.2.3 Approximations of the Exchange-Correlation Functionals – LDA/GGA/PBE/PBEsol functionals

The local density approximation (LDA) functional is the simplest approximation functional.[4] It treats a general inhomogeneous electronic density as a locally homogeneous one.

$$E_{ex}^{LDA}[\rho(r)] = \int dr\rho(r)\varepsilon_{xc}^{unif}[\rho(r)\,] \qquad \textbf{Eq. 16}$$

It very successfully predicts systems with a uniform electronic density, such as bulk metals. However, this functional has its limitations. For those systems in which the electronic density rapidly varies, such as molecules and surfaces, it fails to interpreter the electronic density changes.

To improve the LDA and keep it linear, a generalized gradient approximation (GGA) functional is introduced by an expansion of the density in terms of its gradient of the density.[5,6]

$$E_{xc}^{GGA}[\rho(r)] = \int dr\rho(r)\varepsilon_{xc}^{unif}\{\rho(r)F_x[s(r)]\} \qquad \textbf{Eq. 17}$$

where $s = \frac{|\nabla n|}{2k_F n}$, and F_x is the exchange enhancement factor (Figure 3.1) that gives the different enhancement factors according to different GGA functionals.

The PBE exchange-correlation functional is proposed by Perdew, Burke, and Ernzerhof, which improved PW91-GGA with an accurate description of the linear responses of the uniform electron density and smoothed potential.[7,8] Recently, a newly functional, PBEsol was introduced. It has specifically improved the equilibrium properties of densely packed solid and its surfaces.[9]

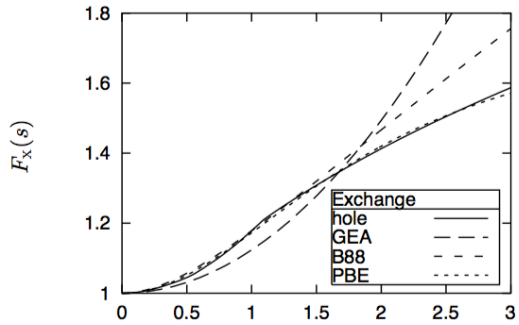

Figure 3.1 Exchange enhancement factors for different GGA's. [10]

3.3 vdW-DFT

The van der Waals force is a relatively weak interaction in physical chemistry, compared to covalent bonds, hydrogen bonds, or electrostatic interaction. It includes Keesom force (between two permanent dipoles), Debye force (between a permanent and an induced dipoles) and London dispersion force (between instantaneously induced dipoles). The last one, also well known as London forces, is induced by interactive forces between instantaneous di-poles or multi-poles in molecules without permanent multi-pole moments. The description of London forces is illustrated in Eq. 18, which is the term of both dipole polarizabilities and ionization potentials in relation to $-1/R^6$. Though it is not compatible to covalent bonds, it is dominant in certain circumstances and exhibits a unique phenomenon, such as the binding of biomolecules, molecular crystals, and molecules on surfaces.[11] It is also the force that holds graphite layers together.

$$E_{AB}^{disp} \approx -\frac{3}{2}\frac{I_A I_B}{I_A + I_B}\frac{\alpha^A \alpha^B}{R^6} \qquad \text{Eq. 18}$$

The standard density functional theory has successfully solved many-body solid-state problems, approximating the electron interaction with the

exchange-correlation functionals. However, it is still a challenge to use such local functionals to accurately describe the nonlocal electron dispersion for two reasons. First, the exchange-correlation functionals provide a mean field approach in which an electron interacts with the total electron density. While dispersion interaction is based on the instantaneous electron positions.[12] The other reason is that the simulation calculates the binding or repulsion only when the electron density is overlapped. It neglects the long distance interaction, such as attractive London force.[13] As shown in Figure 3.2, the classical PBE exchange-correlation functional gives an exponential decay with an underestimated binding energy, compared with the accurate that exhibits $-1/R^6$.

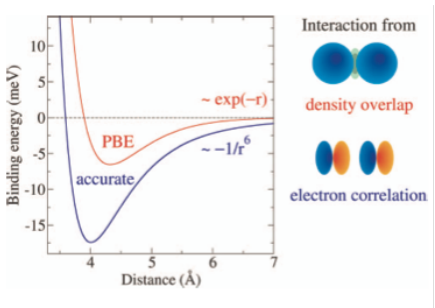

Figure 3.2 Binding curves for the Kr dimer obtained with the PBE exchange-correlation functional and an accurate potential.[14]

As a result, PBE functional would rise to much lower binding energy and higher equilibrium site, as shown in Figure 3.2.

3.3.1 DFT-D2 method of Grimme

The method named as "DFT-D" simplifies the correction by adding the dispersion energy to the total energy.

$$E_{tot} = E_{KS-DFT} - \sum \frac{C_6}{R^6} \qquad \text{Eq. 19}$$

where C_6 is referred as the van der Waals constants. However, it is hard to obtain the coefficients C_6 and this coefficient should not be a constant during calculation. Therefore, DFT-D3, [15] the Tkatcheko and Scheffler (TS) approach,[16] and the Beche-Johnson (BJ) model[17,18] modified the dispersion coefficient and let the coefficient vary by the effective volume of the atom. These empirical corrected dispersion approaches give satisfactory results, but with relatively high computational cost.[19]

By introducing semi-empirical parameters, Grimme proposed a GGA-type functional.[20] The method adapts relatively short electron correlation length scales. Meanwhile, the damped C_6R^{-6} term is introduced to describe the situation with medium to large interatomic distances. Here, the total energy is given by

$$E_{DFT-D} = E_{KS-DFT} + E_{disp} \qquad \text{Eq. 20}$$

where the $E_{KS\text{-}DFT}$ is the usual Kohn-Sham energy and E_{disp} is an empirical dispersion correction, in term of C_6R^{-6}. As the atomic ionization potentials I_P and static dipole polarizabilities α are calculated from DFT/PBE0, the C_6 coefficient is given in

$$C_6^a = 0.005 N I_P^a \alpha^a \qquad \text{Eq. 21}$$

where N has values 2, 10, 18, 36, and 54 for atoms from rows 1-5 of the periodic table.

3.3.2 vdW-DF functional

So far, there is a promising nonlocal van der Waals density functional method that is directly based on the electron density.[21] It also splits the correlation

energy into short- and long- range parts. That is the exchange-correlation energy takes the following form:

$$E_{ex} = E_x^{GGA} + E_c^{LDA} + E_c^{nl} \qquad \textbf{Eq. 22}$$

where the E_x^{GGA} is the exchange energy using revPBE generalized-gradient approximation (GGA) functional, the E_c^{LDA} is the local density approximation (LDA) for the correlation energy part, and the E_c^{nl} is the non-local energy induced by non-local electron correlation effects.[22] This last part can be represented in terms of the Fourier transform of the *S* as follows:

$$E_c^{nl} = \int_0^\infty \frac{dr}{4\pi}[1 - (\hat{q} \cdot \hat{q}')^2] S_{\vec{q},\vec{q}'} S_{\vec{q}',\vec{q}} \qquad \textbf{Eq. 23}$$

where *S* is the polarization operator and dependent on frequency ω and related to the dielectric function ε_λ via

$$S = \int_0^1 \frac{d\lambda}{\lambda}[1 - \frac{1}{\varepsilon_\lambda}] \qquad \textbf{Eq. 24}$$

where λ is the coupling constant.

The newly developed optB88-vdW functional is employed in Ref.11, where the enhancement factor is written as

$$F_x^{optB88}(s) = 1 + \frac{\mu s^2}{1+\beta s \operatorname{arcsinh}(cs)} \qquad \textbf{Eq. 25}$$

where $c = 2^{\frac{4}{3}}(3\pi^{\frac{2}{3}})$, μ=0.22, and $\beta = \frac{\mu}{1.2}$. This corrected functional improves the binding and reaches a higher accuracy than B88 functional. It yields a

mean absolute deviation (MAD) in only 10 meV, compared to 62 meV from B88.[11,12,13]

In summary, the DFT method, based on a variation of electron density, give a relatively accurate and efficient way of calculating the wavefunction of a many-body system. Kohn-Sham equation gives a much easier way to solve the Schrödinger equation. However, the unknown exchange-correlation energy must be approximated. From LDA in homogenous density to gradient GGAs, different functionals suits for different problems. For van der Waals interactions, DFT has also developed methods with or without semi-empirical parameters. All in all, DFT provides a powerful tool to predict the electronic structures and then derived properties of the solid states.

References

[1] G. Kresse, Lecture notes: Computational Material Science, University of Vienna, 2000;

[2] P. Hohenberg, and W. Kohn, *Phys. Rev.* **1964**, 136, B864;

[3] http://newton.ex.ac.uk/research/qsystems/people/jenkins/mbody/mbody3.html

[4] J. P. Perdew and A. Zunger, *Phys. Rev. B* **1981**, 23, 5048;

[5] J. P. Perdew, J. A. Chevary, S. H. Vosko, K. A. Jackson, M. R. Pederson, D. J. Singh, and C. Fiolhais, *Phys. Rev. B* **1992**, 46, 6671;

[6] J. P. Perdew, J. A. Chevary, S. H. Vosko, K. A. Jackson, M. R. Pederson, D. J. Singh, and C. Fiolhais, *Phys. Rev. B* **1993**, 48, 4978

[7] J. P. Perdew, K. Burke, and M. Ernzerhof, *Phys. Rev. Lett.* **1996**, 77, 3865;

[8] J. P. Perdew, K. Burke, and M. Ernzerhof, *Phys. Rev. Lett.* **1997**, 78, 1396;

[9] J. P. Perdew, A. Ruzsinszky, G. I. Csonka, O. A. Vydrov, G. E. Scuseria, L. A. Constantin, X. Zhou, and K. Burke, *Phys. Rev. Lett.* **2008**, 100, 136406

[10] Kieron Burke, *The ABC of DFT*, http://chem.ps.uci.edu/kieron/dft/book

[11] J. Klimeŝ, D. R. Bowler, and A. Michaelides, *J. Phys.: Condes. Matter.* **2010**, 22, 022201;

[12] J. Klimeŝ, and A. Michaelides, *J. Chem. Phys.* **2012**, 137, 120901;

[13] J. Klimeŝ, D. R. Bowler, and A. Michaelides, *Phys. Rev. B* **2011**, 83, 195131;

[14] K. T. Tang and J. P. Toennies, *J. Chem. Phys.* **2003**, 118, 4976;

[15] S. Grimme, J. Antony, S. Ehrlich, and H. Krieg, *J. Chem . Phys.* **2010**, 132, 154104;

[16] A. Tkatchenko and M. Scheffler, *Phys. Rev. Lett.* **2009**, 102, 073005;

[17] A. D. Becke and E. R. Johnson, *J. Chem. Phys.* **2007**, 127, 154108;

[18] E. R. Johnson and A. D. Becke, *J. Chem. Phys.* **2005**, 123, 024101;

[19] L. A. Burns, A. Vázquez-Mayagoitia, B. G. Sumpter, and D. C. Sherrill, *J. Phys. Chem.* **2011**, 134, 084107;

[20] S. Grimme, *J. Comp. Chem,* **2006**, 27, 1787;

[21] M. Dion, H. Rydberg. E. Shoröder, D. C. Langreth, and B. I. Lundqvist, *Phys. Rev. Lett.* **2009**, 92, 246401;

[22] Y. Zhang, and W. Yang, *Phys. Rev. Lett.* **1998**, 80, 890;

Chapter IV
Tuning Graphene Properties by Nitrogen Doping and Vacancies

4.1 Introduction

Graphene, a single layer of carbon atoms, is a rapidly rising star on the horizon of materials science and condensed-matter physics.[1] It has a remarkable high electron mobility, which can reach 15,000 $cm^2V^{-1}S^{-1}$ at room temperature.[2] Beyond that, other distinctive properties such as high opacity,[3] high thermal conductivity (~5,00 $Wm^{-1}K^{-1}$),[4] high Young's modulus (~1,100 GPa),[5] large specific surface area (theoretical value, 2,630m^2g^{-1})[6], are attracting tremendous interest for a range of potential electronic applications. However, one of the main obstacles is it possesses zero bandgap, which blocks graphene applications development in the post-silicon era. Moreover, this "magical" material has also triggered interest in other low-dimensional materials such as transition metal dichalcogenides (TMDS),[7] and hexagonal boron nitrides (h-BN).[8] These new members enrich the 2-D family and possess a range of bandgaps. However, none of them has achieved the electron mobility and high frequency as graphene. Since graphene has been discovered, a lot of effort has been put into tailoring the bandgap of this 2D material without disturbing the high electron mobility, including functionalization,[9] nanostructuring,[10,11,12,13] and substrate engineering.[14,15]

After graphene exfoliation using the scotch tape,[2] there have been many research activities aiming to produce, characterize and modify graphene-based materials. To achieve a graphene single sheet, several methods have been developed besides micromechanical exfoliation of graphite.[16] Especially, chemical vapor deposition (CVD) and epitaxial growth have been employed to grow single-layer graphene on nickel, copper, or germanium substrates.[17,18,19,20,21,22] Furthermore, by the addition of NH_3 in the gas precursor, graphene can be grown with the doping of nitrogen in order to tailor the electronic properties.[23] Previously, theoretical studies have already paid a lot of attention

on the points defects, such as mono-vacancy, di-vacancy, as well as Stone-Wall defects.[24,25,28] They have adopted 4*4 supercell with LDA functional for the defect energy predictions[24], which is clearly not sufficient to prevent the defect-defect interaction. Z. Hou, *et al*, have done a lot of works to investigate the points defects through energetically and electrical properties under PBE functional. However, the defects in their study only limited on the defects under two atoms missing. Despite numerous theoretical studies on defective graphene, the investigations either contain a large density of defects or focus on the reconstructions of the carbon vacancy.[26, 27, 28] In this chapter, the author represents a systematic study of the pure carbon vacancy and nitrogen substitution up to a 6-membered ring. Moreover, the mono-/di-vacancy with a nitrogen doping defective complex is also investigated using PBEsol functionals, which has more reliable results for solid states.[30]

4.2 Calculation details

All the equilibrium geometries and electronic structures have been performed based on ab initio density functional theory (DFT), as implemented in the VASP package.[29] The PBEsol exchange-correlation functional within the generalized gradient approximation has been used due to its good performance, especially on solid and surface simulation.[30] The author also employs PBE functional for comparison.[31] Kohn-Sham orbitals[32] are expanded in a plane wave basis set with a cut-off energy of 400 eV. The systems are relaxed until all force components are less than 0.01 eV/Å. The Brillouin zone integration is performed with $5\times5\times1$, which was proven sufficiently accurate in tests. For the band structure calculations, the sample points doubled around Dirac point. The vacuum region of the supercell perpendicular to the graphene sheet was set to 15 Å to avoid any possible interlayer interaction.

To simulate the ground state of a graphene sheet and the nitrogen doping defects, a 7×7 unit cell was employed. The 98 atoms supercell sheet is large enough to prevent defect-defect interactions. To evaluate the supercell is sufficient enough, the energy per atom of the 6 carbon ring missing configuration using different n*n supercells, which is also the largest defects in all the defects, are compared. The results are shown in Figure 4.1. Clearly, the larger the supercell is, the energy per atoms is higher. However, the trend is not linear. Even the 8*8 supercell has better results, the improvement is only 0.12%, compared to the carbon chemical potential in pristine graphene. Therefore, 7*7 supercell is large enough in our study. In order to systematically study the geometries of different sites of the carbon vacancies and nitrogen substitutions, models were built with up to 6 atoms for both vacancy and nitrogen substitutions, as illustrated in Figure 4.2 and Figure 4.3, respectively. For the sites where vacancies and substitutional defects are combined, the author has considered mono-vacancy and di-vacancies with different nitrogen substitution rate around the vacancy point, as illustrated in Figure 4.4 and Figure 4..

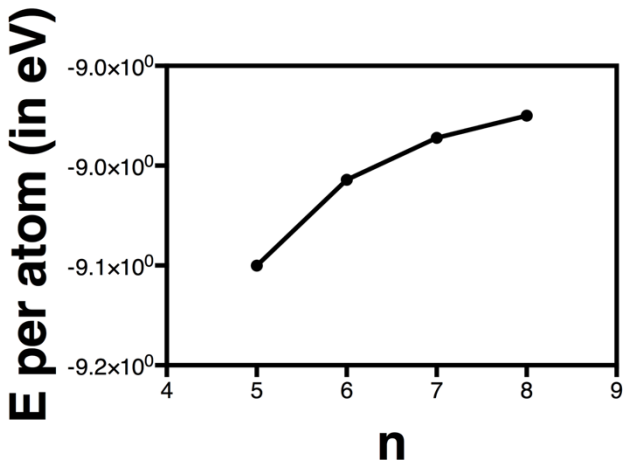

Figure 4.1 The energy per atom in the 6Vc configuration under n*n supercell.

4.3 Results and Discussion

4.3.1 Geometric structures

Before discussing the geometries of the defective graphenes, the author calculates the pristine graphene as a benchmark. Since the systems concerned contain two different coordinate types of defect, it is necessary to test in the accuracy of the model for such defective graphene. Firstly, the optimized lattice parameter for pristine graphene is 2.46 Å in PBEsol and 2.47 Å in PBE functional. Compared with the experimental (2.46 Å)[33] and other theoretical (2.465 Å)[34] data, it is clear that the reasonable choice is to follow the PBEsol functional, which has been widely recognized to improve the simulations of solid materials.[35] Meanwhile, the author also compared the results with those based on PBE functional.

To distinguish the different configurations of point defects, i.e. the vacancy defects, the substitution defects, and vacancy-substitution complexes, the following notations are used: V_C represents a carbon vacancy and N_C is for a nitrogen substitution on a carbon site. Therefore, a defective complex of n vacancies and m nitrogen substitutions are denoted as nV_C+mN_C. An extensive range of possible configurations for each defect case were calculated, and only the most stable were selected and listed in Figure 4.2-Figure 4.5.

In a graphene with only vacancy defects (Figure 4.2), the missing carbon atom(s) creates the vacancy and leaves un-terminated dangling carbon bonds around the point defects. All the vacancy defects are still planar. All the distortion and reformation is because the symmetry around the defect is

broken down with three dangling bonds around the vacancy, which induces reconstruction of the graphene, due to a Jahn-Teller like distortion. The nearby carbon atoms form a new weak bond to reduce the system total energy and new pentagon rings may form. Especially for the $5V_C$ configuration, the newly formed carbon bond length is 1.47 Å, which is comparable with the classical sp^2-sp^2 carbon bond (1.42 Å). These new conformations also stretch the bonds of the first and the second nearest neighbors. Especially, in $3V_C$ configuration, the bond length has been extended to 1.63 Å, as shown in Figure 4.2(c) with a missing bond in the second neighbor.

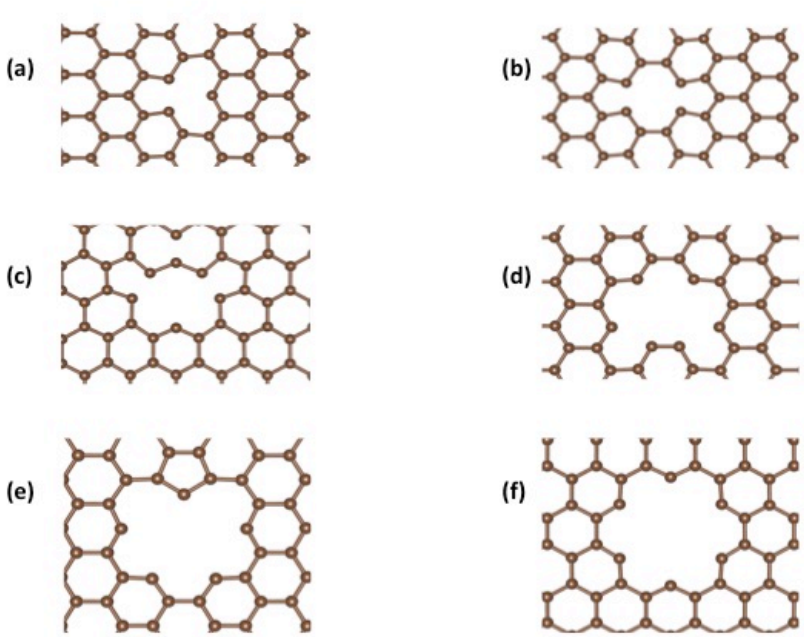

Figure 4.2 Stable configurations of nVc defective graphene, where (a) to (f), n=1-6.

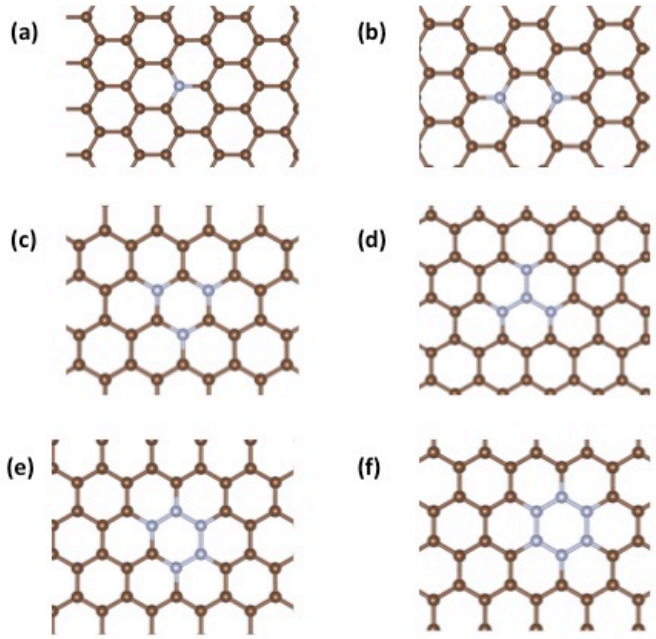

Figure 4.3 Stable configurations of nitrogen substitutional graphene, where (a) to (f) are m=1-6;

In the nitrogen substitutional graphene, the angle of the $\angle$C – N – C remains 120°, which indicates that the electronic configuration of nitrogen is of the same sp^2 type as carbon. The nitrogen-carbon bond length is 1.41 Å, which is shorter than the pristine C-C bond in graphene (1.42 Å), due to the higher electronegativity of nitrogen than carbon. For a low nitrogen substitution ratio, nitrogen atoms tend to repeal each other and form the repeated N-C bonds. The energy difference of the one with N-N bonds and the one with N-C bonds can reach 1.01 eV in the 2Nc configuration, which indicate that the C-N is more favorable than N-N even under thermodynamic conditions. However, when m ≥ 4, nitrogen atoms tend to cluster and form N-N bonding (Figure 4.3(d, e, and f)). All the configurations have been tested for thermal vibration stability. No N_2 molecules cluster out from the substitutional defective graphenes.

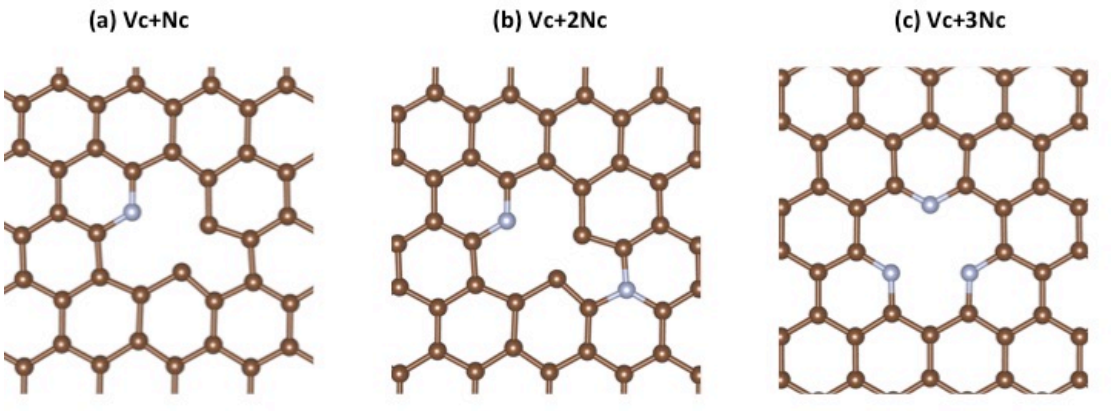

Figure 4.4 Stable configurations of defective Vc+mNc graphene complex, where m= 1-3;

Figure 4.4 shows the most stable configurations in the V_C+mN_C defective complexes. The nitrogen atoms tend to substitute the edge sites surrounding the vacancy defect. Similar to the pure nitrogen-substitution cases, at low m numbers, the nitrogen atoms tend to occupy off-site positions, i.e. forming "N-C" bonds, Figure 4.4 (b). This configuration is 0.10 eV lower than both N surrounding the vacancy configuration. This suggests the co-existence of both types of defective graphene configurations in practice. As the number of vacancies increases, the nitrogen atoms symmetrically surround the point defect (Figure 4.4 (c)).

The $2V_C$+mN_C scenario is shown in Figure 4.5. For a low substitution ratio, where m<3, there are two competing positions for the nitrogen dopants. One is away from the point defect, the other is around the point defect, shown in Figure 4.5 (a), (a'), (b) and (b'). When m=1, E_a is 1.05 eV lower than $E_{a'}$, and E_b is 0.15 eV more favorable than $E_{b'}$. While for m>2 cases, the energy difference between the favorable and the second favorite ones can reach 2 eV. Therefore, there are the two possible positions where nitrogen can occupy when the vacancy is already extant. The one is away from the vacancy, where the nitrogen shares convent bonds with carbon. The two "lone-pairs" of

electrons of nitrogen form pi-bonds with the surrounding carbon. At the same time, the carbon atoms around the point vacancy undergo the Jahn-Teller like reconstruction and new weak C-C bonds are formed to lower the total energy. The other one is to surround the vacancy, where 2 of 5 electrons of nitrogen form the N-C convent bonds. The remaining electrons disperse and hybridize in the vacancy space. The results show that nitrogen is keen to follow the first way (the former) at a low doping ratio, while the second (the latter) when at a relatively high ratio in both defective complex cases.

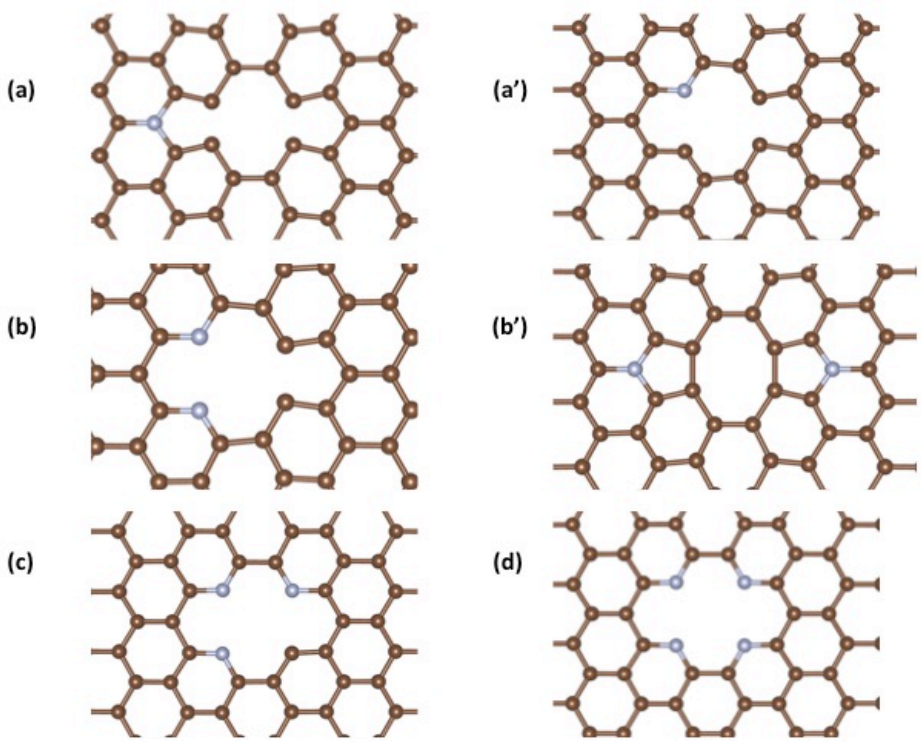

Figure 4.5 Stable configurations of the 2Vc+mNc defective graphenes, (a)-(b) represents m=1-4. The (a') and (b') are the competing configurations of (a) and (b), respectively.

4.3.2 Energetics of defective graphene systems

In order to understand further the atomic defects, the author introduces the defect formation energy, which represents the change in energy of the crystal (graphene) when an atom is removed from a regular lattice site in the bulk

and is added to the crystal surface at a typical surface site. The defect formation energy is defined as follows:

$$E_{formation} = E_{total} - (n+m)E_C - \frac{1}{2}mE_{N_2}$$

where E_{total} is the system total energy of the defective complex, and E_C and E_{N2} are the chemical energies of carbon in graphene and nitrogen in N_2, respectively. For pure vacancy- or substitutional defective graphenes, the formation energy is shown in Figure 4.6. Compared with vacancy defects, the pure substitution defects have lower formation energy in each category. The formation energy rises with the increasing number of atoms missed or substituted, especially after n or m is greater than 4, the trend rises dramatically. However, the $2V_C$ configuration possesses a lower formation energy than the V_C, which suggests that there is less energy penalty with the case of two missing carbon atoms than one. Meanwhile, it is noticeable that the defect formation energy of N_C is only 0.77 eV. This explains the high N_C doping existence defect in graphene growth.[36]

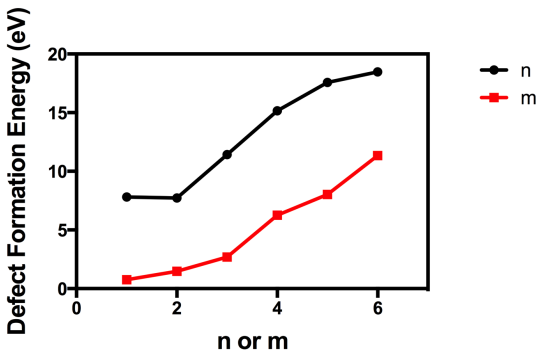

Figure 4.6 Defect formation energy of pure defective graphenes with n or m = 1-6.

For the vacancy and substitution joint complex, the formation energy is shown in Table 4.1. In each vacancy scenario, the formation energy declines as the nitrogen doping increasing until the nearest points around the vacancy point are all substituted by nitrogen atoms, where V_C+3N_C and $2V_C$+4N_C is 3.15 and 3.20 eV, respectively.

Table 4.1 Defect formation energy of the nVc+mNc defective complex.

$E_{formation}$ /eV			
V_C+N_C	V_C+2N_C	V_C+3N_C	
5.31	4.48	3.15	
2V_C+N_C	2V_C+2N_C	2V_C+3N_C	2V_C+4N_C
6.90	6.00	5.33	3.20

To further investigate the substitution progress, the author also employed a new term, the relative energy, as defined in Equation 1, where $E_{13\text{-}11}$ and $E_{13\text{-}12}$ are the "V_C+N_C" and "V_C+2N_C" defective graphene relative to "1V_C+3N_C". It also represent the relative energy of increased doping nitrogen when mono-vacancy already exists, while $E_{24\text{-}21}$, $E_{24\text{-}22}$ and $E_{24\text{-}23}$ give information on the comparison of 2V_C+4N_C with other defective complex will fewer substitute nitrogen atoms when a di-vacancy exists.

$$E_{13-11} = E_{V_C+3N_C} + 2E_{pristine} - [2E_{N_C} + E_{V_C+N_C}]$$

$$E_{13-12} = E_{V_C+3N_C} + E_{pristine} - [E_{N_C} + E_{V_C+2N_C}]$$

$$E_{24-21} = E_{2V_C+4N_C} + 3E_{pristine} - [3E_{N_C} + E_{2V_C+N_C}]$$

$$E_{24-22} = E_{2V_C+4N_C} + 2E_{pristine} - [2E_{N_C} + E_{2V_C+2N_C}]$$

$$E_{24-23} = E_{2V_C+4N_C} + E_{pristine} - [E_{N_C} + E_{2V_C+3N_C}]$$

Equation 1 The relative energy (eV) of V_C+3N_C and 2V_C+4N_C according to other doping ratio defect complex.

$$E_{13-10} = E_{V_C+3N_C} + 3E_{pristine} - [3\mathrm{E}_{N_C} + E_{V_C}]$$

$$E_{13-20} = E_{V_C+3N_C} + 3E_{pristine} - [3E_{N_C} + E_{2V_C} - E_c]$$

$$E_{24-10} = E_{2V_C+4N_C} + 4E_{pristine} - [4E_{N_C} + E_{V_C} - E_c]$$

$$E_{24-10} = E_{2V_C+4N_C} + 4E_{pristine} - \left[4E_{N_C} + E_{2V_C}\right]$$

Equation 2 The relative energy (eV) of V_C+3N_C and 2V_C+4N_C according to the pure mono-/di-vacancy or pure substitution defects

Table 4.2 The relative energy of the defective complex

	PBE	PBEsol
E_{13-11}	-3.64	-3.70
E_{13-12}	-2.22	-2.10
E_{13-10}	-6.60	-6.97
E_{13-20}	-6.65	-6.88
E_{24-21}	-6.17	-6.00
E_{24-22}	-4.14	-4.33
E_{24-23}	-2.73	-2.90
E_{24-10}	-7.11	-7.68
E_{24-20}	-7.16	-7.59

For the pure mono-/di-vacancy defects, the PBE and PBEsol functionals lead to contradictory results as the di-vacancy defect is more stable according to the PBE functional, whereas the mono-vacancy defect is energetically favored from the PBEsol functional. These results are contrary to those by Fujimoto[37], where the use of PBE functional predicts that the di-vacancy is less stable. However, the results can be confirmed by CVD graphene growth on Cu(111).[38] Therefore, the PBEsol should give more reliable results. For the nitrogen doped defective complex, the 2V_C+4N_C defective graphene complex is the most stable, compared with other defective graphenes, followed by V_C+3N_C with ~0.5 eV higher in energy. This conclusion is supported by both PBE and PBEsol functionals.

4.3.3 Electronic properties

It is well known that the existence of local defects can greatly influence the electronic properties of 2D materials.[39] Hence, the electronic properties are also investigated for both energy favorite defective complex V_C+3N_C and 2V_C+4N_C. The spin polarized projected density of state (DOS) of V_C+3N_C is shown in Figure 4.7. The Fermi level shifts towards the valence states, which suggests the defective complex is an n-type semiconductor. Meanwhile, the main contribution for the Fermi level is from the in-plane nitrogen, as well as the p_z orbital of carbon. This also explained the configuration itself, where the extra electrons of nitrogen distribute and hybridize in the spacious point vacancy to lower the energy. Further, the electron combined with the p_z orbital of the carbon atoms forms the π bond. While the π* is mainly formed by the carbon atoms.

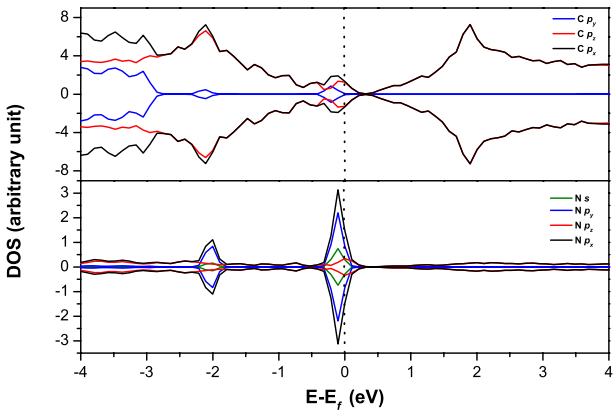

Figure 4.7 The projected density of states (DOS) of V_C+3N_C defective complex.

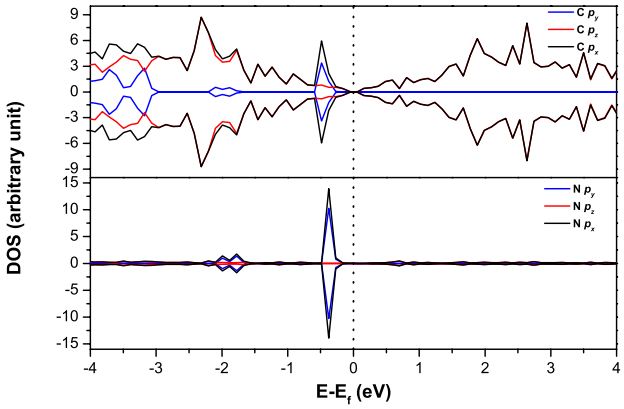

Figure 4.8 The projected density of states (DOS) of $2V_C+4N_C$ defective complex.

The spin polarized projected DOS of $2V_C+4N_C$ is shown in Figure 4.8. The valence band is contributed by the hybrid p_z orbital of carbon and nitrogen. Both carbon and nitrogen valence band are pushing downward and introduce a band gap at the Fermi level. Meanwhile, the conduction band is dominated by carbon π^* orbital and it also pushes upward and leaves a bandgap at the Fermi level. This vacancy and nitrogen doping defective complex graphene open the bandgap by 0.27 eV. Meanwhile, the band structure calculation is consistent with this conclusion, as shown in Figure 4.9. For pure graphene, with a “zero” bandgap at K point (dashed line), here opens up. However, under the periodic condition, the model itself is still porous structure with the defect ratio around 2%, which is hard to achieve in the experiments.

More accurate testing using 8*8 supercell is carried out to identify the conduction band minimum and valence band maximum. The results show the bandgap decreased to 0.265 eV. It suggests that the lower defect concentration will have a lower bandgap.

To demonstrate the charge distribution of the top valence band and bottom conduction band directly, the charge distribution at ± 0.2 eV is shown in

Figure 4.10. It shows a charge of the valence band is mainly along the y-direction while the conduction is along the x-direction. It is also in line with the results from the spin-polarized DOS. These partial charge distributions also represent the STM images at ± 0.2 V of this defective complex.

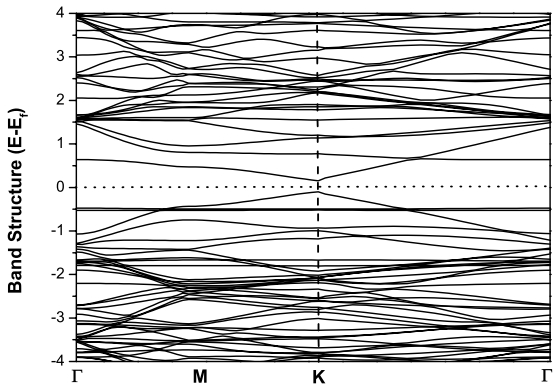

Figure 4.9 Band structure of the $2V_C$+$4N_C$ defective complex.

Notably there is a high energy dispersion in the band structure, which indicates that both electron and hole have low effective mass. To identify this, the carrier effective mass is calculated according to the following equation.

$$m^* = \hbar^2 \left(\frac{\partial^2 E}{\partial k^2} \right)^{-1}$$

where the ħ is Dirac constant, E and k are the energy and receptacle vector, respectively. The calculated effective mass is 0.089 and 0.072 for electron and hole respectively. Notably, the phonon scattering will enhance at high defect density. Therefore, the mobility will be hindered.

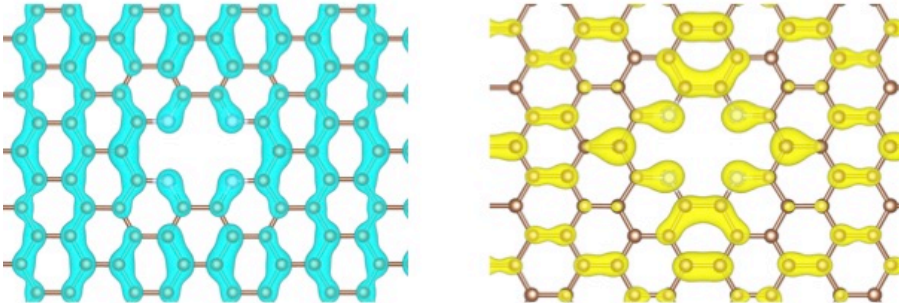

Figure 4.10 Charge distribution at ±0.2eV for$2V_C$+$4N_C$. Left graph for -0.2 eV, which indicates the top valence band, while the right one is +0.2 eV, which indicates the bottom conduction band.

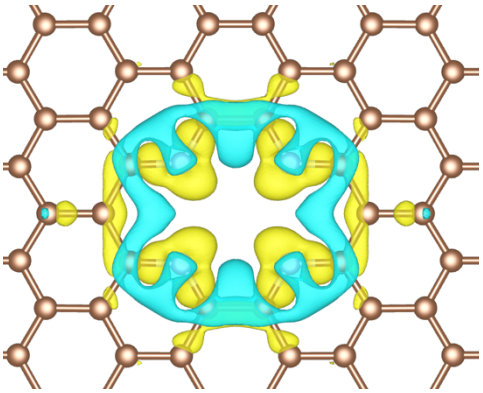

Figure 4.11 Charge distribution difference (CDD) of $2V_C$+$4N_C$, where the yellow area represents charge accumulation; while the blue area represents charge reduction.

To directly show the defect effect on the charge distribution, the charge density difference is calculated by

$$\rho = \rho_{total} - \rho_C - \rho_N$$

where ρ_{total} is the total charge density of the defective complex, and ρ_C and ρ_N are the separate charge density of carbon and nitrogen atoms, respectively. As shown in Figure 4.11, the defect merges the electron re-distribute in the vacancy area in both in-plane and out-of-plane directions, which is indicated in the figure yellow area. These all comes from the nitrogen, which has more electron negativity, and the bonded carbon nearby.

4.4 Conclusions

Here the author presents a systematic study of vacancy and nitrogen doping of graphene based on density functional theory. The results show that both supercell size and the functionals can affect the conclusion. To avoid point defect-defect effect, 7×7 supercell is the minimum to study with. The PBEsol functional gives more reliable energy. All the possible structures of the pure vacancy and nitrogen substitution have been considered. For pure vacancy defects, the carbon atoms around the point defect undergo a Jahn-Teller like distortion. When at a low doping ratio, nitrogen atoms avoid doping together, while the situation reverses at a high doping ratio. This doping behavior happens whenever nitrogen is present in both pure substitutions and is combined with substitution complex. Moreover, the vacancy and nitrogen substitution complex can tune the electronic properties, leading to change from semi-metal into n-type semiconductor. More important, it would affect the band gap, especially for energetic favorite $2V_C+4N_C$ complex. The bandgap of this defective graphene can open up to 0.27 eV, which is in a desirable range for graphene electronic applications. However, this bandgap opening only can be realized in high defect density. The calculated effective masses are 0.089 and 0.072 for electron and hole, respectively. These indicate that this bandgap opened up defective complex still retains the low effective masses.

References

[1] A.K. Geim, and K.S. Novoselov, *Nature Materials,* **2007**, 6, 183;

[2] K. S. Novoselov, A.K. Geim, S.V. Morozov, D. Jiang, Y. Zhang. S.V. Dubonos, I.V. Grigorieva, and A.A. Firsov, *Science*, **2014**, 306, 666;

[3] A.B. Kuzmenko, E. Van Heumen, F. Carone, D. Van Der Marel, *Phys. Rev. Lett.* **2008**, 100(11), 117401;

[4] X. Xu, L.F.C. Pereira, Y. Wang, J. Wu, K. Zhang, X. Zhao, S. Bae, C.T. Bui, R. Xie, J.T.L. Thong, B.H. Hong, K.P. Loh, D. Donadio, B. Li and B. Özylimaz, *Nature Communications*, **2014**, 5, 3689;

[5] C. Lee, X. Wei, J.W. Kysar, J. Hone, *Science,* **2008**, 321, 385;

[6] M.D. Stoller, S. Park, Y. Zhu, J. An, and R.S. Ruoff, *Nano Lett.*, **2008**, 8, 3498;

[7] Q.H. Wang, K. Kalantar-Zadeh, A. Kis, J.N. Coleman and M.S. Strano, *Nature Nanotechnology,* **2012**, 7, 699;

[8] K. Watanabe, T. Taniguchi and H. Kanda, *Nature Materials,* **2004**, 3, 404;

[9] H. Wang, Q. Wang, Y. Cheng, K. Li, Y. Yao, Q. Zhang, C. Dong, P. Wang, U. Schwingenschlögl, W. Yang, X. X. Zhang, *Nano Lett.* **2012**, *12*, 141-144;

[10] J. Cai, P. Ruffieux, R. Jaafar, M. Bieri, T. Braun, T. Blankengurg, M. Muoth, A.P. Seitsonen, M Saleh, X. Feng, K. Müllen, and R. Fasel, *Nature* **2010**, *466*, 470-473;

[11] N. Mohanty, D. Moore, Z. Xu, T.S. Sreeprasad, A. Nagarja, A.A. Rodriguez and V. Berry, *Nature. Comm.* **2012**, *3*, 844;

[12] V. Barone, O. Hod, and G.E. Scuseria, *Nano Lett.* **2006**, *6*, 2748-2754;

[13] X. Wang, Y. Ouyang, X. Li, H. Wang, J. Guo, and H. Dai, *Phys. Rev. Lett.* **2008**, *100*, 206803;

[14] J.-K. Lee, S. Yamazaki, H. Yun, J. Park, G.P. Kennedy, G.-T. Kim, O. Pietzsch, R. Wiesendanger S.W. Lee, S. Hong, U. Dettlaff-Weglikowska, and S. Roth, *Nano Lett.* **2013**, *13*, 3494-3500;

[15] F. Zhao, T.T. Nguyen, M. Golsharifi, S. Amakubo, K.P. Loh, and R.B. Jackman, *J. Appl. Phys.* **2013**, *114*, 053709;

[16] K.S. Novoselov, A.K. Geim, S.V. Morozov, D. Jiang, Y. Zhang, S.V. Dubonos, I.V. Grigorieva, and A. A. Firsov, *Science*, **2004**, 306, 666;

[17] Q.K. Yu, J. Lian, S. Siriponglert, H. Li, Y.P. Chen, and S.S. Pei, *Apply Physics Letter*, **2008**, 93, 113103;

[18] L.G. De Arco, Y. Zhang, A. Kumar, and C. Zhou, *IEEE Trans. Nanotechnology*, **2009**, 8, 135;

[19] A. Reina, X. Jia, J. Ho, D. Nezich, H. Son, V. Bulovic, M.S. Dresselhaus, and J. Kong, *Nano Letter*, **2009**, 9, 30;

[20] K.S. Kim, Y. Zhao, H. Jang, S.Y. Lee, J.M. Kim, K.S. Kim, J.-H. Ahn, P. Kim, J.-Y. Choi, and B.H. Hong, *Nature*, **2009**, 457, 706;

[21] X. Li, W. Cai, J. An, S. Kim, J. Nah, D. Yang, R. Piner, A. Velamakanni, I. Jung, E. Tutuc, S.K. Banerjee, L. Colombo, and R. S. Ruoff, *Science*, **2009**, 324, 1312;

[22] G. Wang, M. Zhang, Y. Zhu, G. Ding, D. Jiang, Q. Guo, S. Liu, X. Xie, P.K. Chu, Z. Di and X. Wang, *Scientific Reports*, **2013**, 3, 2465;

[23] D. Wei, Y. Liu, Y. Wang, H. Zhang, L. Huang, and G. Yu, *Nano Lett.* **2009**, 9, 1752;

[24] Y. Fujimoto and S. Saito, *Phys. Rev. B* **2011**, 84, 245446;

[25] Z. Hou, X. Wang, T. Ikeda, K. Terakura, and M. Oshima, *Phys. Rev. B* **2012**, 85, 165439;

[26] M. Deifallah, P. F. McMillan, and F. Corà, *J. Phys. Chem. C* **2008**, 112, 5447;

[27] M. Calandra and F. Mauri, *Phys. Rev. B* **2007**, 76, 161406 (R);

[28] Z. Hou, X. Wang T. Ikeda, K. Terakura, M. Oshima, and M. Kakimoto, *Phys. Rev. B*, **2013**, 87, 165401;

[29] G. Kresse and J. Hafner. *Phys. Rev. B*, **47**:558 (1993).

[30] J.P. Perdew, A. Ruzsinszky, G.I. Csonka, O.A. Vydrov, G.E. Scuseria, L.A. Constantin, X. Zhou, K. Burke, *Phys. Rev. Lett.* **2008**, 102, 039902;

[31] J. P. Perdew, K. Burke, and M. Ernzerhof. *Phys. Rev. Lett.* **1996**, 77, 3865.

[32] P. E. Blochl. *Phys. Rev. B*, **1994**, 50, 17953;

[33] A. Das S. Pisana, B. Chakraborty, S. Picscnec, S. K. Saha, U. V. Waghmare, K. S. Novoselov, H. R. Krishnamurthy, A. K. Geim, A. C. Ferrari, and A. K. Sood, *Nature Nanotech.* **2008**, 3, 210;

[34] D. Jiang, M.-H. Du and S. Dai, *J. Chem. Phys.* **2009**, 130, 074705;

[35] X. Jiang, C. Århammer, P. Liu, J. Zhao, and R. Ahuja, *Scientific Reports*, **3, 1877;**

[36] Y. –F. Lu, S. –T. Lo, J. –C. Lin, W. Zhang, J. –Y. Lu, F. –H. Liu, C. –M. Tseng, Y. –H. Lee, C. –T. Liang, and L. –J. Li, *ACS Nano*, **2013**, 7, 6522;

[37] Y. Fujimoto and S. Saito, *Phys. Rev. B* **2011**, 84, 245446;

[38] T. Niu, M. Zhou, J. Zhang, Y. Feng, and W. Chen, *J. Am. Chem. Soc.* **2013**, 135, 8409;

[39] M. M. Ugeda, I. Brihuega, F. Hiebel, P. Mallet, J. –Y. Veuillen, J. M. Gómez-Rodriguez, and F. Ynduráin, *Phys. Rev. B* **2012**, 85, 121402(R);

Chapter V
Graphene@Diamond(111) and (100) Surfaces: Bandgap Opening by Substrate

5.1 Introduction

In this chapter, another way of tuning the graphene bandgap was studied, i.e. by a creation of a sizable bandgap without degradation of the electronic properties of graphene via. substrate hybridization. Typically, graphene-based field effect transistors (FETs) have been built on Si/SiO_2 substrates.[1,2,3] It captures graphene's superior current-carrying capacity, with the breakdown current density, J_{BR}, of ~1 μA/nm^2.[4,5] However, most of the heat accumulated at the bottom of the Si/SiO_2 wafer, due to the high thermal conductivity of graphene.[6] It has been found that the hybrids suffer from additional phonon scattering associated with the low surface phonon energy (59meV) and large trap density in the substrates.[7] This will further limit the performance of the graphene. Diamond, as the isotope of graphene, possesses the higher energy of the optical phonons (165 meV). Owing to its high thermal conductivity and low phonon scattering, diamond as a substrate may provide an alternative way of tuning the properties of graphene, such as reduction of the electrical noise, while tuning the bandgap of graphene. So far, experimentalists have fabricated FETs of graphene on diamonds, [8] diamond-like-carbon[7] or nanodiamonds[9]. However, the mechanisms of between the sp^2 and sp^3 carbon, the orientation of the diamond surfaces and the surface termination effects are still unclear. Previous theoretical studies have focused on the diamond (111) surface, due to its geographic configuration are compatible with graphene.[10] Hu, *et al.* have studied the interaction of graphene with the diamond (111) and (100) surfaces. However, the results are still highly debatable, as the supercell of the diamond (100) would fold a lot of "noise" in the primitive cell band structure using plane-wave based calculations. Here, a systematic theoretical study of the graphene interaction of diamond surface is presented. Our results show that the hydrogen termination plays an essential

role to enhance the interface interaction. Meanwhile, the diamond (100)-2x1 surface is preferable than the diamond (111) surface for such purpose.

5.2 Calculation Details

The DFT simulations were carried out using Vienna *ab-initio* Package (VASP). [11, 12] The electron-core interaction is treated using projected augmented wave (PAW) potentials.[13,14] The exchange and correlation term uses the PBE functional, which is proven good for diamond and graphene simulations.[15,16] Because the van der Waals interaction plays an essential role in the hybrid structures, this interaction is treated using the optB88-vdW.[17] This functional is proven to be more accurate on H-bonded van der Waals interaction.[18] Kohn-Sham orbitals are expanded in a plane wave basis set with a cut-off energy of 800 eV. The systems are relaxed until all forces are less than 0.01 eV/Å. A Monkhorst-Pack mesh of 7×7×1 was used for the heterostructures. The dipole correction is also considered.

5.3 Results and Discussion

Considering the lattice mismatch of the graphene and single crystal diamond surfaces, difference supercells have been chosen to minimize the strain of the heterostructures. For the D (111) surface, a 1×1 unit cell is used for matching 1×1 graphene. The mismatch is 2.2%. For the D(100) surface, a $\begin{pmatrix} 7 & 1 \\ 4 & 1 \end{pmatrix}$ supercell was employed to match a $\begin{pmatrix} 6 & 1 \\ 4 & 1 \end{pmatrix}$ graphene, with a mismatch 1.2%. To investigate the effect of the hydrogen treatment (termination) of the diamond surfaces, both bare and hydrogen terminated single-crystal diamond (SCD) (111) and (100) surfaces were considered. The supercells of Gr@H_D(111) and Gr@H_D(100) are shown in Figure 5.1 (a) and Figure 5.2 (a). All the SCD models consist of 6 layers of carbon atoms with the bottom

carbon terminated by H atoms. During the relaxation, only the bottom 3 layers, as well as the bottom H atoms, were kept fixed in respective of bulk positions, with all other atoms fully relaxed until the force on any given atom is smaller than 0.01 eV/Å. The side view of Gr@H_SCD (111) and Gr@H_SCD(100) are shown in Figure 5.1(b) and Figure 5.2 (b), respectively, where the SCD(100) undergoes a 2×1 reconstruction. The binding energy (E_b) per atom of graphene with the substrate is defined as follows:

$$E_b = \frac{1}{N_G}[E_{Gr@D} - (E_{Gr} + E_D)]$$

where $E_{Gr@D}$ is the total energy of the graphene-on-diamond heterostructure; E_{Gr} and E_D are the energies of the isolate graphene and the diamond substrates, respectively; and N_G is the number of graphene atoms in the supercell.

The distance and the binding energy between the graphene and the diamond surface at the equilibrium position are listed in Table 5.1. Overall, the distances are closer in the hydrogen terminated SCDs than the bare SCDs. This is due to the hydrogen treated surface bringing about a stronger interaction between the two components of the heterostructures. Moreover, the Gr@H_SCD(100) shows the closest distance between the graphene and the diamond surface. These results are also consistent with the variation of the binding energy. Notably, in both Gr@H_SCD(100) and Gr@SCD(100) cases, the binding energies are in the same range as graphite, ~65 meV.[19] While in the Gr@H_SCD(111) and Gr@SCD(111) cases, the binding energy is halved. This indicates that the surface orientation of diamond will affect the interactions of the two components in the heterostructure.

Table 5.1 Binding energy per graphene atoms E_b (meV) and the distances between graphene and substrates (A) at equilibrium states

Samples	E_b (meV)	Distance (A)
Gr@H_SCD(100)	-59	2.68
Gr@H_SCD(111)	-35	2.77
Gr@SCD(100)	-56	3.83
Gr@SCD(111)	-20	3.13

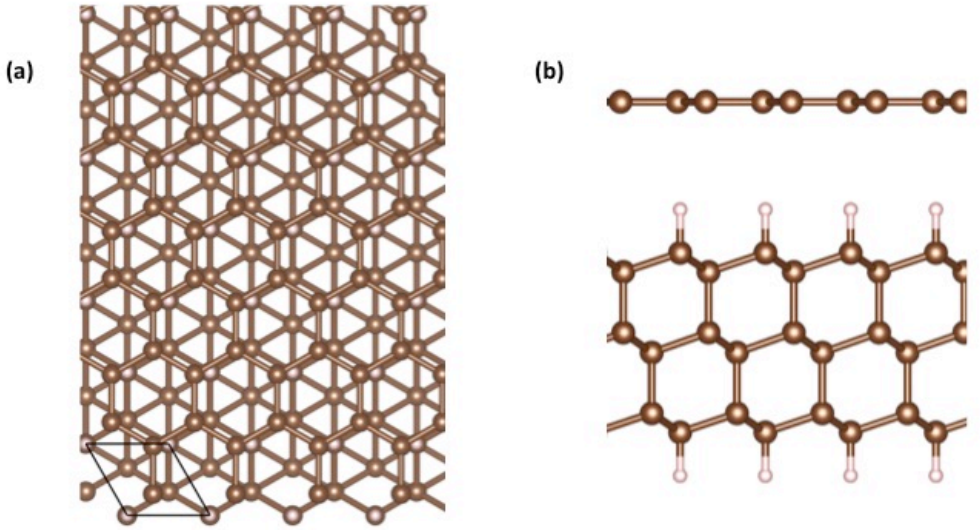

Figure 5.1 Equilibrium structure of graphene @H_SCD(111). (a) top view; (b) side view. The primitive cell is shown in the solid line in (a). The brown balls represent carbon and the pink ones are hydrogen

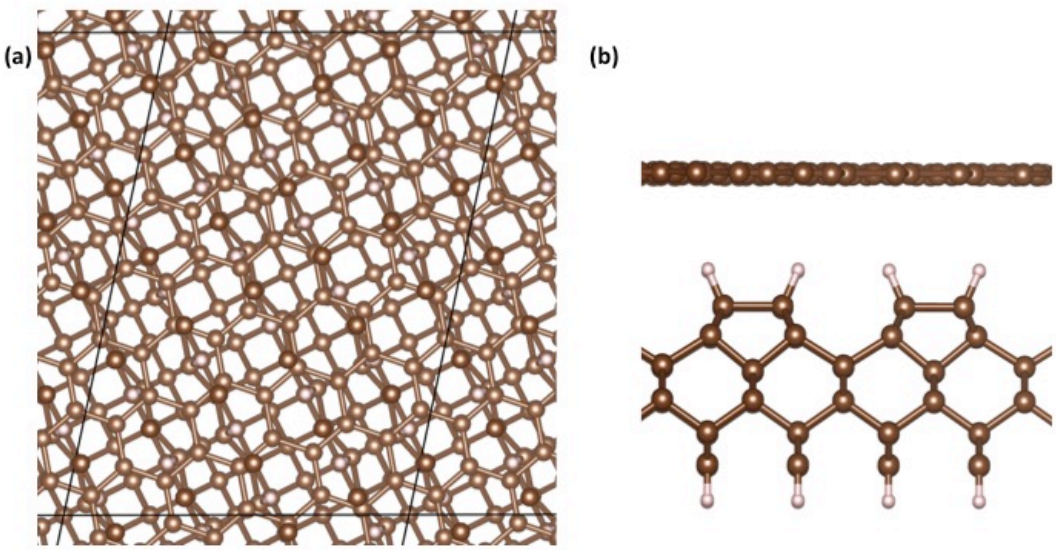

Figure 5.2 Equilibrium structure of graphene @H_SCD(100). (a) top view; (b) side view. The primitive cell is shown in the solid line in (a). The brown balls represent carbon and the pink ones are hydrogen

Because of the asymmetric interface of graphene and the substrate, the charge will redistribute between the two. Detailed electronic properties are

also investigated by charge density difference and band structure. The charge density difference is defined as

$$\rho = \rho_{Gr@D} - (\rho_{Gr} + \rho_D)$$

where $\rho_{Gr@D}$ is the charge density of the Gr@Diamond heterostructure and ρ_{Gr} and ρ_D is the isolated graphene and diamond, respectively.

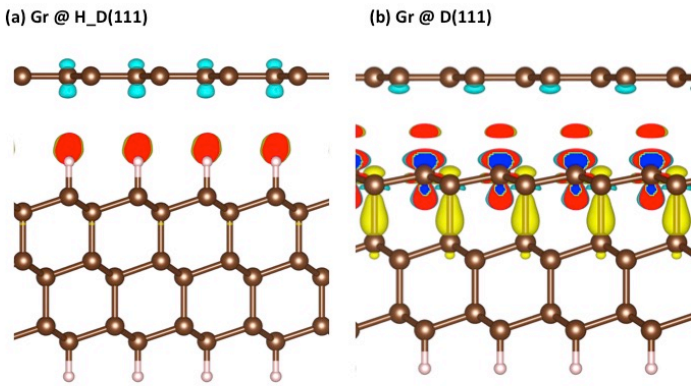

Figure 5.3 Charge density difference between graphene and H_SCD(111) / SCD(111) substrate. Blue represents the diminished of electron density while the red part represents where the electron density accumulated.

From Figure 5.3, the charge density of graphene is reduced, which is mainly due to the p_z orbital of graphene forming the π bond above the graphene. For the hydrogen-terminated surface, the charge transfer mainly consists of the charge from the graphene to the hydrogen above the diamond surface. While for the untreated diamond surface, the charge redistribution also involves the top few layers of diamond, partly due to the untreated SCD(111) surface possessing dangling bonds, which make the surface highly active.

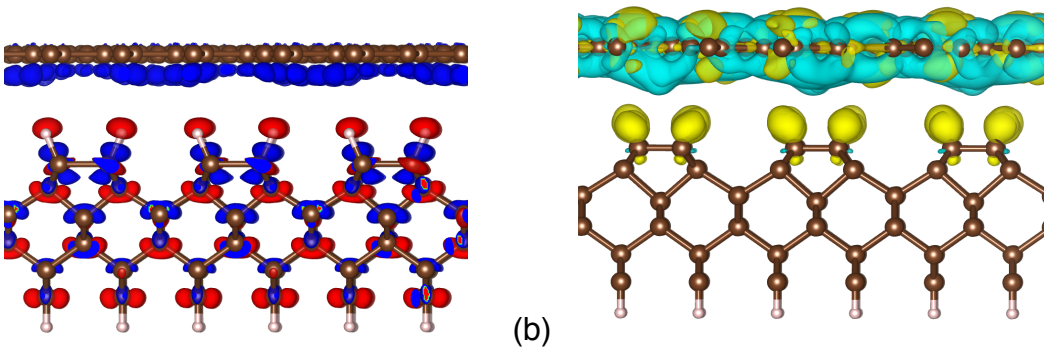

Figure 5.4 Charge density difference between graphene and H_SCD(100) / SCD(100) substrate. Blue represents the diminished of electron density, while the red part represents where the electron density accumulated. (isosurface= 0.0005 e/a_0^3)

Both the H_SCD(100) and SCD(100) substrates undergo a dimer reconstruction before the graphene is introduced (Figure 5.2 (b)). These reconstructions make a new π bond above the surface. The charge density differences of Gr@H_D(100) and Gr@D(100) are shown in Figure 5.4 (a) and (b), respectively. For the bare SCD(100) surface, the charge transfer is only within the diamond dimer and graphene itself. The graphene in Gr@SCD(100) exhibits strong tendency for hole doping. For the H_SCD(100) surface, the electrons in p_z orbitals are injected to the H on top of the substrate. It can be concluded that hydrogen treatment of the surface can induce a transfer of electrons, which consist of π state of graphene, to diamond and creates p-doping of graphene.

For the two different types of materials, the band alignment is determined by their respective work functions. Therefore, the control over graphene work function is the key to reducing the contact barrier of top electrode devices.[20,21] Previous scanning based studies reveal that the work function of graphene is similar to graphite, around 4.5 eV.[22] It also exhibits layer dependency.[23] For substrate itself, the hydrogen treatment can tune the diamond surface electron affinity from positive to negative. Therefore, the electron on the conduction band can easily escape the surface after the hydrogen treatment.[24] For the SCD(111) substrate, the vacuum level is 0.38 eV above

the conduction band, while it is 1.65 eV below the conduction band after the hydrogen treatment.[25] For the hydrogen treatment also tuned the SCD(100) surface into a negative electron affinity surface, where the vacuum level of H_SCD(100) surface lies 2.2 eV below the conduction band edge. However, the vacuum level of the untreated SCD(100) surface is 0.8 eV below the conduction band edge.[26] For the heterostructures in our system, the work functions are also investigated and listed in Table 5.2 where $\chi = E_{vacuum} - E_{fermi}$. Compared with free-standing graphene, the hydrogen treatment of the SCD can shift the work-function upward, while the untreated SCD pushes it downward (Table 5.2). These changes are due to the Fermi level shift, and the substrate induced doping.

Table 5.2 Work functions of the heterostructures, compared with the free-standing graphene.

	Gr@SCD(111)	Gr@H_SCD(111)	Gr@SCD(100)	Gr@H_SCD(100)
χ	3.67	4.83	4.02	4.92
Fermi Level	1.21	0.49	-0.39	0.07
χ of Graphene	4.8 (our result)/ 4.5(experimental)[27]			

These weakly stacked heterostructures have also tuned the band structure at K point, where the Dirac point of graphene is located, as shown in Figure 5.5 and Figure 5.5To precisely predict the band location of the Dirac point of graphene, one extra set of points have been added, when sampling near the special point. The results show that the bandgaps of the Gr@H_SCD(100) and the Gr@H_SCD(111) are 61 and 20 meV, respectively. Both band structures exhibit p-type doping characteristics. In the mean time, the energy dispersion retained in both systems, suggesting that the graphene still possesses high carrier mobility. Notably, the bandgap in Gr@H_SCD(111) is

less than 25 meV in thermal energy, indicating this bandgap opening will disappear at room temperature.

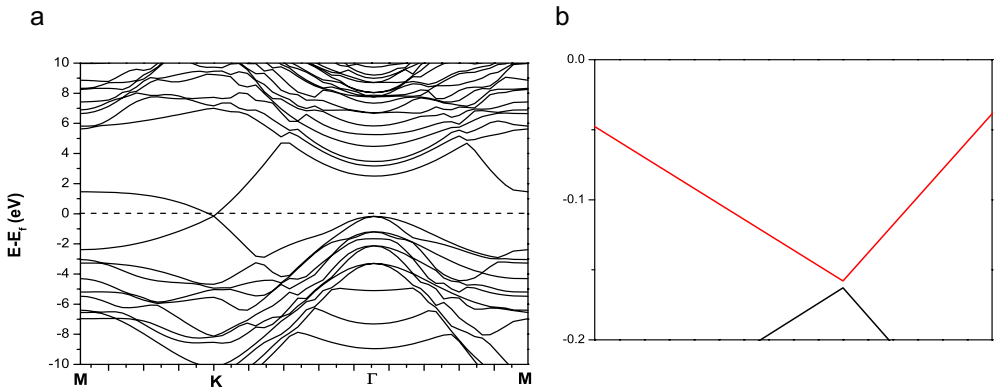

Figure 5.5 (a) Band structure of Gr@H_SCD(111) heterostrurcture along M-K-Γ-M direction. Energy is adjusted according to Fermi level. (b) Zoom-in figure at the Dirac point in (a)

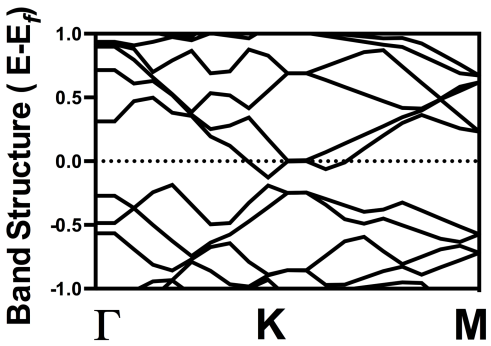

Figure 5.6 Band Structure of Gr@H_SCD(100) heterostrurcture along Γ-K-M direction. Energy is adjusted according to Fermi level.

Our theoretical results are also compared with experimental data from collaborators, as shown in Figure 5.7 and Figure 5.8. Low-temperature sheet resistance measurement was applied in a pulse tube cooler allowing cooling from room temperature to 2K by a chopped D.C. resistance technique.[28,29] Both show the resistance increases with decreasing temperature $d\rho/dT<0$, which proves a transition for graphene from a semi-metallic to semiconducting behaviour. An estimate for E_g can be deduced from the temperature dependence of the conductivity $\sigma=1/\rho$, which for a semiconducting material varies according to the Boltzmann transport model:

$$\sigma = \sigma_0 \cdot \exp\left(-\frac{E_g}{2kT}\right)$$

The ρ(T) results were plotted in Figure 5.7 by ln(1/ρ) vs 1/T to demonstrate a straight line with a slope of $-E_g/2k$.[30] For Gr@H_SCD100, the resistance increases steadily with decreasing temperature between 290 to 230K (Region 1), and from 230 to 50K (Region 2) a continuing increase in resistance with falling temperature but at a slower rate than at a higher temperature. This temperature dependence is still unclear. It could be the coverage of H is deceased as the temperature goes up. From Figure 5.7(a), the bandgap for Region 1 is 0.466eV, and the bandgap for Region 2 is 0.0286eV. However, the Gr@H_SCD(111) shows a steady increase in resistance with reducing temperature. The bandgap for G@H_SCD(111) is 0.0164eV, Figure 5.7(b).

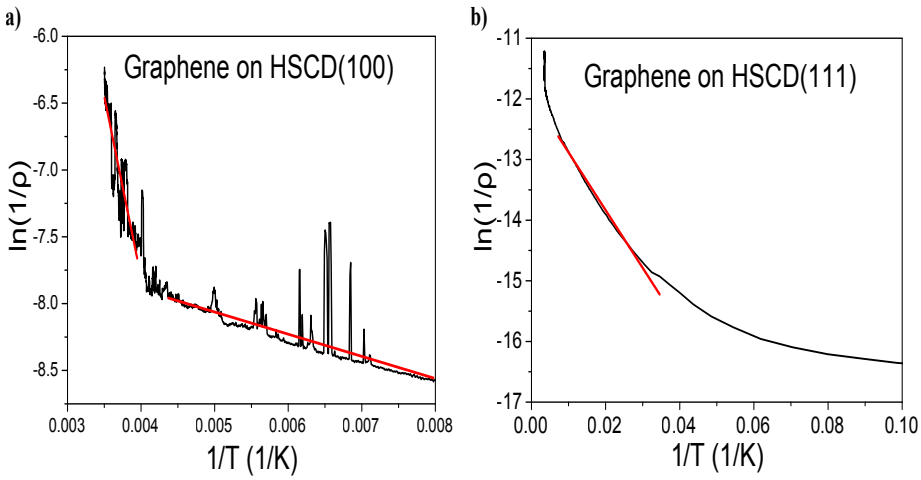

Figure 5.7 Graphic depiction of ln(1/ρ) vs 1/T. (a) Gr@H_SCD(100). (b) Gr@H_SCD(111).

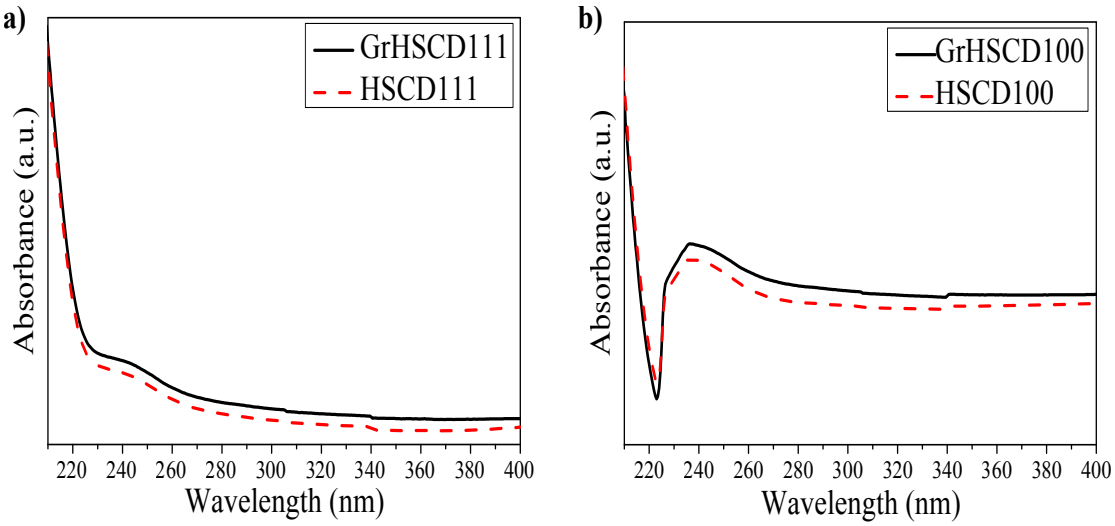

Figure 5.8 UV-Vis absorption spectra. (a) H_SCD111 and Gr@H_SCD111. (b) H_SCD(100) and Gr@H_SCD(111)

The other approach to characterize the bandgap is by the UV-visible absorption spectra. The results were plotted in Figure 5.8 for H_SCD(100)/(111) and Gr@SCD(100)/(111), respectiveley. The bandgap estimated from the cut-off wavelength with $E_g=h\cdot C/\lambda$, where *h* is Plank's constant, *C* is the speed of light.[31] The observed absorption near 210 nm for all the samples suggests a $\pi \rightarrow \pi^*$ transition of C=C.[32] However, a small shoulder observed for H_SCD(100) and Gr@H_SCD(100) gives a second bandgap. The bandgap is measured by the difference of the substrate with and without graphene on top. The difference in the bandgaps for H_SCD(100) and Gr@H_SCD(100) is 0.026 eV for 210nm and 0.17eV for the small shoulder. While for H_SCD(111) and Gr@H_SCD(111) only an absorption at 210nm is observed, and the difference between the bandgaps of H_SCD(111) and Gr@H_SCD(111) is 0.02eV.

Our theoretical results are in line with our experimental ones with a higher prediction of the bandgap. This is due to the following reasons. Firstly, the commercial CVD graphenes used in the FETs cannot be perfect and pristine as in the modelling. Secondly, the remaining PMMA could also effect the performance of the graphenes. Thirdly, the H-treatment of the diamond

surfaces cannot reach to 100%, which is the essential factor for the bandgap opening.

5.4 Conclusions

Here we proposed an approach to tune the graphene bandgap using another carbon allotropy, diamond, as a substrate, due to diamond's high thermal conductivity and low electrical noise. The calculations have been carried out by adapting two different diamond surface orientations, SCD(100) and SCD(111), with/without hydrogen termination. These sp^2-sp^3 hybrid structures undergo charge redistribution from graphene to the substrate. Consequently, the graphene is of p type characteristics. Moreover, the hydrogen treatment of the diamond surfaces can further enhance the interlayer interaction. However, these effects vary with different surfaces orientations. The bandgap of Gr@H_SCD(100) and Gr@HSCD(111) are 61 and 20 meV, respectively. Comparing the results of low-temperature sheet resistance measurements and UV-vis data of the fabricated FET from our collaborators, these predictions provide further insight of the interaction mechanism for tuning of the bandgap of graphene.

References

[1] S. Ryu, L. Liu, S. Berciaud, Y.-J. Yu, H. Liu, P. Kim, G. W. Flynn, and L. E. Brus, *Nano Lett.* **2010**, 10(12), 4944;

[2] P. Joshi, H. E. Romero, A. T. Neal, V. K. Toutam, and S. A. Tadigadapa, *J. Phys. : Condes Matter.* **2010**, 22, 334214;

[3] Z. Cheng, Q. Zhou, C. Wang, Q. Li, C. Wang, and Y. Fang, *Nano Lett.* **2011**, 11(2), 767;

[4] A. Pirkle, J. Chan, A. Venugopal, D. Hinojos, C. W. Magnuson, S. McDonnell, L. Colombo, E. M. Vogel, R. S. Ruoff, and R. M. Wallace, *Appl. Phys. Lett.* **2011**, 99, 122108;

[5] K.-J. Lee, A. P. Chandrakasan, and J. Kong, *IEEE Electron Device Lett.* **2011**, 32, 557;

[6] M. Freitag, M. Steine, Y. Martin, V. Perebeinos, Z. Chen, J. C. Tsang and P. Avouris, *Nano Lett.* **2009**, 9(5), 1883;

[7] Y. Wu, Y.-M. Lin, A. A. Bol, K. A. Jenkins, F. Xia, D. B. Farmer, Y. Zhu, and P. Avouris, *Nature*, **472**, 74 (2001);

[8] J. Yu, G. Liu, A. V. Sumant, V. Goyal, and A. A. Balandin, *Nano Letts.* **12**, 1603 (2012);

[9] Fang Zhao, Andrei Vrajitoarea, Qi Jiang, Xiaoyu Han, Aysha Chaudhary, Joseph Welch, and Richard Jackman, *Sci. Rep.* accepted.

[10] Y. Ma, Y. Dai, M. Guo and B. Huang, *Phys. Rev. B*, **85**, 235448 (2012);

[11] G. Kresse and J. Hafner. *Phys. Rev. B,* **47**, 558 (1993);

[12] G. Kresse and J. Hafner. *Phys. Rev. B,* **49**, 14251 (1994);

[13] P.E. Blochl. *Phys. Rev. B*, **50**, 17953 (1994);

[14] G. Kresse and D. Joubert, *Phys. Rev. B*, **59**, 1758 (1999);

[15] J. P. Perdew, K. Burke, and M. Ernzerhof. *Phys. Rev. Lett.* **77**, 1396 (1997);

[16] J. P. Perdew, K. Burke, and M. Ernzerhof. *Phys. Rev. Lett.* **78**, 1396 (1997)

[17] J. Klimeš, D. R. Bowler, and A. Michaelides, *Phys. Rev. B,* **83**, 195131 (2011)

[18] J. Klimeš, and A. Michaelides, *J. Chem. Phys.* **2012**, 137, 120901;

[19] G. Graziano, J. Klimeš, F. Fernandez-Alonso, and A. Michaelides, *J. Phys.: Condens. Matter* **2012**, *24*, 424216

[20] H. Ishii, K. Sugiyama, E. Ito, K. Seki, *Adv. Mater.* **1999**, 11, 605;

[21] J. Jiang, T. D. Krauss, L. E. Brus, *J. Phys. Chem. B* **2000**, 104, 11936;

[22] G. Giovannetti, P.A. Khomyakov, G. Brocks, V. M. Karpan, J. van den Brink, and P.J. Kelly, *Phys. Rev. Let.* **2008***,* 101, 026803;

[23] H. Hibino, H. Kageshima, M. Kotsugi, F. Maeda F. –Z. Guo, and Y. Watanabe, *Phys. Rev. B* **2009**, 79, 125437;

[24] L. Diederich, O. M. Küttel, P. Aebi, L. Schlapbach, *Surface Sci.* **1998**, 418, 219;

[25] J. B. Cui, J. Ristein, and L. Ley, *Phys. Rev. Lett.* **1998**, 81, 429;

[26] J. van der Weide, Z. Zhang, P. K. Baumann, M. G. Wensell, J. Bernholc, and R. J. Nemanich, *Phys. Rev. B* **1994**, 50, 8;

[27] T. Takahashi, H. Tokailin, T. Sagawa, *Phys. Rev. B* **1985**, 32, 8317;

[28] L. Hao, J. C. Gallp, and D. Cox, *Appl. Phys. Lett.* **2009**, 95, 113501;

[29] G. Wang, Q. Jia, and G. Cao, *IEEE Symp. Electr. Electron. Eng.* **2012**, 19;

[30] S. Das Sarma, E. H. Hwang, K. Kechedzhi, and L. Tracy, *Phys. Rev. B* **2014**, 90, 125410;

[31] W. Zhang, Y. Sun, F. Dong, W. Zhang, S. Duan, and Q. Zhang, *Dalton Trans.* **2014**, 43, 12026;

[32] H. –C. Hsu, I. Shown, H. –Y. Wei, Y. –C. Chang, H. –Y. Du, Y. –G. Lin, C. –A. Tseng, C. –H. Wang, L. –C. Chen, Y. –C. Lin, and K. –H. Chen, *Nanoscale,* **2013**, 5, 262;

Chapter VI
Strain effects on phosphorene nanoribbons

6.1 Introduction

One of the most critical and challenging issues facing the electronics industry is the development of alternatives to silicon-based materials enable large improvements in device performance.[1,2,3] Considerable efforts have been devoted to 2D materials, such as graphene,[4] which despite promising charge transport properties is unable to function as a switch in transistor devices due to the lack of an intrinsic bandgap. To ameliorate this, several avenues of research have been pursued in order to increase the bandgap, including functionalization,[5] nanostructuring,[6,7,8,9] and substrate engineering.[10,11] Results to date are inconclusive and so alternative materials are sought.

The recent exfoliation of black phosphorous,[12,13] which consists of weakly stacked layers of a quasi-planar corrugated half-honeycomb structure, dubbed phosphorene, has garnered huge experimental and theoretical interest due to its relatively large and direct band gap and good charge carrier motilities,[14,15,16,17,18] Presently, several open questions remain: Is it possible to synthesize this material at industrial scales? What is the nature of the strongly anisotropic conducting behaviour, *e.g.* the drain current is strongly angular dependent.[10] What are the effects of nanostructuring on the electronic and optical properties of this material?

Particularly to resolve this last question and taking inspiration from the recent experimental work on the ballistic transportation of graphene nanoribbons,[19] the authors have investigated the structural and electronic properties of phosphorene nanoribbons (PNRs).[20,21] Realistic stable nanoribbons were considered, e.g. any bonds that are cleaved are passivated with hydrogen. It is shown that out of the three lowest energy cleavage directions, one in particular demonstrates strong quantum size effects that increase the

magnitude of the bandgap, which is related to the spatial extent of the valence band edge (VBE) and conduction band edge (CBE) states. The effects of strain on the transport properties of phosphorene were theoretically investigated by calculation of the hole and electron effective masses at the VBE and CBE, respectively. We identify that the charge transport properties, based on the analysis of the effective mass, can be modified by uniaxial straining of the nanoribbons, analogous to the findings of biaxial straining on phosphorene.[22] However, we demonstrate, for the first time, that both the size of the bandgap and the transport properties (*e.g.* electron and hole mobility) of the PNRs can be extensively modified by (uniaxial) straining, allowing the tuning of the material for several applications, such as solid state lighting, light emitting diodes, flat panel displays, and bio-labeling. Furthermore, our findings indicate that it is possible to tune the directness of the bandgap by uniaxial straining for a particular nanoribbon structure, and that the resulting direct and indirect bandgaps can degenerate at a given strain, potentially allowing segregation of electrons and/or holes of the same energy by momentum and for the valley effects to manifest.

6.2 Calculation Details

We have performed first-principles plane-wave calculations within the density functional theory (DFT) using projected augmented wave (PAW) potentials to treat the core electrons. All calculations were performed using the Vienna *ab-initio* Simulation Package (VASP). [23, 24] Several exchange-correlation functionals were used in order to evaluate our results, specifically the PBE functional,[25] the PBEsol functional,[26] and the HSE06 hybrid functional.[27] The van der Waals stacking in bulk phosphorus was treated using the DFT-D2 method of Grimme.[28] Kohn-Sham orbitals were expanded in a plane wave basis set with a cut-off energy of 400 eV. The systems are relaxed until all

forces are less than 0.01 eV/Å. A Monkhorst-Pack mesh of 8×8×1 was used for single layer phosphorene, whereas for nanoribbons the k-point mesh is 7×1×1. For these k-point meshes the error is less than 1 meV per atom. For the calculation of band structures for the phosphorene sheet we sample the following points of high symmetry: Γ, Y and X, whereas for the ribbon we simply sample 10 points along the vector in reciprocal space that corresponds to the ribbon direction in real space. The vacuum region is set to 20 Å perpendicular to the sheet, with an additional 20 Å vacuum separating the nanoribbons.

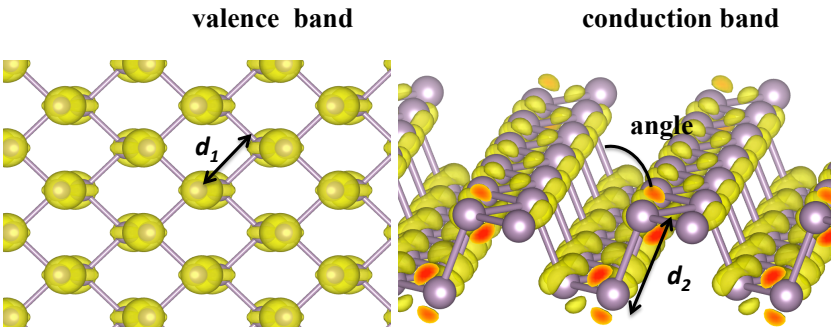

Figure 6.1 Atomic structure of phosphorene and partial electronic density of valence band edge (left) and conduction band edge (right) states (isosurface is set to 0.01 e/a_0^3).

6.3 Results and Discussion

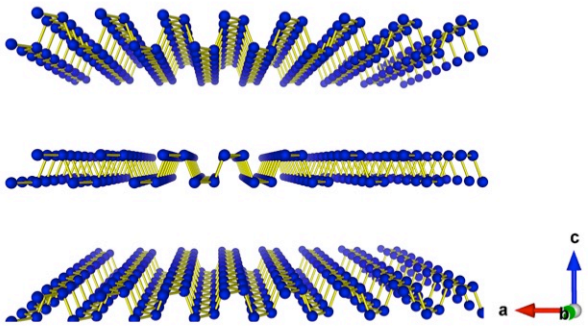

Figure 6.2 The scheme of the bulk black phosphorous.

6.3.1 Bulk black phosphorous and single layer phosphorene

The scheme of the black phosphorous is shown in Figure 6.2. Because the lack of experimental data on the single layer phosphorene, we chose the experimental data for bulk phosphorous as the benchmark to verify. In comparison of the geometry parameters, shown in Figure 6.3, PBEsol, which has improved the performance for the solid state, finds good values for *a* and *c*, even without van der Waals corrections. It strongly underestimates *b*, giving a distorted structure that does not match experiment. Furthermore, by comparing the bandgap at Γ point (Figure 6.4), it gives a bandgap that is far too large by 2.4 eV. We consider this functional is unsuitable for this material. Both PBE and HSE06 have overestimated the *b* and *c* parameters by 6.7% and 4.2%, respectively. Furthermore, these functionals either underestimate or overestimate the bandgap at Γ point. However, these errors have been highly improved by considering the weak van der Waals corrections, especially for PBE functional. Both Tran *et al.* [18] and Appalakondaiah *et al.*[29] have investigated the role of these interactions on the lattice parameters. Especially the HSE06 functional with Grimme correction, it gives the same bandgap 0.3 eV of the bulk phosphorus. Compared to reference 12, they calculated the electronic structure by manipulated HSE functional with smaller screened factor and the structure determined by PBE functional to meet the experimental data. Their bandgap was 0.37 eV smaller than the experimental one. Therefore, the key factor for bulk black phosphorous is the van der Waals correction. These give us confidence to pursue the calculation of single layer phosphorene.

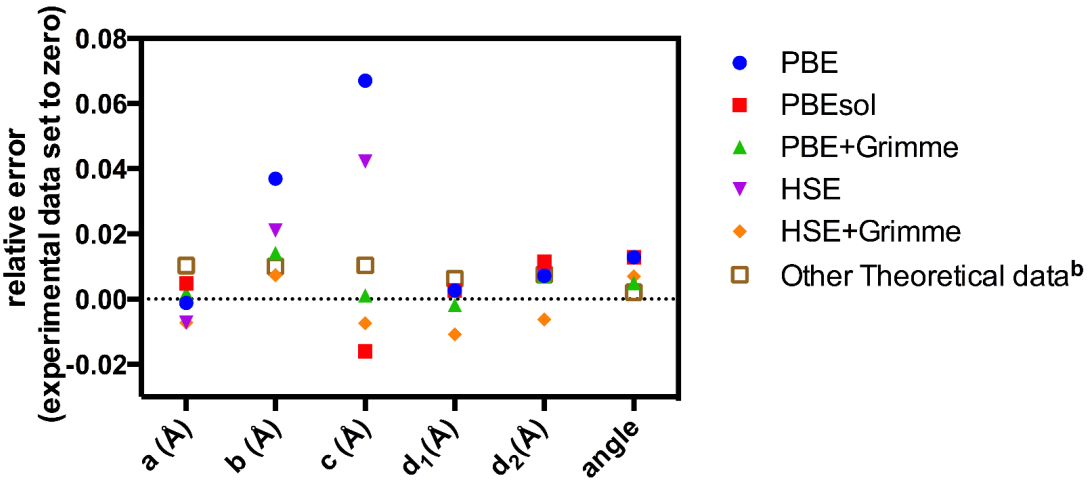

Figure 6.3 The relative error of the lattice parameters (a, b, c), bond lengths (d_1 and d_2) and the buckled angle. The experimental data is set in zero.

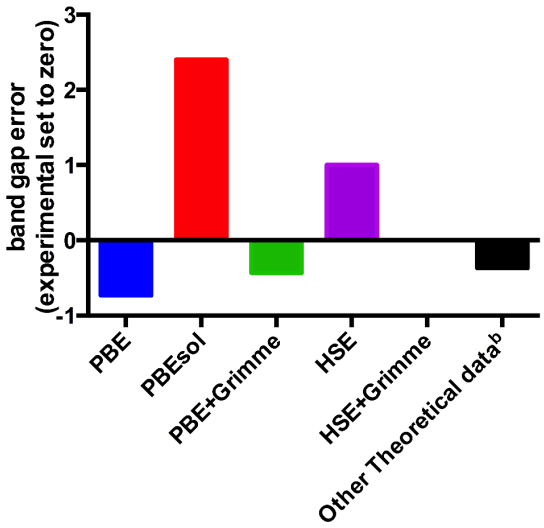

Figure 6.4 The relative error of the bandgap compare with the experimental data (in eV). b: reference 12

The geometry parameters of single layer phosphorene are listed in Table 6.1. In the absence of experimental information, we can only compare results with other simulations. As expected, van der Waals corrections are insignificant for phosphorene, with equilibrium bond lengths and band gaps nearly the same. The band gap from PBE calculations is in line with Reference 12, ~0.9eV; however, the bandgap from our hybrid functional is much higher at 1.55eV. This difference is due to two factors: the model structure in Reference12 is

from a non-hybrid PBE calculation, and their hybrid functional uses an artificially reduced exchange contribution from the default value, whereas the HSE06 has been tested to describe accurately the behaviors of many materials.[30] The influence of model structure was subsequently investigated, with the hybrid functional calculation, based on the PBE structure, yielding a bandgap of 1.30 eV.

Table 6.1 Structural parameters, bond lengths and angle, and band gap at Γ point of phosphorene

	PBE	PBEsol	PBE+vdW	HSE	HSE+vdW	Reference 12
a (A)	3.30	3.28	3.30	3.28	3.28	3.35(PBE)
b (A)	4.58	4.41	4.57	4.54	4.54	4.62 (PBE)
d_1 (A)	2.22	2.21	2.22	2.20	2.20	N/A
d_1 (A)	2.25	2.23	2.26	2.23	2.23	N/A
angle (°)	103.8	102.6	103.8	104.0	103.9	N/A
Gap {Γ(eV)}	0.90	0.70	0.86	1.55	1.55	0.90 (PBE) 1.1 (HSE)

The spatial distribution of the conduction and valence states of phosphorene are plotted in Figure 6.1. From inspection the valence band is mostly localized towards the exterior of the sheet, whereas the conduction band is more strongly weighted towards the interior of the sheet, i.e. in between the two surfaces of the sheet. This reflects the nature of the DOS, wherein both the valence band maximum (VBM) and conduction band minimum (CBM) have strong contributions from the p_z orbitals; the valence band edge state is bonding-like, and the conduction band edge state antibonding-like, see Figure 6.5.

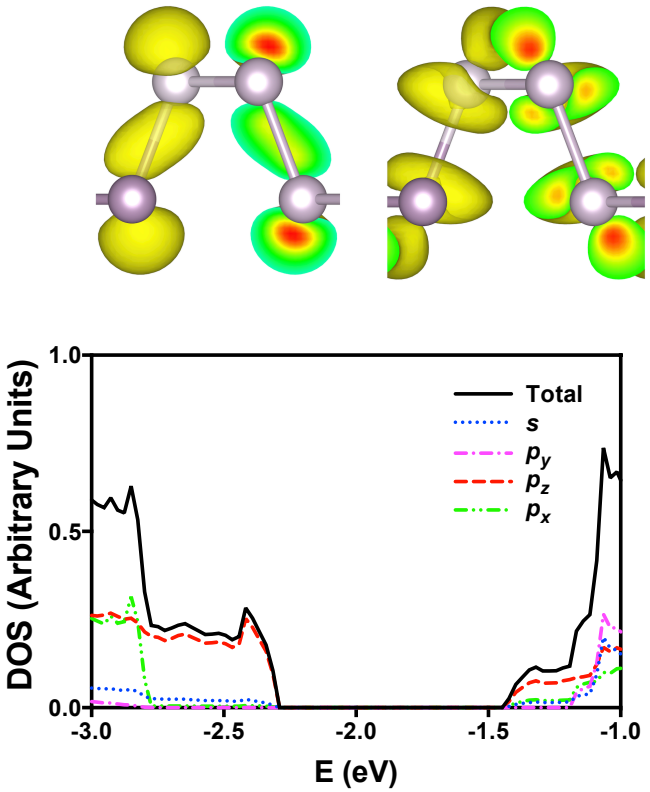

Figure 6.5 Top (left) shows side view of VBM state and top (right) shows side view of CBM state (isosurface set to 0.003 e/a_0^3). Bottom plot shows partial DOS, the zero is set to the top of the VBM, with the zero of energy set to the top of the valence band, due to the small size of Wigner-Seitz radius not all electronic density can be projected onto the atomic orbitals.

We calculated the band structure of phosphorene with the PBE functional and the HSE06 functional obtained using the relevant (PBE, HSE) crystal structure. The findings are presented in Figure 6.6. The differences between the band structures are mostly composed of a rigid shift upwards in energy of the conduction band states. Importantly, there are no major qualitative differences in the dispersion of states across the special k-points. The effective masses determined by the PBE functional are very close to those by the HSE06 functional, and thus are predictive.

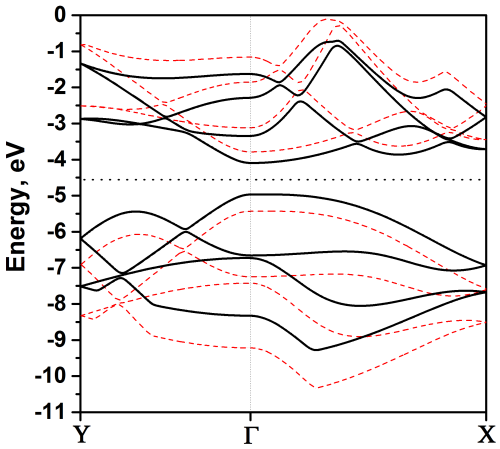

Figure 6.6 Calculated band structures of phosphorene, PBE structure with PBE functional (black solid lines), HSE06 structure with HSE06 functional (red dash lines). The zero of the y-axis is the reference level of the electrostatic potential in the middle of the vacuum region. The band structures of the two calculations were aligned using the electrostatic potential in the middle of the vacuum region.[31]

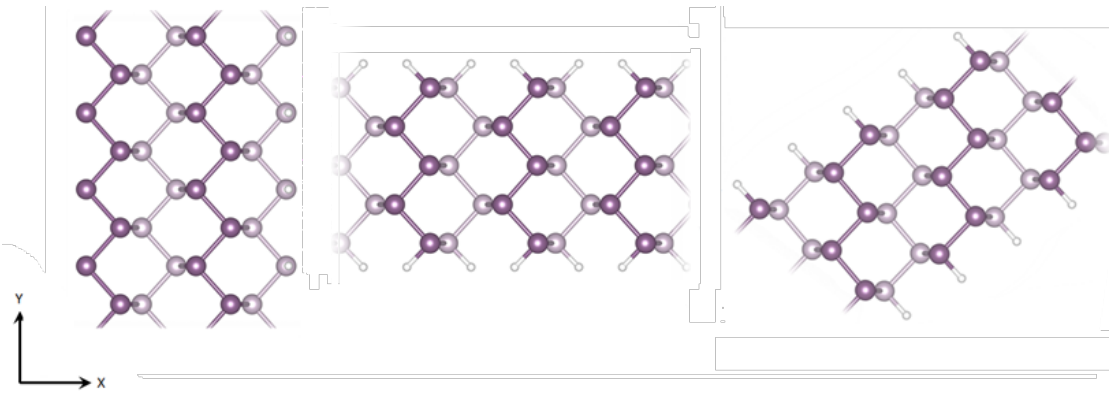

Figure 6.7 From left to right, z-PNR, a-PNR and d-PNR.

6.3.2 Nanostructuring phosphorene

From the structure of phosphorene, there are three evident orientations to form nanoribbons: the armchair ribbon (a-PNR) along [100], the zigzag ribbon (z-PNR) along [010], and a diagonal ribbon (d-PNR) along [110] (which is at an angle of 35.7° to the armchair direction), shown in Figure 6.7 The formation of each nanoribbon results in the breaking of one P–P bond per edge phosphorus atom. In realistic nanostructures, these edge atoms are highly reactive and will bond with impurities, most likely hydrogen. Therefore, in our models the edges of the ribbon are passivated with hydrogen. In order to

check for possible Peierls distortion effects that may modify the electronic structure by structural distortion,[32] we modelled several different lengths of nanoribbon, specifically ribbons of length one, two, and four unit cells. No such distortions were observed. The zero temperature edge formation energy per unit length (E_{edge}) was calculated using

$$E_{edge} = \frac{1}{2L}\left(E^{ribbon} - N_P E^{bulk} - \frac{N_H}{2} E_{H_2}\right)$$

where L is the length of the nanoribbon, E^{ribbon} is the total energy of the nanoribbon, N_P is the number of phosphorus atoms in the nanoribbon, E^{bulk} is the energy of phosphorene per atom, N_H is the number of hydrogen atoms, and $E_{H_2}$is the energy of a H_2 molecule. Our results are shown in Table 6.2. Thermodynamically these cuts are slightly exothermic for the zigzag ribbons, which are stable with respect to depassivation. However, for both the armchair and diagonal nanoribbons the formation edges are slightly endothermic. The order of stability for these nanoribbons is z-PNR > d-PNR > a-PNR. For all the systems, the narrower the ribbon, the harder it is to form. We emphasize that these formation energies refer to zero-temperature; we would expect elevated temperatures to favour hydrogen release from the edges due to the entropic factor in the Gibbs free energy. However, as black phosphorus is formed at high pressure,[33] the entropic contribution to the free energy of the gas is reduced, favouring hydrogen binding.

Table 6.2 Number of P–P rings, defined as the 6-atom unit cell as illustrated by the plane view in Figure 6.7, nanoribbon width, and formation energy of ribbon edges, for all three types of nanoribbon.

z-PNR			a-PNR			d-PNR		
Width (rings)	Width (Å)	E_{edge} (meV)	Width (rings)	Width (Å)	E_{edge} (meV)	Width (rings)	Width (Å)	E_{edge} (meV)
11	27.2	-54	9	29.8	+55	9	26.3	+2
10	25.0	-54	8	26.5	+52	8	23.5	+2
7	18.0	-51	7	23.2	+55	7	20.7	+2
6	15.8	-49	6	19.9	+53	6	17.8	+3
5	13.5	-46	5	16.5	+55	5	15.0	+4
4	11.1	-45	4	13.2	+58	4	12.2	+6
3	8.8	-43	3	9.9	+59	3	9.3	+7
2	6.7	-32	2	6.6	+62	2	6.5	+10

As shown in Figure 6.4, the magnitude of the band gap in each type of the nanoribbon increases as the ribbon's width is reduced. This effect is similar to that observed when forming graphene nanoribbons,[34] and is believed to be caused by the quantum confinement of electrons.[35]

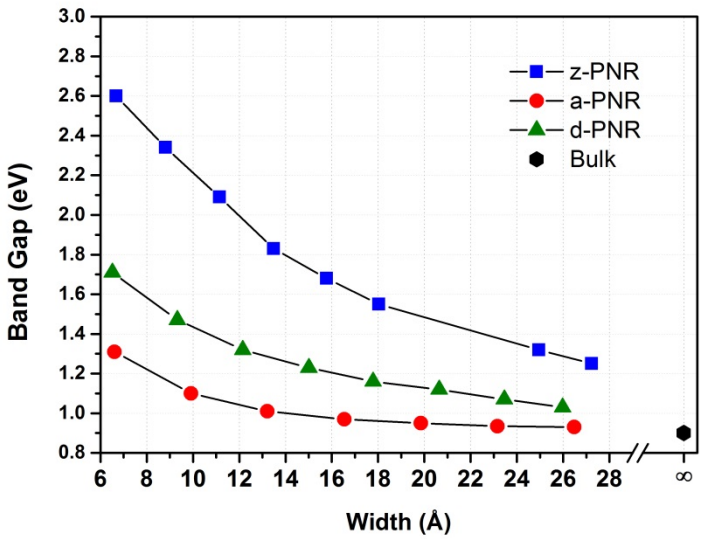

Figure 6.8 Variation of band gap with respect to nanoribbon width for z-PNR, a-PNR and d-PNR. The bulk value is also plotted as black dot.

We see that the effect of quantum confinement when cutting perpendicular to the armchair direction to form z-PNRs is considerably greater than when cutting perpendicular to the zigzag direction to form a-PNR. For example, the z-PNR of 13.5 Å wide has a band gap of 1.83 eV, while the a-PNR of 13.2 Å wide shows a band gap of only 1.01 eV (PBE phosphorene shows a bandgap of 0.90 eV). This finding is supportive of the fact that the band edge states in phosphorene propagate primarily along the armchair direction. Furthermore cutting phosphorene to form d-PNR also confines wavefunctions propagating in the armchair direction, although for a given width of ribbon the length scale of confinement is greater than when forming a-PNR and therefore the confinement effect is reduced. This change in bandgap originates from both an increase in energy of the conduction band edge, and a reduction in energy of the valence band edge. The bandgaps of the a-PNR structures and d-PNR structures are all direct, Γ →Γ; however for the z-PNR structures the lowest energy bandgap (by ~0.005 eV) is indirect, 0.0625 →Γ.

For each type of PNRs, the band gap was calculated from the HSE06 functional. We found that the HSE06 band gap was always higher than the PBE prediction. The difference of the band gaps between HSE06 and PBE calculations reduces gradually as the ribbon-width increases, varying from +0.81 eV (6.7 Å wide z-PNR), +0.68 (6.6 Å z-PNR) and +0.82 (6.5 Å d-PNR) to +0.68 eV (bulk). This is acceptable as PBE always underestimates the band gap.

The effective mass of electrons at the conduction band minimum (m_e^*) and of holes at the valence band maximum (m_h^*) were calculated using

$$m^* = \hbar^2 \left(\frac{\partial^2 E}{\partial k^2} \right)^{-1}$$

where *E* and *k* correspond to energy and the reciprocal lattice vector along the nanoribbon. These nanoribbon effective masses were compared to those of the phosphorene sheet, specifically along the equivalent directions as the nanoribbons.

For the d-PNR structures the effective masses of both hole and electrons are comparable. For 26.3 Å wide nanoribbons $m_h^* = 1.03m_0$ and $m_e^* = 0.60m_0$. Unlike the other nanoribbons, nanostructuring does not strongly modify these values, e.g. for the narrowest d-PNR, $m_h^* = 0.73m_0$ and $m_e^* = 0.68m_0$. Nanostructuring along this direction does not especially improve mobility of either type of the charge carriers.

In general, in terms of truncating the crystal lattice and maximizing charge transport (assuming there is no change in the timescale for electron scattering), a-PNR nanoribbons are best, as effective masses along this direction are smaller than in other directions, which is no doubt due to the strong p_z contributions to the VBE and the CBE. The natural direction for charge transport is through these states, and the greatest overlap between these orbitals is from one side of the sheet to the other, i.e. from top to bottom, which corresponds to the armchair direction; therefore a-PNR nanoribbons, which maintain the structure along the armchair direction, are best. The effective masses for a-PNRs compare favourably with those reported for graphene nanoribbons, which are of the order 0.06 to 0.21m_0.[36,37]

Properties of nanoribbons may be easily modified through the application of uniaxial strain. In order to investigate their response to straining, we applied uniaxial strain along the infinite direction of each type of PNR, calculated the in-plane stiffness and investigated the effects of straining on band gap and

effective mass in order to provide insight into the charge transport properties. We present results for the widest nanoribbons only, but similar trends hold for other nanoribbon widths. We investigate strains up to a magnitude of ± 10%, which is considerably less than the theoretical ultimate strain of phosphorene and thus is physically realisable.[38,39]

The in-plane stiffness, *C*, is defined in a similar manner as the conventional Young's modulus, ε^{3D}, and was calculated using:

$$C = \frac{1}{A_0}\left(\frac{\partial^2 E}{\partial \varepsilon^2}\right)$$

where *E*, ε and A_0 correspond to the energy, linear strain and equilibrium surface area of the nanoribbon;[40] while ε^{3D} has units of N/m^2 (Pa), *C* has dimensionality of N/m (Pa.m), and is related to ε^{3D} through the relationship $\epsilon^{3D} = \frac{C}{c_0}$, where c_0 is the lattice parameter perpendicular to the plane on which the 2D material lies. Our results are shown in Table 6.3. The a-PNR structures are easiest to compress, the d-PNR structures are the easiest to extend. These results are in line with recent studies on bulk phosphorene, which found that the surface tension of phosphorene under a given strain is considerably lower in the armchair direction than in the zigzag direction.[41] The values are a factor of 10 less than that reported for graphene structures.[40] This is due to the puckered structure of phosphorene, compression or extension leads to P–P–P bond angle change as opposed to C–C bond length alteration as for graphene.

Table 6.3 In-plane stiffness for a-PNR, d-PNR, and z-PNR structures upon compression and tension

Structure	***C* under compression(N/m)**	***C* under extension (N/m)**
a-PNR	22.8	18.5
d-PNR	25.2	14.0
z-PNR	96.5	48.6

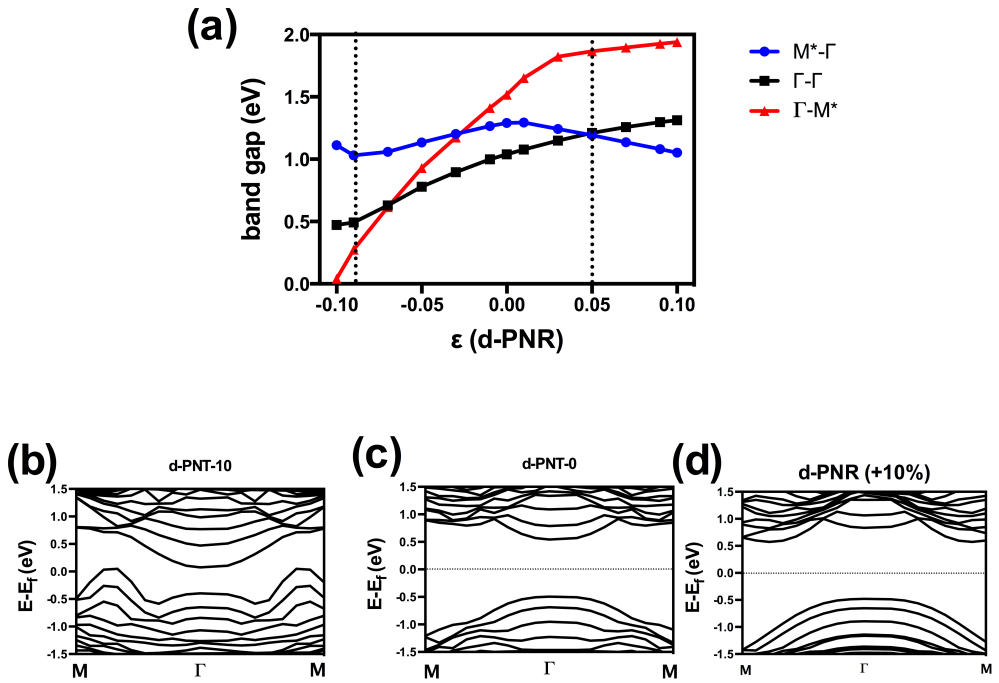

Figure 6.9 Variation of band gap with respect to strain (ε) for the d-PNR (a), both direct transition (Γ →Γ black line with squares), and two indirect transitions (Γ →M*, blue line with circles, M* →Γ, red line with triangles). The dashed lines indicate where the transition from a direct to an indirect bandgap occurs. Beneath are representative bandstructures for strains of –10% (b), 0% (c), and +10% (d), respectively.

In contrast to the a-PNR and z-PNR structures, the behavior of the bandgap with respect to external strain for the d-PNR structures is rather complicated, Figure 6.9. The direct bandgap (which involves a Γ →Γ transition) increases linearly with increasing tensile strain, and conversely decreases with increasing compressive strain. This behaviour can be understood by analysis of the band structure, as also shown in Figure 6.9. With increasing tensile strain the conduction band edge (at the Γ–point) increases in energy, leading to an increase in bandgap. The converse is true for compressive strain, where the conduction band decreases in energy (at the Γ–point). However, for critical strain parameters (+5% for tension, –7% for compression) the lowest energy transition becomes indirect. These involve transitions to or from the *k*–point M*, which corresponds to a point 0.39 reciprocal lattice vectors away from the Γ–point, and with respect to the phosphorene sheet is located at (0.2757, 0.2757, 0). Specifically, upon compression, transitions from M* to Γ

become competitive in energy, while upon extension, transitions from Γ to M^* become competitive in energy. Again, this behaviour can be related to features in the band structure. Upon compression, the valence band at point M^* increases in energy, while upon tension the conduction band at point M^* decreases in energy. For the critical value of strain (+5%) the energy of the states at the Γ–point and the M^*–point at the conduction band (for compression) or valence band (for extension) would be the same. This would have potential applications for valleytronic devices, which make use of the fact that quasiparticles with the same energy but residing in different parts of the reciprocal space have different momentums and thus are less susceptible to phonon scattering.[42]

For two-dimensional phosphorene, direct to indirect transitions are observed for external strain along the armchair direction.[41] However the same is not observed for one-dimensional a-PNR, and is only observed for the d-PNR structure. In order to explain this behaviour, it is necessary to understand the process of straining d-PNR (e.g. under tensile strain). When a-PNR or z-PNR is under strain, this strain is purely along the armchair or zigzag directions. However, when the d-PNR structure is put under tension or compression the strain is along both the armchair and zigzag directions. Furthermore, the Brillouin zone sampling of the nanoribbons is only one-dimensional, e.g. along the nanoribbon. For a-PNR and z-PNR, this means that, compared to the ideal phosphorene sheet, only *k*-points along one real space axis are projected into the reciprocal space. For strain along the armchair direction for two-dimensional phosphorene, as reported in the work of Peng *et al.*,[41] the direct-indirect transition occurs when the lowest energy conduction band state is at X (1/2,0,0) while the highest energy state is at Γ. However, for the 1-dimensional sampling of the nanoribbons, the Brillouin zone sampling can only occur at (0, Γ→1/2,0). In order to sample the lowest energy conduction

state *k*-points in two real-space axes would need to be projected into the reciprocal space, and as nanoribbons are one-dimensional systems this is forbidden. The lowest energy conduction band state cannot be accessed and the bandgaps of a-PNR remain direct. In contrast, as the d-PNR structures are diagonal, the *k*-points that are projected onto the one-dimensional reciprocal spaces are obtained from two real space axes of the corresponding phosphorene sheet, namely (Γ→0.3535, Γ→0.3535, 0). The Brillouin zone of these structures can thus sample the low-lying conduction band states that manifest under strain, and so a direct to indirect transition is observed.

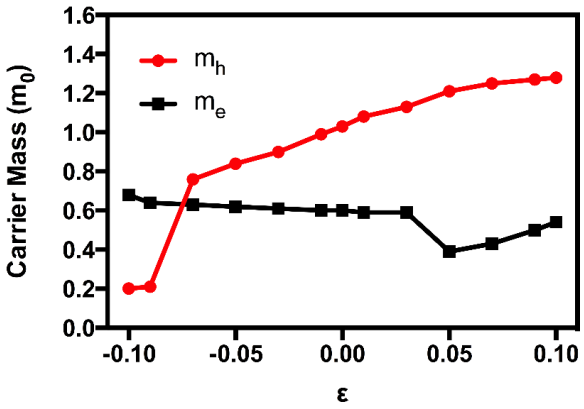

Figure 6.10 Variation of hole and electronic effective masses with respect to strain (ε) for d-PNR.

The effective masses of the electron and hole in the d-PNR were also calculated, shown in Figure 6.10. Under no external strain, the effective mass of the electron is significantly less than that of the hole, in contrast to the other two nanoribbon structures studied. When under compressive strain, the effective mass of the electron slightly increases; however, there is a significant decrease in the effective mass of the hole, especially when the bandgap undergoes a transition from direct to indirect at –9%. Initially m_h^* = $1.03m_0$, but falls to $0.20m_0$ when compressive strain is –9%. Concurrent with this, the bandgap also drops to 0.0407 eV. When the nanoribbon is under a tensile strain, hole masses slowly increase to $1.28m_0$ at strain +10%, while m_e^*

slowly decreases to $0.39m_0$ at +3% strain, before increasing again to $0.54m_0$ for a strain of +10%. This behaviour is due to the onset of the direct-indirect transition. To summarise: Compressing d-PNR improves hole effective masses, and for large compressive and tensile strains the direct to indirect transition strongly reduces the gap, which also coincides with a strong decrease in the hole effective mass. Upon tension, the electron effective mass remains smaller than the hole mass, even when the direct-indirect transition occurs at a tension of +5%.

From the above analysis of the behaviour of the effective masses given above, the d-PNR structures demonstrate an interesting direct to indirect bandgap transition for both compression and extension, which cannot only modify the optical properties, but based on analysis of the band structure we determine that at critical strains it is possible to achieve degenerate energy valleys at different *k*-points. Nanostructuring of the material in this direction would be of interest for valleytronic applications.

6.4 Conclusion

In summary, we have performed Density Functional Theory simulation of realistic passivated phosphorene nanoribbons, a one-dimensional nanostructure that demonstrates the anisotropy of the phosphorene lattice. We found that hybrid functionals do not change the dispersion of the band edges; thus gradient-corrected functionals are sufficient to calculate effective masses. We show that in order to describe correctly the electronic properties of bulk black phosphorus it is essential to include the effects of van der Waals interactions rather than artificially change the proportion of the default

exchange value. However, as we simulated quasi-two-dimensional nanostructures this correction was not needed and so was neglected.

Three types of nanoribbon were constructed and modelled, all of which involved the breaking of one P–P bond per edge phosphorus atom, the armchair, diagonal, and zigzag. All three types of nanoribbon display quantum size effects that modify the position of the valence and conduction band edges with decreasing width. In particular, the z-PNR structures show strong quantum size effects, with a large change in bandgap over the ribbon widths. For the other nanoribbons, the quantum size effect is smaller, but the bandgap of all ribbons can be tuned. Nanostructuring to very narrow widths does change the effective mass of carriers. This is structure dependent. Carrier effective mass in d-PNR structures are insensitive to nanostructuring. However, such phenomenon can be effectively utilized for electron-hole separation, e.g. in photo-catalysis.

The response of the nanoribbon structures to strain was also determined and in particular the effects of strain on the electronic structure and the effective mass were explored. For d-PNR structures, compressive strain reduces the effective mass of both the electrons and hole, while for tensile strain the electron effective mass is slowly reduced and the hole effective mass slowly increases. The *p*-type and/or *n*-type transport properties of these nanostructures can be tuned by the imposition of an external tensile strain.

The bandgap of these structures under strain has also been investigated. The behaviour of the d-PNR structures is complicated, as there are direct to indirect bandgap transitions for both compressive and tensile strain. This behaviour can be related to that of the band edges, specifically the raising of the valence band (under compression) and the lowering of the conduction

band (under tension) of the band at a special *k*-point, M^*, which is widely separated from the Γ–point; there is the possibility that d-PNR structures may be engineered upon straining so that two valleys are energetically degenerate with electrons of widely different momentum able to coexist at the same energy. These materials are thus of interest for valleytronic applications.

Phosphorene is a material that possesses great potential for electronic and optical devices. We demonstrate that electronic properties can be tuned by fabrication of nanoribbons. We show in particular that strain can improve charge transport properties, with tension potentially improving the electron transport of a-PNR structures and hole transport properties of z-PNR structures. Furthermore, the optical properties of d-PNR structures can be tuned and further experimental investigation of these structures would be of great interest.

Reference

[1] W. J. Yu, Z. Li, H. Zhou, Y. Chen, Y. Huang, and X. Duan, *Nature Mater.* **2013**, *12*, 246-252;

[2] D. H. Lee, and J. A. Gupta, *Science* **2010**, *330*, 1807-1810;

[3] S. A. Shevlin, A. Currioni, and W. Andreoni, *Phys. Rev. Lett.* **2005**, *94*, 146401;

[4] K. S. Novoselov, V. I. Fal'ko, L. Columbo, P. R. Gellert, M. G. Schwab, and K. Him, *Nature* **2012**, *490*, 192-200;

[5] H. Wang, Q. Wang, Y. Cheng, K. Li, Y. Yao, Q. Zhang, C. Dong, P. Wang, U. Schwingenschlögl, W. Yang, and X. X. Zhang, *Nano Lett.* **2012**, *12*, 141-144;

[6] J. Cai, P. Riffieux, R. Jafar, M. Bieri, T. Braun, S. Blankenburg, M. Muoth, A. P. Seitsonen, M. Saleh, X. Feng, K. Müllen, and R. Fasel, *Nature* **2010**, *466*, 470-473;

[7] N. Mohanty, D. Moore, Z. Xu, T. S. Sreepasad, A. Nagaraja, A. A. Rodriguez, and V. Berry, *Nature. Comm.* **2012**, *3*, 844;

[8] V. Barone, O. Hod, and G. Scuseria, *Nano Lett.* **2006**, *6*, 2748-2754;

[9] X. Wang, Y. Ouyang, X. Li, H. Wang, J. Guo, and H. Dai, *Phys. Rev. Lett.* **2008**, *100*, 206803;

[10] J.-K. Lee, S. Yamazaki, H. Yun, J. Park, G. P. Kennedy, G.-T. Kim, O. Pietzsch, R. Wisendanger, S. W. Lee, S. Hong, U. Dettlaff-Weglikowska, and S. Roth, *Nano Lett.* **2013**, *13*, 3494-3500;

[11] F. Zhao, T. T. Nguyen, M. Golsharifi, S. Amakubo, K. P. Loh, and R. B. Jackman, *J. Appl. Phys.* **2013**, *114*, 053709;

[12] H. Liu, A. T. Neal, Z. Zhu, D. Tománek, and D. Ye, Peide, *ACS Nano* **2014**, *8*, 4033;

[13] L. Li, Y. Yu, G. J. Ye, Q. Ge, X. Ou, H. Wu, D. Feng, X. H. Chen, and Y. Zhang, *Nature Nano,* **2014**, *9*, 372;

[14] E. S. Reich, *Nature* **2014**, *506*, 19

[15] F. Xia, H. Wang, and Y. Jia, *Nature Communications* **2014**, *5*, 4458;

[16] A. Castellanos-Gomez, L. Vicarelli, E. Prada, J. O. Island, K. L. Narasimha-Acharya, S. I. Blanter, D. J. Groenendijk, M. Buscema, G. A. Steele, J. V. Alvarez, H. W. Zandbergen, J. J. Palacios, and H. S. J. van der Santt, *2D Materials* **2014**, *1*, 025001;

[17] Z. Zhu, and D. Tománek, *Phys. Rev. Lett.* **2014** *112*, 176802;

[18] V. Tran, R. Soklasi, Y. Liang, and L. Yang, *Phys. Rev. B* **2014**, *89*, 235319;

[19] J. Baringhaus, M. Ruan, F. Edler, A. Tejeda, M. Sicot, A. Taleblbrahimi, A. Li, Z. Jiang, E. H. Conrad, C. Berger, C. Tegenkamp, and W. A. de Heer, *Nature* **2014**, *506*, 349;

[20] V. Tran, and L. Yang, *Phys. Rev. B* **2014**, *89*, 245407;

[21] X. Peng, A. Copple, and Q. Wei, *J. Appl. Phys.* **2014**, *116*, 144301;

[22] R. Fei, and L. Yang, *Nano Lett.* **2014**, *14(5)*, 2884;

[23] P. E. Blöchl, *Phys. Rev. B* **1994**, *50*, 17953;

[24] G. Kresse, and J. Hafner, *Phys. Rev. B* **1993**, *47*, 558;

[25] J. P. Perdew, K. Burke, and M. Ernzerhof. *Phys. Rev. Lett.* **1996**, *77*, 3865;

[26] J. P. Perdew, A. Ruzsinszky, G. I. Csonka, O. A. Vydrov, G. E. Scuseria, L. A. Constantin, X. Zhou, and K. Burke, *Phys. Rev. Lett.* **2008**, *100*, 136406;

[27] J. Heyd, G. E. Cruseria, and M. Ernzerhof, *J. Chem. Phys.* **2003**, *118*, 8207;

[28] D. Grimme, *J. Comp. Chem.* **2006**, *27*, 1787;

[29] Appalakondaiah, S.; Vaitheeswaran, G.; Lebègue, S.; Christensen, N. E.; Svane, A. *Phys. Rev. B* **2012**, *86*, 035105

[30] A. V. Krukau, O. A. Vydrov, A. F. Izmaylov, and G. E. Scuseria, *J. Chem. Phys* **2006**, *125*, 224106;

[31] A. Walsh, C. R. A. Catlow, *J. Mater. Chem.* **2010**, *20*, 10438;

[32] S. A. Shevlin, A. J. Fisher, E. Hernandez, *Phys. Rev. B* **2001**, *63*, 195306;

[33] E. N. Rissi, E. Soignard, K. A. McKiernan, C. J. Benmore, J. L. Yarger, *Sol. Stat. Comm.* **2012**, *152*, 390;

[34] J. W. Son, M. L. Cohen, G. Louie, *Phys. Rev. Lett.* **2006**, *97*, 216803;

[35] A. D. Yoffe, *Adv. In Phys.* **1993**, *42*, 173;

[36] P. Ruffiex, J. Cai, N. C. Plumb, L. Pathey, D. Prezzi, A. Feretti, E. Molinari, X. Feng, K. Müllen, C. A. Pignedoli, R. Fasel, *ACS Nano* **2012**, *6*, 6930;

[37] B. O. Tayo, arXiv:1404.2499, **2014**

[38] Q. Wei, X. Peng, *Appl. Phys. Lett.* **2014**, *104*, 251915;

[39] J.-W. Jiang, H. S. Park, *J. Phys. D: Appl. Phys.* **2014**, *47*, 385304;

[40] R. Faccio, P. A. Denis, H. Pardo, C. Goyenola, *A. W*. Mombrú*, J. Phys.: Condens. Matter* **2009***, 21,* 285304

[41] X. Peng, A. Copple, Q. Wei, *Phys. Rev. B* **2014**, *90*, 085402;

[42] H. Zeng, J. Dai, W. Yao, D. Xiao, X. Cui, *Nature Nano.* **2012**, *7*, 490;

Chapter VII
Van der Waals Heterostructures: Tunable electronic properties of phosphorene with Graphene

7.1 Introduction

Since graphene was exfoliated from graphite, one-atom thick two-dimensional (2D) materials have attracted great attention.[1] Led by graphene, other 2D materials, such as hexagonal boron nitride (hBN), transition metal dichalcogenides (TMDCs), and perovskite-type two-dimensional oxides, have also been explored.[2,3,4] Compared with the bulk states, these 2D materials exhibit intriguing physical properties and exciting prospects for a variety of applications. The band gap variation, ranged from zero (graphene) to 5.2 eV (hBN), the changes from indirect to direct bandgap and spin-valley coupling (TMDCs) open up new ways for electronic, photocatalysis, optoelectronic, spintronic, and valleytronics applications. After various developments in the last ten years, the next challenge for two-dimensional materials is to assemble them into van der Waals heterostructures - in a scientifically informed and technically controlled miner.[5] For semiconducting electronics, heterostructures have been applied to laser,[6] solar cells,[7] light-emitting diodes,[8] and field effect transistor, [9] *et al*. Nonetheless, the low dimensional van der Waals heterostructures have tunable properties because of the asymmetric arrangement of Dirac/Dirac-like cone. Yang, *et al,* epitaxially grows graphene on hBN by a plasma-assisted deposition method, which avoid the lattice orientation and interface caused by transferring graphene onto the substrate.[10] The atomic force microscopy (AFM) shows all graphene/hBN samples have the same moiré pattern, which indicates this can be categorized by van der Waals epitaxial growth. Moreover, these resembled van der Waals heterostructures also reveal new properties, such as higher carrier mobility,[11] reduced Fermi velocity,[12] and ballistic transport.[13] Britnell *et al.* investigate the TMDCS/graphene hybrids.[14] This ultrathin heterostructure shows improved photon absorption and photon-current production. Theoretically, Kang *et al*, have investigated MoS_2/$MoSe_2$ heterostructures,

and revealed a strong localized valence band maximum (VBM) and delocalized conduction band minimum (CBM); this hybrid also has an indirect bandgap like other bilayer TMDCs.[15]

Phosphorene, the single layer black phosphorus, is following a similar pathway as graphene from graphite. After being exfoliated using scotch tape,[16,17] few-layer phosphorenes with a puckered structure has garnered huge interest because of its intrinsic bandgap, which has been a major obstacle for graphene in electronic applications. Moreover, phosphorene shows a charge-carrier mobility of 1000 $cm^2V^{-1}s^{-1}$,[16] a highly layer-dependent bandgap,[18] an anisotropic conducting behaviour,[19] and tunable electron/hole effective mass under straining,[20] all of which make this promising 2D material highly desirable for novel applications. However, single-layer phosphorene is hard to be stabilized in the air, similar to silicene.[21] On the other hand, graphene is relatively stable and resistant to moisture at RT. Hence, phosphorene sandwiched between graphenes could provide a practically useful structure with stability and a suitable bandgap. To explore such options, we present first-principles calculations on the structural and electronic properties of the combined graphene and mono-layer phosphorene structures in this study.

7.2 Calculation Details

All the calculations were carried out using the Vienna *ab initio* simulation package.[22,23] The interactions between the valence electrons and the cores were described by the projector augmented wave (PAW) method.[24,25] The exchange and correlation energy is described by generalized gradient approximation PBE functional.[26,27] To identify explicitly the conduction band edge, the hybrid HSE06 functional, which is a hybrid of Hartree-Fock and PBE exchange functionals at the 0.25/0.75 ratio, is also employed; further optical

properties is also assessed, based on the HSE06 functional. Since van der Waals interaction plays an essential role in the 2D heterostructures, the DFT-D2 method of Grimme was selected here, as it takes into a count of those interactions with one of the most recognized approaches.[28] Kohn-Sham orbitals are expanded in a plane wave basis set with a cut-off energy of 400 eV. All the geometry was fully relaxed until all forces are less than 0.01 eV/Å. A Monkhorst-Pack mesh of 7×7×1 was used for the heterostructures. To avoid the neighbouring cell interaction, a 25 Å vacuum interlayer is considered for periodical interactions. The dipole correction is also considered.

7.3 Results and Discussion

The calculated lattice parameters, Fermi level and the bandgap of phosphorene and graphene are shown in Tabel 7.1. As phosphorene is sensitive to the strain, the supercell is chosen to keep the phosphorene fixed.[29] Even though it has higher Young's modulus, graphene is under 1% strain in the heterostructure. Because of the valence band maximum (VBM) and conduction band minimum (CBM) are all located in high symmetry points, the band gaps are insensitive to stacking orientation. The sandwich supercells (G/P/G) are selected by rotating arbitrarily the in-plane angle to fit the phosphorene sheet (Figure 7.1), in order to reduce computational cost. Furthermore, other 2D heterostructures show that the stacking orientation shows a minor effect on the binding energy and bandgap.[30]

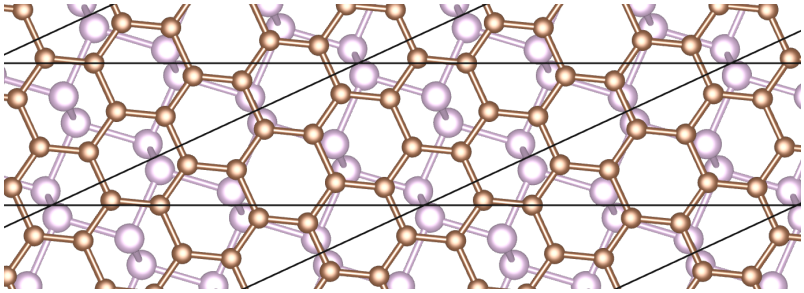

Figure 7.1 The scheme of the graphene/phosphorene/graphene (G/P/G) heterostructure. The black solid lines highlight the supercell used in the calculation.

Table 7.1 Lattice parameters of graphene and phosphorene in PBE functionals.

	a (A)	b(A)	Bandgap/eV
Graphene	2.47	N/A	0
Phosphorene	3.30	4.58	0.9

The binding energy between those two hybridized 2D materials is defined as follows:

$$E_b = \frac{1}{N_P}[E_{total} - (E_{phosphorene} + E_{graphene})]$$

where E_{total} is the total energy of the hybrid structure, $E_{phosphorene}$ and $E_{graphene}$ represent the energies of phosphorene and graphene, respectively. The number of phosphorous in the superlattice is denoted as N_P. The binding energy and the equilibrium binding distance are shown in Table 7.2. The G/P/G heterostructure exhibits van der Waals layer-layer interaction. The binding energy is -65 meV/atom, and the equilibrium distance is 3.38 Å. This binding energy is in the same magnitude of the tri-layer phosphorene (-55 meV) and graphite/h-BN (around -65 meV)[31]. Meanwhile, the results show that the interlayer distance (3.38 Å) is close to that of graphite (3.35 Å).[32] This further indicates that this heterostructure is a weak van der Waals hybrid.

Table 7.2 Binding energy and distance of GPG heterostructure at equilibrium position, as long as the Fermi level of the G/P/G in both PBE and HSE06 functionals.

	E_b (meV/P atom)	Distance (A)	Fermi level (eV)
G/P/G	-65	3.38	-0.83 (PBE) -0.91 (HSE06)

Another key feature of heterostructure is illustrated in the charge redistribution. Electrons will flow from one to the other driven by the difference in electrochemical potentials between the component materials. Here the charge density difference of the heterostructure is calculated according to Eq. 1 and plotted in Figure 7.2. Clearly, the more electronegative phosphorus atoms gain electron density, whereas the situation is reversed for carbon atoms in graphene. Furthermore, these charge redistributions mainly consist of the p_z orbitals of graphene and phosphorene as well as p_x orbitals of phosphorene. These orbitals are the dominant contributor of the conduction and valence band edges.

$$\rho = \rho_{total} - (\rho_G + \rho_P) \qquad \text{Eq. 1}$$

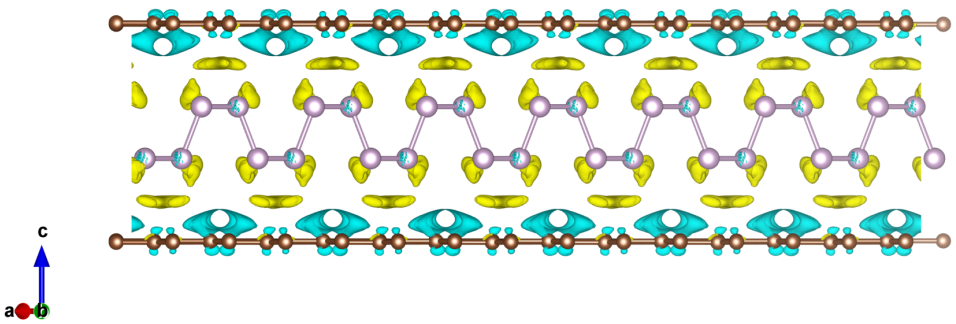

Figure 7.2 The charge density difference of G/P/G heterostructure, where the yellow area represents charge accumulation; while the blue area charge reduction.

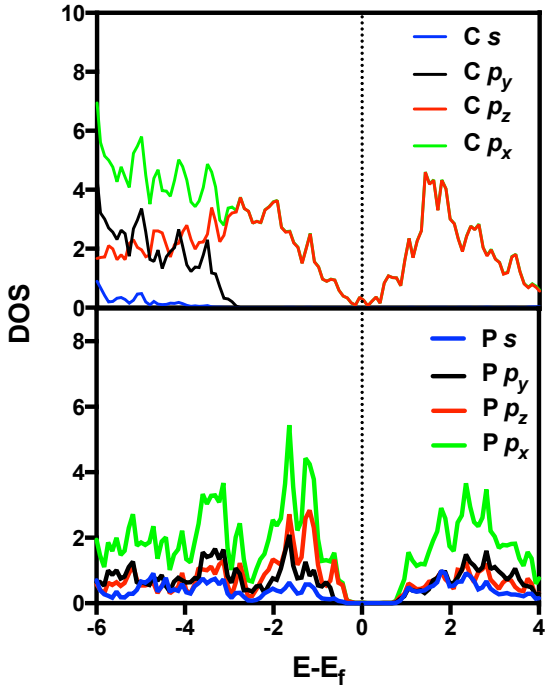

Figure 7.3 Projected density of states (DOS) of G/P/G heterostructure. Fermi level has been adjusted to zero.

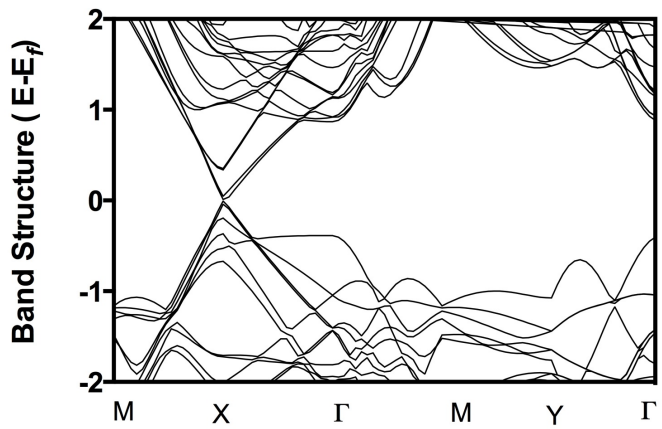

Figure 7.4 Band structure of G/P/G heterostructure in high symmetry points. Fermi level has been adjusted to zero.

The projected density of states and band structure of G/P/G are plotted in Figure 7.3 and Figure 7.4, respectively. Though the phosphorene has a bandgap at Γ point, graphene still dominates the band edges of the heterostructure. Meanwhile, the p_x and p_z orbitals of phosphorene are

hybridized with the p_z orbitals of graphene at valence band. For the conduction band, only p_z orbitals of graphene contribute to the hybridization. At the X point, where the relative superposition of the K point of graphene due to the resembling, results show a bandgap opening of 19 meV for the heterostructure. It should be pointed out that the PBE functional always underestimate the bandgap of semiconductors.[33] Hence, the band gap should be larger than this value.

Combining the desirable conductivity and transparency of graphene with the proper bandgap of phosphorene, the optical properties of this heterostructure were investigated. In order to accurate predict the optical properties, we adopted two approaches: one is to calculate static dielectric properties, based on Density functional perturbation theory (DFPT), which doesn't need to include information of the conduction bands and local field effect.[34,35] The other is the hybrid functional frequency dependent dielectric matrix calculations, which give a more accurate optical bandgap but is computationally costly.[34]

We calculate the dielectric tensor by solving the rewritten linear Sternheimer equations:

$$\big(H(k)-\epsilon_{nk}S(k)\big)|\nabla_k \breve{u}_{nk}\rangle = -\frac{\partial\big(H(k)-\epsilon_{nk}S(k)\big)}{\partial k}|\breve{u}_{nk}\rangle$$

where the $|\nabla_k \breve{u}_{nk}\rangle$ can adopt the usual expression in perturbation theory,

$$\nabla_k \breve{u}_{nk}\rangle = \sum_{n'\neq n}\frac{|\breve{u}_{nk}\rangle\left\langle \breve{u}_{nk}\left|\frac{\partial\big(H(k)-\epsilon_{nk}S(k)\big)}{\partial k}\right|\breve{u}_{nk}\right\rangle|\,\breve{u}_{nk}\rangle}{\epsilon_{nk}-\epsilon_{n'k}}$$

For the *C_1* structure in our calculation, there have six independent elements, of which ε_{11}, ε_{22} and ε_{33} represent the main dielectric constants. The average

dielectric constant is given as $\bar{\varepsilon} = \frac{1}{3}\sum_1^3 \varepsilon_{ii}$. They are listed in Table 7.3. The heterostructure exhibits birefringence behavior, whereas the ε_{22} is two orders of magnitude of ε_{33}, and 5 times of ε_{11}.

Table 7.3 Electronic dielectric tensor in three independent elements based on DFPT. The average dielectric tensor is also listed, given by $\bar{\varepsilon} = \frac{1}{3}\sum_1^3 \varepsilon_{ii}$.

ε_{11}	ε_{22}	ε_{33}	$\bar{\varepsilon}$
56.95	245.24	1.68	101.29

Conclusions

Here a sandwich stacking of graphene/phosphorene/graphene (G/P/G) heterostructure was investigated by means of Density Functional Theory simulations. The G/P/G heterostructure is a weak van der Waals stacking and the charge within is redistributed where the electron transfers from graphene to phosphorene. Consequently, graphene opened its bandgap to 19 meV, with a high degree of energy dispersion of both conduction and valence band edges. It suggests the heterostructure retained the high mobility. Meanwhile, the optical properties are also studied based on hybrid functional and DFPT theory. The dielectric constant varies dramatically with orientation, where the dielectric along the y-axis is two orders of magnitude of the z-axis.

References

[1] A. K. Geim, K. S. Novoselov, *Nature Materials* **2007**, 6, 183;

[2] K. Watanabe, T. Taniguchi, and H. Kanda, *Nature Materials* **2004**, 3, 404;

[3] Q. H. Wang, K. Kalantar-Zadeh, A. Kis, J. N. Coleman, and M. S. Strano. *Nature Nanotechnology* **2012**, 7, 669;

[4] I. Mannhart, and D. G. Schlom, *Science* **2010**, 327,1607;

[5] A. K. Geim and I. V. Grigorieva, *Nature* **2013**, 499, 419;

[6] T. Wang, H. Liu, A. Lee, F. Pozzi, and A. Seeds, *Optics Express* **2011**, 19, 11381;

[7] M. C. Sharber, D. Mühlbacher, M. Koppe, P. Denk, C. Waldauf, A. J. Heeger, and C J. Brabec, *Advanced Materials* **2006**, 18, 789;

[8] S. Chen, M. Tang, Q. Jiang, J. Wu, V. G. Dorogan, M. Benamara, Y. I. Mazur, G. J. Salamo, P. Smowton, A. Seeds, and H. Liu, *ACS Photonics* **2014**, 1, 638;

[9] F. Zhao, T. T. Nguyen, M. Golsharifi, S. Amakubo, K. P. Loh, and R. B. Jackman, *Journal Apply Physics* **2013**, 114, 053709;

[10] W. Yang, G. Chen, Z. Shi, C. C. Liu, L. Zhang, G. Xie, M. Cheng, D. Wang, R. Yang, D. Shi, K. Watanabe, T. Taniguchi, Y. Yao, Y. Zhang, and G. Zhang, *Nature Materials* **2013**, 12, 792

[11] C. R. Dean, A. F. Young, I. Meric, C. Lee, L. Wang, S. Sorgenfrei, K. Watanabe, T. Taniguchi, P. Kim, K. L. Shepard, and J. Hone, *Nature Nanotechnology* **2010**, 5, 772;

[12] M. Yankowitz, J. Xue, D. Cormode, J. D. Sanchez-Yamagishi, K. Watanabe, T. Taniguchi, P. Jarillo-Herrero, P. Jacquod and B. J. LeRoy, *Nature Physics* **2012**, 8, 382;

[13] A. S. Mayorov, R. V. Gorbachev, S. V. Morozov, L. Britnell, R. Jalil, L. A. Ponomarenko, P. Blake, K. S. Novoselov, K. Watanabe, T. Taniguchi, and A. K. Geim, *Nano Letters* **2011**, 11, 2396;

[14] L. Britnell, R. M. Ribeiro, A. Echmann, R. Jalil, B. D. Belle, A. Mishchenko, Y. J. Kim, R. V. Gorbachev, T. Georgiou, S. V. Morozov, A. N. Grigorenko, A. K. Geim, C. Casiraghi, A. H. Castro Neto, K. S. Novoselov, *Science* **2013**, 340, 1311;

[15] J. Kang, J. Li, S. S. Li, J. B. Xia, and L. W. Wang, *Nano Letters* **2013**, 13, 5485;

[16] H. Liu, A. T. Neal, Z. Zhu, Z. Luo, X. Xu, D. Tománek and P. D. Ye, *ACS Nano* **2014**, 8, 4033;

[17] L. Li, Y. Yu, G. J. Ye, Q. Ge, X. Ou, H. Wu, D. Feng, X. H. Chen and Y. Zhang, *Nature Nanotechnology* **2014**, 9, 372;

[18] V. Tran, R. Soklashi, Y. Liang, and L. Yang, *Phys. Rev. B* **2014**, 89, 235319;

[19] R. Fei and L. Yang, *Nano Letters* **2014**, 14, 2884;

[20] X. Han , H. Morgan Stewart, S. A. Shevlin, C. R. A. Catlow, and Z. X. Guo, *Nano Letters* **2014** DOI: 10.1021/nl501658d

[21] E. S. Reich, *Nature* **2014**, 506, 19;

[22] G. Kresse and J. Furthmüller, *Comput. Mat. Sci.* **1996**, *6*, 15;

[23] G. Kresse and J. Furthmüller, *Phys. Rev. B*, **1996**, *54*, 11169;

[24] P. E. Blochl, *Phys. Rev. B* **1994**, *50*, 17953;

[25] G. Kresse and D. Joubert, *Phys. Rev. B,* **1999**, *59*, 1758;

[26] J. P. Perdew, K. Burke, and M. Ernzerhof, *Phys. Rev. Lett.* **1996**, *77*, 3865;

[27] J. P. Perdew, K. Burke, and M. Ernzerhof, *Phys. Rev. Lett.* **1997**, 78, 1396;

[28] S. Grimme, *J. Comp. Chem.* **2006**, *27*, 1787;

[29] X. Han, H. Morgan Stewart, S. A. Shevlin, C. R. A. Catlow, and Z. X. Guo, *Nano Lett.* **2014**, 14(8), 4607;

[30] Y. Ma, Y. Dai, M. Guo, C. Niu and B. Huang, *Nanoscale,* **2011**, 3, 3883;

[31] G. Graziano, J. Klimeš, F. Fernandez-Alonso, and A. Michaelides, *J. Phys.: Condens. Matter* **2012**, *24*, 424216;

[32] P. Delhaès, *Graphite and Precursors,* **2001**, Gordon and Breach Science Publishers;

[33] M. K. Y. Chan and G. Ceder, *Phys. Rev. Lett.* **2010**, 105, 196403;

[34] M. Gajdoš, K. Kummer, G. Kresse, J. Furthmüller, and F. Bechstedt, *Phys. Rev. B* **2006**, 73, 045112;

[35] S. Baroni and R. Resta, *Phys. Rev. B* **1986***,* 72, 035105*;*

Chapter VIII
Functionalized Porous Graphene for H_2 purification

8.1 Introduction

As an energy carrier, hydrogen is clean and can be produced from renewable and low-carbon sources, offering a bright and promising pathway for humankind to substitute fossil fuels, particularly via. highly efficient fuel cells.[1] However, undesirable contaminants, such as carbon dioxide, carbon monoxide, methane and nitrogen, can severely degrade H_2 purity and shorten the lifetime of the fuel cell.[2,3] In order to develop effective membranes to remove or trap such impurity molecules, it is important to understand their interaction mechanisms with relative membrane materials. Here, we propose to use multi-scale simulations to study H_2 purification from gas mixtures using monolayer nanoporous graphene (NPG) membranes, featuring nitrogen-doped pores with a critical pore size. Taking kinetic diameter as the key screening factor for H_2 purification, the functionalized pores were selected, in relation to the kinetic diameters of H_2, CO_2, N_2, and CH_4, 2.89, 3.30, 3.64 and 3.80 Å, respectively.[4] Theoretically, Du et al. investigate the impact of pore sizes using a non-terminated pore model, indicating the largest selectivity for H_2/N_2 separation presents a "pore-10" geometry, i.e. 10 carbon atoms missing pore, which gradually reduces as the pore size further increases.[5] The results are in line with by the MD simulation of Sun *et al.* and empirical potential barrier calculation by Drahushuk *et al.*[6,7] Furthermore, studies show that nitrogen-functionalized pores could enhance the gas selectivity.[8,9] Here a comprehensive DFT simulation study was carried out on gas permeation mechanism, preferred direction and energy barrier across the porous membrane. The results are compared with the MD findings from collaborators. Both selectivity and permeability of H_2 can reach 35 and $4.43X10^{-21}$ $mols^{-1}Pa^{-1}$, respectively. Hence, the proposed model is perfect for H_2 purification. More importantly, the DFT results provide a clear mechanistic insight as to why the CO_2 molecule is trapped in the center of the pore, instead passing through it.

The overall study indicates that the nitrogen-doped nanoporous graphene is not only a H_2 purification membrane, and may also act as a candidate for carbon capture, especially for CO_2 at low concentrations.

8.2 Calculation details

We have performed first-principles plan-wave calculation within the density functional theory (DFT), implanted in the Vienna *ab-initio* Simulation Package (VASP). [10 , 11] The core electron interaction was treated by projected augmented wave (PAW) potentials.[12,13] Both the PBE functional[14,15] and DFT-D2 method of Grimme[16] were used for the exchange-correlation. Considering the van der Waals interaction plays an essential part when the gas molecules pass through the nanopores, all the simulations were carried out using an improved semi-empirical DFT-D2 method, unless specified otherwise, which has been proved to yield reliable results on the description of density functional dispersion correction.[17,18] Kohn-Sham orbitals were expanded in a plane wave basis set with a cut off energy of 500 eV. The sampling method employed Gaussian smearing due to the large system. All the systems were relaxed until all forces were less than 0.01 eV/Å. Only Gamma point was used for the k-point sampling. The charge distribution was carried out by Bader analysis.[19,20]

The statistic calculations are carried out using classical Molecular Dynamic (MD) implanted in DL-POLY. In order to calculate the targeted gas selectivity and permeability through a single pore, the NPG membrane model is constructed into a large sheet (61.40Å×63.81Å), using the same pore configuration mentioned in DFT calculation. The pore density in this model is 2.55×10^{-4} $Å^{-2}$, comparable with the pore density of nitrogen doped graphene membrane ($\sim10^{-4}$ $Å^{-2}$) generated by ion bombardment.[21] The porous graphene

sheet was placed in the middle of a simulation cell with 100 Å in length, dividing the cell into two chambers. The initial configurations of gas molecules were randomly generated in one chamber by packmol.[22] And the other chamber was initially populated by 4 H_2 molecules (0.88 bars). All gas pressures quoted herein this study were calculated by Peng-Robinson equation of state (PREOS).[23] Hard Leonard-Jones wall was placed in the ends of two chambers in order to prevent the periodic interaction. Newton's equations of motion were integrated using Velocity Verlet algorithm[24] with a time-step of 1.0 fs. The temperature was maintained at 313.15 K by Nose-Hoover thermostat[25, 26] with a relaxation time of 1.0 ps. Intermolecular interactions, which dominate by van der Waals forces, are performed by the Lennard-Jones (LJ) potential and electrostatics. The cut-off distance for LJ and Columbic interactions is set into 15.0 Å. All crossing terms of the Lennard-Jones interactions were determined by the Lorentz-Berthelot mixing rules. For gas molecules with quadruple moments, we have adopted the EPM2 model[27] and X1 model[28] for CO_2 and N_2, respectively. For H_2 and CH_4, neutral one-site beads from Buch et al.[29] and Martin et al.[30] have been employed, respectively. LJ parameters of atoms within the graphene membrane were taken from CHARMM[31].

8.3 Results and Discussion

As the kinetic diameters of each gas molecules vary, the nanopores of different diameters were tested in the first place. The effect of N substitution doping was considered for the nanopores as well, as shown in Figure 8.1. Each nanopore is denoted as "pore-x"; x is the number of vacancies or missing atoms that forms the pore. As the H_2 and CO_2 possess the closest kinetic diameters,[4] the MD calculations of H_2 and CO_2 gas mixture are performed to screen the pore size factor. As shown in Table 8.1, pore-6 is too

small to pass through any gas molecules, while pore-13 is far too large, where both H_2 and CO_2 are permeable. Hence, the pore-10 is the best candidate. As noted earlier (Chapter 4), the defect-defect interaction cannot be neglected, unless the graphene supercell is larger than 7×7. In order to investigate the gas selection of functionalized pores, the pore-pore interaction factor should be screened out. Here two models have been built to tackle the problem. Model-1 is to adopt a graphene cluster (Figure 8.2), inspired by the study of the interface between molecules and solid surfaces.[32] The pore-10 porous graphene cluster consists of 6-circle carbon with outer 2-circle fixed along with the terminated H atoms in the outer ring. All other atoms are fully relaxed during all the calculations. The carbon atoms around the pore edge are substituted by nitrogen atoms. Model-2 is to build the functionalized pore in the periodic condition (Figure 8.3). A 7×7×1 porous graphene supercell was used in the calculation, where pore-10 is shown in the periodic superlattice. The electron density and charge of all the atoms in Model-1 and Model-2 are illustrated in Figures 8.1, 8.2, 8.3 and 8.4, respectively. Comparing the charges of the atoms in the two models, especially the ones around the functionalized pore, it is noted that the difference is under ±5%. Therefore, Model-2 should have nearly the same electronic performance as Model-1 and can be adopted for further calculations, as it is less computationally intensive.

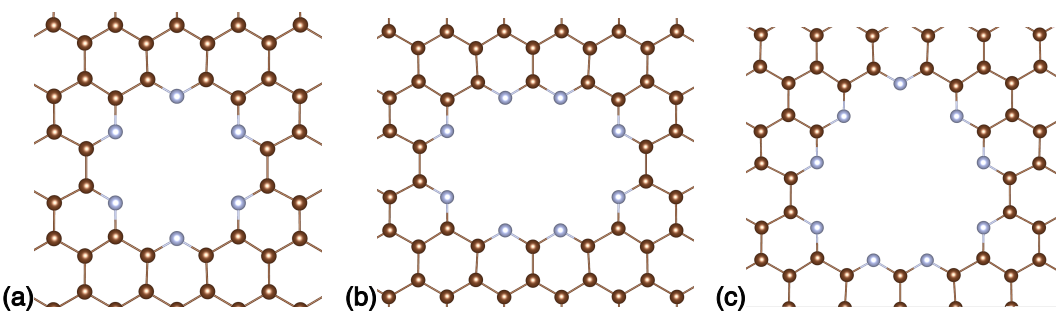

Figure 8.1 The nanoporous graphene selected for gas selection. (a) pore-6; (b) pore-10; (c) pore-13

Table 8.1: H_2 and CO_2 passages in each separate MD simulation

	1st Run		2nd Run		3rd Run	
	H_2	CO_2	H_2	CO_2	H_2	CO_2
Pore-6	0	0	0	0	0	0
Pore-10	28	0	26	1	25	2
Pore-13	206	62	211	64	220	54

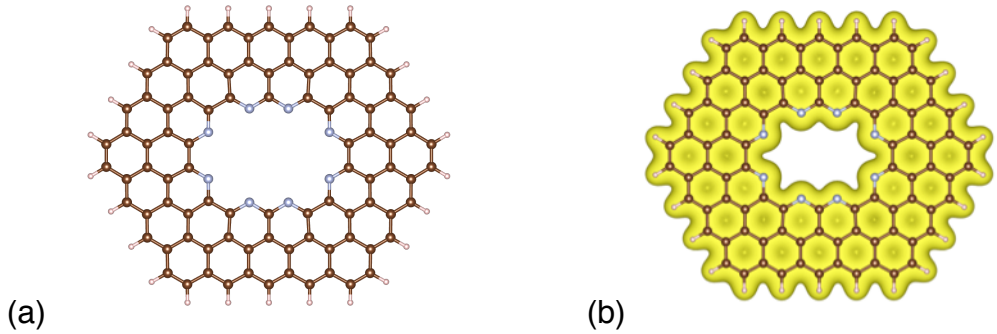

Figure 8.2 (a) the nanoporus graphene cluster in DFT calculation, with hydrogen in pink, nitrogen in blue and carbon in brown. (b) The electron density of pore-10 NGP cluster (isosurface = 0.02 e/a_0^3)

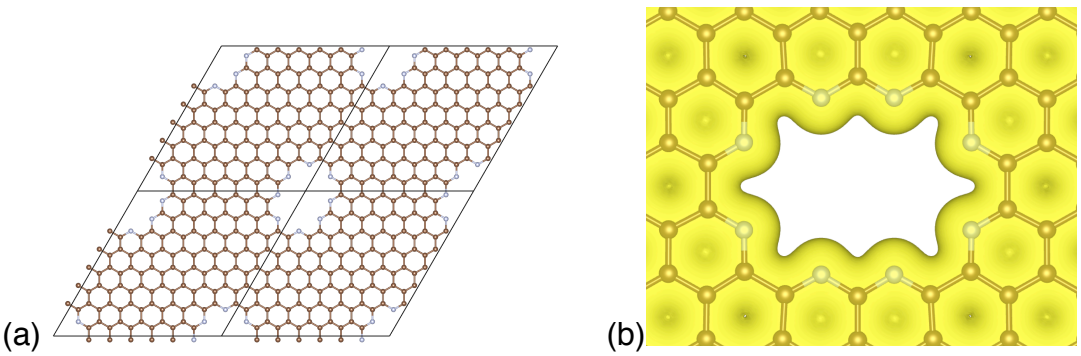

Figure 8.3 (a) The periodic model of pore-10 NGP in DFT calculation, with nitrogen in blue and carbon in brown. The solid line shows the periodic boundary. (b)The electron density of periodic pore-10 NGP (isosurface = 0.02 e/a_0^3)

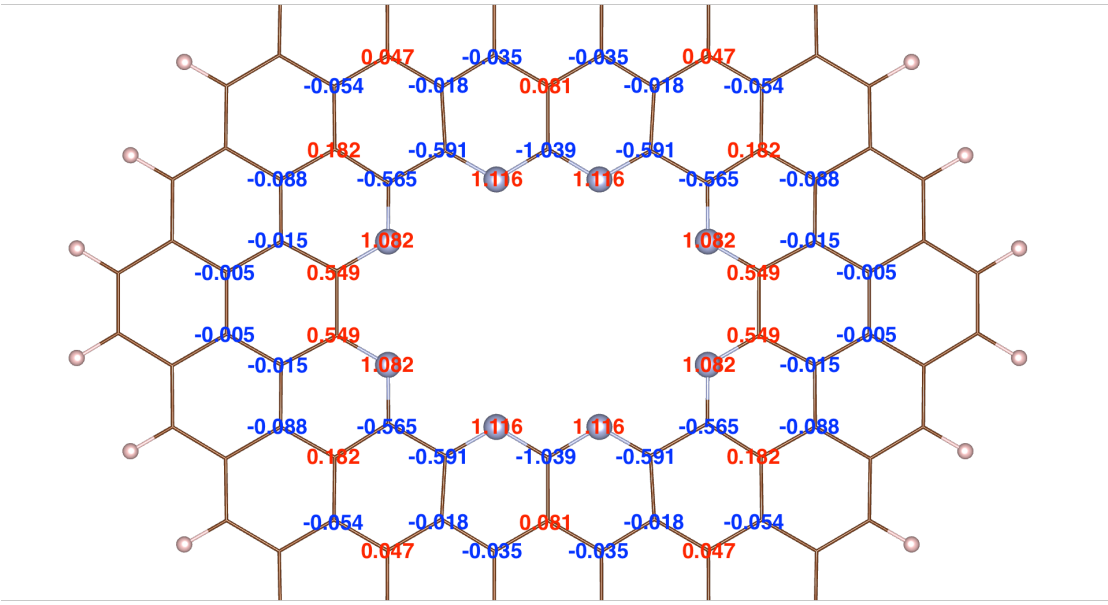

Figure 8.4 Charge difference distribution of Model-1. Nitrogen atoms represent in light blue balls and carbon atoms are simplified as sticks. The charge-accumulated atoms are in red, while the decreased ones are in blue.

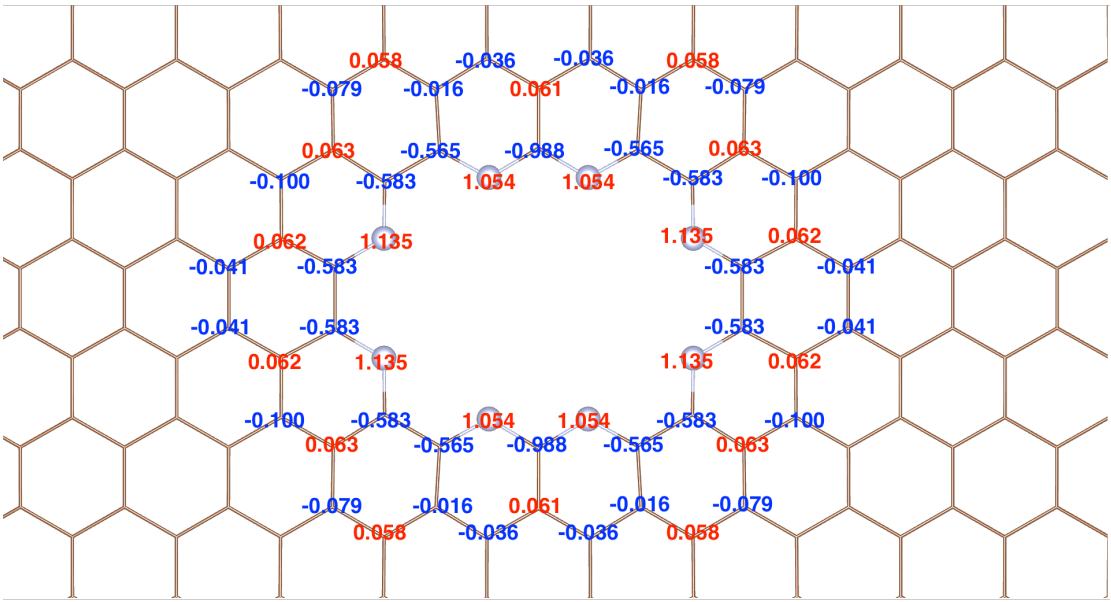

Figure 8.5 Charge difference distribution of Model-2. Nitrogen atoms represent in light blue balls and carbon atoms are simplified as sticks. The charge-accumulated atoms are in red numbers, while the decreased ones are in blue.

To describe the interaction between a gas molecule and the nanopore graphene, the binding energy is defined as follows

$$E_b = E_{total} - E_G - E_{gas}$$

where the E_{total} is the energy of the whole system, E_G and E_{gas} are the energies of the nanopore graphene and the gas molecule, respectively.

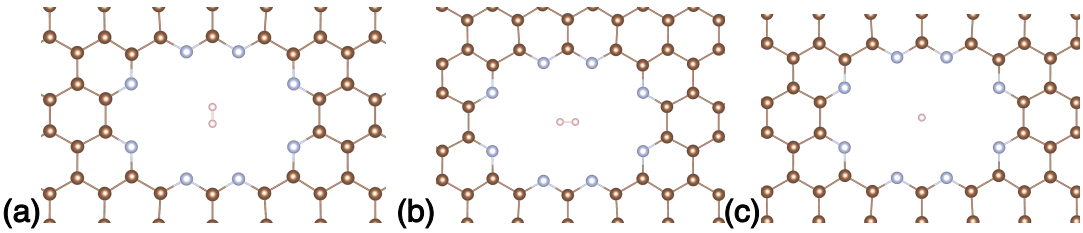

Figure 8.6 The top views of demonstration of three orientations of gas molecules passing through the nanopores. Here take H_2 as an example. From left to right are short shoulder, long shoulder, and perpendicular orientations, respectively.

Before systematic calculations, the orientations of the gas molecules passing through the pore were tested, including the perpendicular, parallel-along-short-shoulder, and parallel-along-long-shoulder, to the graphene plane, as indicated by the arrows in Figure 8.6. The favourable orientation is determined by the energy difference from that of the most favoured orientation, as listed in Table 8. The results show that the behaviour of the different gas molecules varies. H_2 prefers to pass parallel along the short shoulder through the sheet, and the additional energy penalty is less than 0.05 eV if it's perpendicular. It is also the favourable orientation in the half-decorated nanopore graphene in a previous study.[33] However, N_2 and CO_2 prefer to pass perpendicular through the pore. Especially, when its orientation is parallel along the short shoulder, the relative energy can rise to 3.20 eV and 0.69 eV for CO_2 and N_2, respectively. Furthermore, the relative energies of H_2 in the other two directions are under k_BT (25 meV). Therefore, there is no orientational stricture for H_2 diffusion at room temperature. And this phenomenon is

consistent with the results in our MD simulations. So the most favoured orientation for each molecule is selected for further DFT calculations.

Table 8.2 The relative energy (eV) when linear gas molecules pass the pore according to different orientations

	Short shoulder	Long shoulder	Perpendicular
H_2	0	0.01	0.05
N_2	0.69	0.16	0
CO_2	3.20	0.81	0

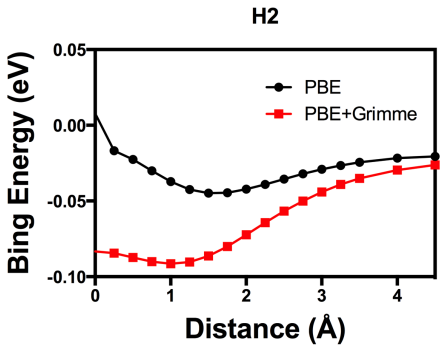

Figure 8.7 The binding energy of H_2 through the nitrogen-functionalized nanopore graphene. The black circles are the results for PBE, and the red squares are those for PBE+Grimme.

Since four gas molecules have different pathways through the nanopore, we measured the distance between the mass central of gas molecules and the centre of the nanopore graphene. For H_2 gas molecule, which prefers to pass parallel to the graphene plane through the pore, the binding energy is shown in Figure 8.. The equilibrium distance for H_2 is at 1.5 Å in PBE functional and the strongest binding distance is at 1.0 Å in PBE+Grimme functional. And the binding energy at the equilibrium state is 44.8 and 91.4 meV for PBE and PBE+Grimme functional, respectively. The difference of those results can be

considered reasonable as the semi-empirical PBE+Grimme includes the long-term charge dispersion. When the H_2 gas molecule is placed in the central of the nanopore, the PBE gives a slightly repulsive result, while the PBE+Grimme yields an attractive one. Compared with a previous study, with the nanopore edge decorated by a equal proportion of nitrogen and hydrogen,[9] it seems that increasing the nitrogen-doping ratio can improve the interaction between the H_2 and nanopore graphene. On the basis of gas molecular diffusion barrier, the energy barrier for H_2 goes through the nanopore is 37.1 and 8.1 meV for PBE and PBE+Grimme, respectively.

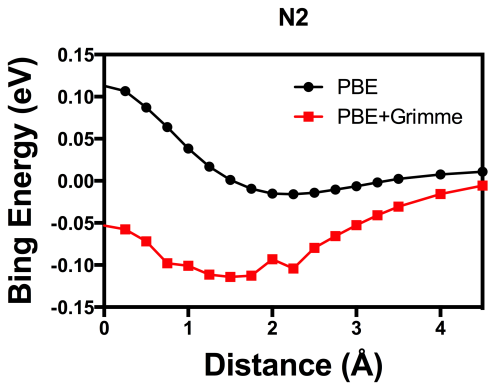

Figure 8.8 Binding energy of N_2 through the nitrogen-functionalized nanopore graphene. The black circles are the results for PBE, and the red squares are those for PBE+Grimme.

Similar to H_2 gas molecule, the gas contaminant N_2 shows the same trend, as noted in Figure 8.. The binding site of N_2 is at 2 Å with a binding energy of 41.9 meV for PBE functional. For vdW-DF calculations, the N_2 experienced two lowest binding sites perpendicularly through the nanopore, with the first lowest at 2.25 Å and the second lowest at 1.50 Å. As the N_2 moves closer to the pore, both nitrogen atoms of N_2 experience an interaction mode change from attraction to repulsion. However, these two atoms are neither at the same height nor the same phase. Consequently, the interactions with the two atoms are not synchronous in the same “pause”. Hence, there will be a saddle point for the total interaction. Interestingly, it shows the same binding height

as the PBE results in the second lowest case. Therefore, the PBE can yield accurate gas binding behavior, in general, but neglects the charge dispersion as the van der Waals is not taken into count. For the gas diffusion energy barrier, it is 128.8 meV for PBE and 60.0 meV for PBE+Grimme.

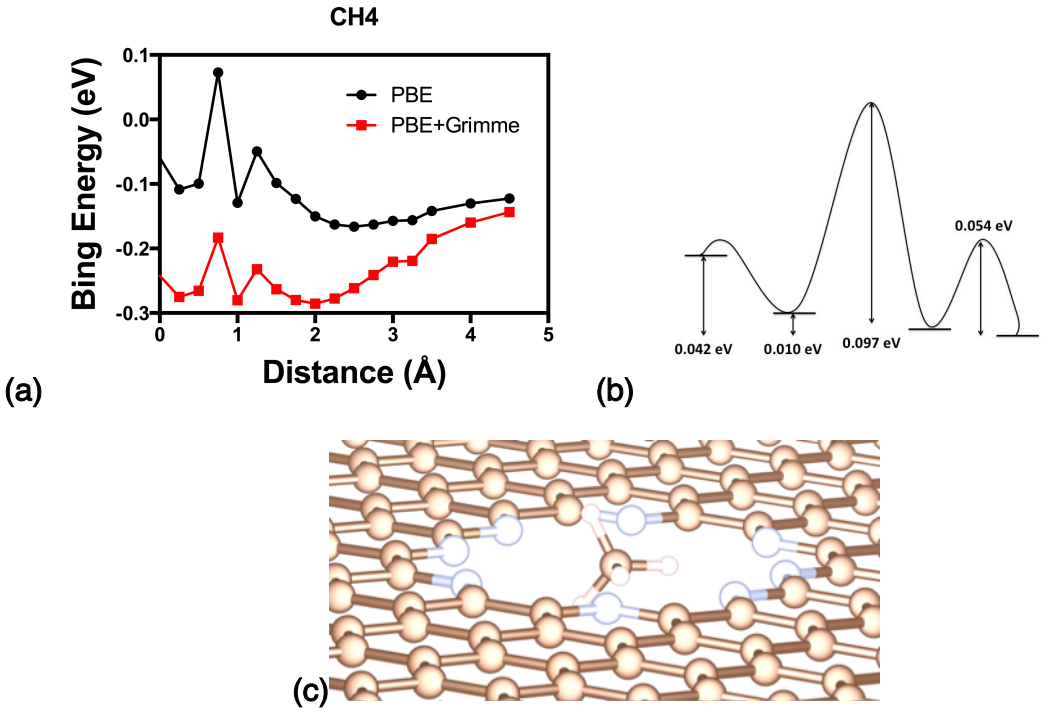

Figure 8.9 (a) The binding energy of CH_4 through the nitrogen-functionalized nanopore graphene. The black circles are the results for PBE, and the red squares are those for PBE+Grimme. (b) Energy barrier diagram of CH_4 through the nanopore with consideration of van de Waals interactions (c) The orientation of CH_4 molecule passes through the nanopore graphene.

For the tetrahedron CH_4 gas molecule, all the relaxations were calculated by fixing the central carbon atom. The favorite orientation is when two of the H atoms point to adjacent corners of the long shoulder and the other two perpendicular to the pore, as shown in 8.9(c). The equilibrium position, which is 2.5 Å for PBE and 2.0 Å for PBE+Grimme functionals. After the first and the lowest (in energy) binding site, the molecule moves closer to the sheet, there will be other two saddle points. The second lowest is at 1 Å, where the edge of the molecule is inside of the nanopore. When the first hydrogen atom passed through the pore, the highest energy barrier is 97 meV. The energy barrier diagram is shown in Figure 8. (b).

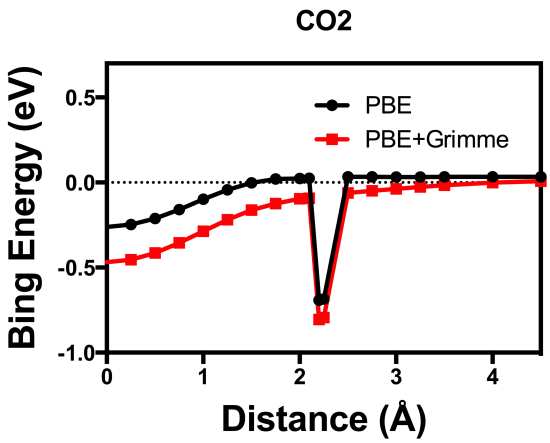

Figure 8.10 The binding energy of CO_2 through the nitrogen-functionalized nanopore graphene. The black circles are the results for PBE, and the red squares are those for PBE+Grimme.

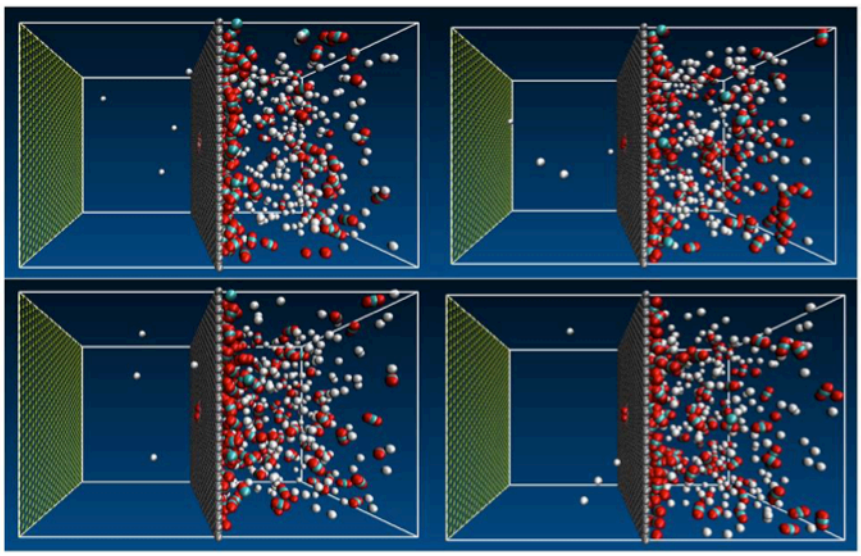

Figure 8.11 Snapshots of H_2+CO_2 system at 0 ns (up left), 1 ns (up right), 2 ns (down left), 3 ns (down right). (White balls represent H, cyan balls are C and red balls are O)

As a linear molecule, CO_2 behaves rather more interestingly, as shown in Figure 8.10. There is a significant energy trap at a distance between 2.20-2.25 Å to the graphene plane. To confirm the results, we doubled sample points around this area. Further, we tested the H_2+CO_2 gas mixture using MD simulations. It shows that two CO_2 molecules would linger in the middle of the nitrogen-doped pore, fully blocking all other gases from permeating through the pore. The snapshots of MD simulation are shown in Figure 8.11. There

are 1 to 4 H_2 atoms slipping through the pore by chance before the blockage by CO_2, but the general trend is nearly null permeability for both gases. This phenomenon is concluded based on 21 simulation tests: 3 independent simulations for 7 different pressure gradients. Both DFT and MD results show this nitrogen decorated nanopore graphene sheet is fully blocked by trapped CO_2.

Overall, the nanopore attracts gas molecules, even when they position in the center of the pore when van de Waals correction has been considered. It can imply that the proposed nanoporous graphene attracts gas molecules to the pore area. However, the energy barrier varies, as listed in Table 8.3.

According the Arrhenius equation for diffusion, the estimated membrane selectivity can be given as

$$S_{H_2/gas} = \frac{D_{H_2}}{D_{gas}} = \frac{A_{H_2}}{A_{gas}} \frac{e^{-E_{H_2}/RT}}{e^{-E_{gas}/RT}}$$

where *D* is the diffusion rate, *A* is the prefactor, and *E* is diffusion barrier. By assuming $\frac{A_{H_2}}{A_{gas}} \approx 1$ at room temperature, the predicted selectivity can then be simplified to

$$S_{H_2/gas} = \frac{e^{-E_{H_2}/RT}}{e^{-E_{gas}/RT}} = e^{(E_{gas}-E_{H_2})/RT}$$

The predicted H_2 selectivity over other gas contaminants is listed in Table 8.3. Notably, our proposed model has superior performance for the selectivity of H_2/CO_2, compare to graphene oxide membranes,[34] poly(1-trimethylsilyl-1-propyne) (PMSP) ,[35] polyetherimide (PEI)[36] or carbon molecular sieve (CMS) membranes.[3737] Meanwhile, the selectivity of H_2 over N_2 is not as good as CO_2, where the interaction energy is one magnitude lower when the gas molecule is positioned in the center of the pore.

Table 8.3 The energy barriers of $H_2/N_2/CH_4/CO_2$ gas molecules for vdW-DF. And the predicted H_2 selectivities from the gas contaminants are also listed.

	H_2	N_2	CH_4	CO_2
Energy barrier (meV)	8.1	60.0	97.0	71.2
Predicted selectivity	N/A	8	35	12.5

To investigate the mechanism behind the energy trap of CO_2 molecules, we plot the charge density difference when CO_2 at 2.25 Å in Figure 8., according to the following equation.

$$\rho = \rho_{total} - (\rho_G + \rho_{CO_2})$$

where ρ_{total} is the total charge density in this configuration, the ρ_G and ρ_{CO2} are charge densities of the isolated nanopore graphene and the CO_2, respectively. As shown in the Figure 8.12, the CO_2 induces charge transfer into the nanopore graphene sheet. The more electronegative nitrogen in the short shoulder attracts more electrons while the carbon in the long shoulder loses more. This transition makes the nearest nitrogens interact more strongly with the carbon atom in CO_2. Meanwhile, the charge within CO_2 also undergoes redistribution, where C in CO_2 is less electron negative. It is also reflected in the C-O bond length, increased by 8 pm. The more electron negative N in the porous graphene and more electron positive C in CO_2 make the interaction much stronger than other molecular cases considered here.

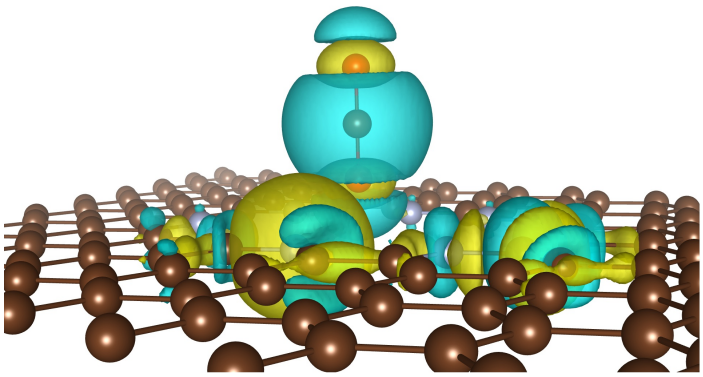

Figure 8.12 Charge density difference of the CO_2 at energy trap position. The yellow area represents the charge accumulated while the blue one where deceased. (isosurface = 0.004 e/r_0^3)

8.4 Conclusions

DFT and Molecular Dynamics simulations were employed to investigate relative selectivity of the porous graphene for H_2 purification. Pore-size effect was first considered, and a monolayer nitrogen-doped porous graphene membrane with a critical pore size of 10 missing C-atoms (pore-10) was selected as the model system. Several gas molecules are considered in the simulations. N_2 and CO_2 only pass through the nanopore perpendicular to the graphene plane. While H_2 shows a slight preference to diffuse parallel to the graphene plane towards the pore and then through the nanopore, and it only costs 0.05 eV extra energy for H_2 to travel perpendicularly. Nitrogen doping around the nanopore attracts all the gas molecules under consideration, H_2/N_2/CH_4/CO_2, but to a more varies extend, so that enhanced selectivity can be achieved. This is mainly due to much-varied energy barrier for the diffusion of the molecules, ranging from 8.1 to 97 meV. At room temperature, the thermal activation is around 25 meV, which is more than enough for H_2 to pass through the pore, but is only one third or even fourth of the energy barrier for other gas contaminants. An interesting phenomenon is also observed for CO_2 interaction with the nanopore graphene, where there is an

energy trap near the pore area of the graphene sheet, causing CO_2 to block the pore area. This is also verified from our MD calculations under different pressures.

References

[1] M. Hirscher, Katsuhiko Hirose, *Handbook of Hydrogen Storage: New Materials for Future Energy Storage*, John Wiley & Sons, **2010**, ISBN: 978-3-527-32273-2

p. 368;

[2] R. B. Gupta, *Hydrogen Fuel: Production, Transport and Storage,* CRC Press, **2008**, ISBN 9781420045758 – CAT 4575X, p. 628;

[3] A. Godula-Jopek, W. Jehle, and J. Wellnitz, *Hydrogen Storage Technologies: New* Materials, Transport, and Infratructure, ISBN: 978-3-527-32683-9

[4] W. D. Breck, Zeolite Molecular Sieves, John Wiley & Son, Inc., New York, 1974, p 636;

[5] H. Du, J. Li, J. Zhang, G. Su, X. Li, and Y. Zhao, J. Phys. Chem. C 2011, 115, 23261;

[6] C. Sun, M. S. Boutilier, H. Au, P. Poesio, B. Bai, R. Karnik, and N. G. Hadjiconstantinou, *Langmuir,* **2014**, 30(2), 675;

[7] L.W. Drahushuk, M. S. Strano, *Langmuir* **2012**, 28, 16671;

[8] T. Wu, Q. Xue, C. Ling, M. Shan, Z. Liu, Y. Tao, and X. Li, *J. Phys. Chem. C* **2014**, 118, 7369;

[9] M. Shan, Q. Xue, N. Jing, C. Ling, T. Zhang, Z. Yan, and J. Zheng, *Nanoscale* **2012**, 4, 5477;

[10] G. Kresse and J. Hafner, *Phys. Rev. B,* **1993**, 47, 558;

[11] G. Kresse and J. Furthmüller, *Comput. Mat. Sci.* **1996**, 6, 15;

[12] P.E. Blochl, *Phys. Rev. B* **1994**, 50, 17953;

[13] G. Kresse and D. Joubert, *Phys. Rev. B* **1999**, 59, 1758;

[14] J. P. Perdew, K. Burke, and M. Ernzerhof, *Phys. Rev. Lett.* **1996**, 77, 3865;

[15] J. P. Perdew, K. Burke, and M. Ernzerhof, *Phys. Rev. Lett.* **1997**, 78, 1396;

[16] S. Grimme, *J. Comp. Chem.,* **2006**, 27, 1787;

[17] X. Jiang, C. Århammer, P. Liu, J. Zhao, and R Ahujia, *Scientific Reports* 2013, 3, 1877;

[18] A. Ambrosetti, and P. L. Silvestrelli, *J. Phys. Chem. C* **2014**, 118, 19172;

[19] W. Tang, E. Sanville, and G. Henkelman, *J. Phys.: Condens. Matter* **2009**, 21, 084204;

[20] E. Sanville, S. D. Kenny, R. Smith, and G. Henkelman, *J. Comp. Chem.* **2007**, 28, 899;

[21] S. C. O'Hern, M. S. H. Boutilier, J. –C. Idrobo, Y. Song, J. Kong, T. Laoui, M. Atieh and R. Karnik, *Nano. Lett.* **2014**, 14, 1234;

[22] L. Martinez, R. Andrade, E. G. Birgin, and J. M. Martinez, *J. Comput. Chem.* **2009**, 30, 2157;

[23] D.-Y. Deng and D. B. Robinson, *Ind. Eng. Chem. Fundam.* **1976**, 15, 59;

[24] W. C. Swope, *J. Chem. Phys.* **1982**, 76, 637;

[25] S. Nosé, *Mol. Phys.* **1984**, 52, 255;

[26] W. G. Hoover, *Phys. Rev. A* **1985**, 31, 1695;

[27] J. G. Harris and K. H. Yungt, *J. Phys. Chem* **1995**, 99, 12021;

[28] C. S. Murthy, K. Singer, M. L. Klein, and I. R. McDonald, *Mol. Phys.* **1980**, 41, 1387;

[29] V. Bush, *J. Chem. Phys.* **1994**, 100, 7610;

[30] M. G. Martin and J. I Siepmann, *J. Phys. Chem. B* **1998**, 102, 2569;

[31] A. D. Mackerell, D. Bashford, R. L. Dunbrack, J. D. Evanseck, M. J. Field, S. Fischer, J. Gao, H. Gao, S. Ha, D. Joseph-McCarthy, L. Kuchnir, K. Kuczera, F. T. K. Lau, C. Mattos, S. Michnick, T. Ngo, D. T. Nguyen, B. Prodhom, W. E. Reiher, B. Roux, M. Schlenkrich, J. C. Smith, R. Stote, J. Straub, M. Watanabe, J. Wiórkiewicz-Kuczera, D. Yin and M. Karplus, *J. Phys. Chem. B,* **1998**, 102, 3586;

[32] R. C. Hoft, M. J. Ford, A. M. McDonagh, and M. B. Cortie, *J. Phys. Chem. C,* **2007**, 111(37) 13886;

[33] D. –E. Jiang, V. R. Cooper, and S. Dai, *Nano Lett.* **2009**, 9 (12), 4019;

[34] H. W. Kim, H. W. Yoon, S. –M. Yoon, B. M. Yoo, B. K. Ahn, Y. H. Cho, H. J. Shin, H. Yang, U. Paik, and S. Kwon, *Science*, **2013**, 342, 91;

[35] K. Nagai, A. Higuchi, T. Nakagawa, *J. Polym. Sci. B* **1995**, 33, 289;

[36] M. E. Rezac, B. Schöberl, *J. Membr. Sci.* **1999**, 156, 211;

[37] D. Shekhawat, D. R. Luebke, H. W. Pennline, *Report DOE/NETL 2003/1200* **2003**

Chapter IX
General Conclusions

The project is mainly dedicated to bandgap engineering of 2D materials using first-principles simulations (DFT). Several approaches were established to tune the properties of those materials. For graphene of a zero bandgap, two approaches have been studied: 1) defects and functionalizing doping; 2) substrate induced hybrid structures. For phosphorene with a natural bandgap, nanostructuring into nanoribbons and strain engineering have been systematically studied. Furthermore, with phosphorene as a natural bandgap source, the graphene/phosphorene/graphene sandwich heterostructures are investigated for band-edge engineering and optical properties. Moreover, defective nitrogen-doped graphenes with nanopores have been studied for gas separation and purification. The main achievements are summarized as follows:

1) For graphene with vacancy and nitrogen substitutions, all of the modified graphenes undergo Jahn-Teller like distortion. For pure N-doped graphenes, N atoms avoid adjacent doping sites and the formation of N-N bonds at a relatively low doping ratio (below 2 N-doping), while the situation is reversed at a high doping ratio (larger than 3 N-doping). This trend also holds for the N-doped defective complexes. For the pure vacancy cases considered, divacancy is the most stable configuration. This conclusion is drawn from relatively accurate results from PBEsol functionals, which is proven to give more reliable predictions for solid state materials. For the N-doped defective complexes, the V_C+3N_C and 2V_C+4N_C are the most stable configurations in mono-vacancy and di-vacancy cases, respectively. The later configuration of the defective graphene shows a bandgap up to 0.27 eV. The calculated effective masses are 0.089 and 0.072 m_0 for electron and hole, respectively. The results indicate that event with this bandgap the defective complex still retains its high conductivity.

However, this proposed model possesses a high defect ratio (4%), which may be difficult to achieve in practice (0.3-2.9%)[1] at the moment.

2) For the diamond-substrate tuned graphene bandgap, both diamond (111) and (100) surfaces can open the bandgap of graphene, where the bandgaps of Gr@H_SCD(100) and the Gr@H_SCD(111) are 61 meV and 20 meV, respectively. These results can further in line with the experimental collaborators' results. The simulations also identify that the H treatment is essential to bandgap tuning on a diamond substrate, in addition to surface orientations. The hydrogen treatment enhances the interaction of the heterostructures, which can further induce charge redistribution. The main driving force for this bandgap opening is the electron transfer from the π states of graphene into H on diamond surfaces.

3) For phosphorene, it is demonstrated that the van der Waals interaction is essential for simulation of bulk phosphorous and the HSE06 functional is sufficiently accurate for the bandgap prediction. Moreover, nanostructured ribbons show significant quantum confinement effect, which largely modulates the bandgap as the ribbon width changes. Furthermore, straining along the ribbons is also shown to change the bandgap structure. Particularly, the d-PNR demonstrates a direct to indirect bandgap transition for both compressive and tensile strains. It is possible to engineer the d-PNR structure by straining so that two valleys inside the first Brillouin zone are energetically degenerate with electrons of widely different momenta able to coexist at the same energy. These materials are thus of interest for valleytronics applications.

4) For the graphene/phosphorene/graphene sandwich heterostructure, charge redistribution can open the graphene bandgap to 19 meV while retaining a high carrier mobility. Meanwhile, the optical properties are highly anisotropic, due to the puckered phosphorene. The calculated dielectric constant along the y-axis is two order of magnitude greater than that of the z-axis. Such distinguished properties have implications for optical birefringence, and optical sensor applications.

5) For the selectivity of gas molecules (H_2/N_2/ CO_2/CH_4) through nitrogen-doped porous graphene, different gas molecules behave rather differently. N_2 and CO_2 only pass through the nanopore perpendicularly. H_2 prefers the parallel pathway through the nanopore though the energy cost is only 0.05 eV if it is to path perpendicularly. The energy barrier of different gas molecules do vary considerably: 8.1 meV for H_2, far less than the thermal energy at room temperature, but 60-90 meV for other gas molecules. An interesting phenomenon is identified for CO_2 interaction with the nanopore graphene, where there is an energy trap near the pore of the graphene sheet. At this special point, more electrons are transferred to nitrogen to attract CO_2. Hence, this specially designed nanopore graphene is perfect for H_2 purification at room temperature.

---

[1] C. Zhang, L. Fu, N. Liu, M. Liu, Y. Wang, and Z. Liu, *Adv. Mater.* **2011**, 23, 1020;

Chapter X
Future Work

Based on the achievements on the study of the 2D materials, the following specific tasks may be considered for further research:

- To combine the N-doped defective graphene and the H-treated diamond substrate: this hybrid may further tune the graphene bandgap for electronic or optical applications. Moreover, such combinations, especially the vacancy/substitution only defects, are closely associated with realistic experimental environments;

- Besides graphene, other 2D materials, e.g. MoS_2 and hBN, may be considered as candidates to build 2D heterostructure to explore the electrical and optical properties;

- Heterostructures of bilayers or trilayers of graphene/phosphorene, MoS2/phosphorene and hBN/phosphorene may be explored for their specific functionalities. Further, the modification of those properties under strain engineering may also be studied;

- Predicted blue phosphorene[1] and other possible 2D materials should be explored to enrich the "2D building blocks" for future "designer structures" with unique and controlled properties for the rapid advancement of many technologies, such as electronics, photonics, photo-catalysis and even, molecular sensing, separation and storage.

[1] J. Guan, Z. Zhu, D. Tománke*, Phys. Rev. Lett.* **2014**, 113(4), 046804;

List of Figures

List of Tables

List of Publications

1. **Xiaoyu Han**, Henry Morgan Stewart, Stephen A. Shevlin, C. Richard A. Catlow, and Zheng Xiao Guo, Strain an Orientation Modulated bandgaps and Effective Masses fo Phosphorene Nanoribbons, *Nano Letts* **14**(8), 4607-4614;
2. Fang Zhao, Andrei Vrajitoarea, Qi Jiang, **Xiaoyu Han**, Aysha Chaudhary, Joseph Welch, and Richard Jackman, Graphene Electronic Properties by Hydrogen-terminated Monolayer Nanodiamond Substrate and its applicant in Field-Effect Transistors, *Scientific Report,* **5**, 13771*;*
3. Haisheng Li, Weiguang, Chen, **Xiaoyu Han**, Qiang Sun, Zhengxiao Guo, and Yu Jia, Van der Waals Effects on Semiconductor Clusters, *Journal of Computational Chemistry,***36**(25), 1919*;*
4. **Xiaoyu Han**, Stephen A. Shevlin, Zheng Xiao Guo, Tuning Graphene Properties by Nitrogen doping and Vacancies, *in preparation*
5. Fang Zhao,[1] **Xiaoyu Han,[1]** John Gallop, Ling Hao, Andrei, Vrajitoare, Stephen, A. Shevlin, Richard B. Jackman, Zheng Xiao Guo, Graphene-Diamond van der Waals heterostructure FET, *in preparation*
6. Haitang Luo,[1] **Xiaoyu Han**,[1] Louise Wright, Stephen A. Shevlin, Zheng Xiao Guo, Enhanced H2 purification by nitrogen-doped nanoporous graphene, *inpreparation*
7. **Xiaoyu Han,** Henry Morgan Stewart, Stephen A. Shevlin, C. Richard. A. Catlow, Zheng Xiao Guo, Sunlight harvesting by phosphorene/graphene heterostructure, *inpreparation*